UNIVERSITÀ DEGLI STUDI DI MILANO

Physics, Astrophysics and Applied Physics PhD School
Department of Physics
Physics, Astrophysics and Applied Physics PhD Course
Cycle XXVIII

High brilliance photon pulses interacting with relativistic electron and proton beams

S. S. D. FIS/03

Supervisor: Dr. Vittoria PETRILLO
Co-supervisor: Prof. Lodovico LANZ
Director of the Doctoral School: Prof. Francesco RAGUSA

PhD Thesis of:
Camilla CURATOLO

A. A. 2015-2016

Commission of the final examination:

Dr. Calin Alexandru UR (Referee) - IFIN-HH (ROM)

Prof. Carlo PAGANI - Università degli Studi di Milano

Prof. Mauro GAMBACCINI - Università degli studi di Ferrara

Dr. Alessandro CIANCHI - Università degli Studi di Roma "Tor Vergata"

Dr. Giuseppe BREGLIOZZI - CERN (CHE)

Final examination:

Date 22-01-2016

Università degli Studi di Milano, Department of Physics, Milano, Italy

Contents

List of Figures

List of Tables

Introduction

Motivation

Recent progress in accelerators and lasers technology opens new perspectives in terms of particle-photon colliders luminosity: low cross section processes can be therefore utilized to create secondary beams with specific values of brightness, brilliance, emittance and energy spread.

We present a detailed study of the interaction between relativistic electron beams and high intensity laser pulses aimed at the production, through Inverse Compton scattering, of high brilliance γ rays. In particular, we focus on the simulations of the emitted photon beams for the Extreme Light Infrastructure Nuclear Physics Gamma Beam System. The machine, presently under construction, is designed to deliver γ ray photon beams of high monochromaticity (bandwidth lower than 0.5%), peak brilliance larger than 10^{19} photons/(s$\cdot 0.1\% \cdot$ mm$^2\cdot$mrad^2), large tunability, fully controlled polarization, spectral density larger than $5 \cdot 10^3$ photons/(s$\cdot$eV) and focused down to micron-scale spot sizes.

The possibility to generate low emittance TeV-class energy pion and muon beams via photo-production in a highly relativistic Lorentz boosted frame is discussed in the second part of the dissertation. The kinematics of all the events given by the proton-photon beams interaction have been studied: pion photo-production and further decay into muon and neutrino, lepton pair photo-production (electron/positron and muon pairs) and Inverse Compton scattering. We analyze the secondary beams brightness achievable by the coupling of advanced high efficiency high repetition rate FEL pulses and Large Hadron Collider or Future Circular Collider proton beams.

Dissertation overview

This Thesis consists of two Parts, for a total of seven Chapters.

Part I presents the high brilliance γ beam production through Inverse Compton scattering, with particular focus on the ELI-NP Gamma Beam System emission simulations. In Chapter 1 we introduce the Inverse Compton scattering and the ELI-NP-GBS: the main characteristics of the machine, the primary beams and the expected γ beam parameters. Chapter 2 recalls the theoretical aspects of the electron-photon interaction while Chapter 3 considers the beam-beam collision. Some analytical formulas and the simulation codes are presented. In Chapter 4 an example of ELI-NP γ beam simulation is reported together with the study of the polarization and of the possible machine error and jitters impact on the emitted radiation.

In Part II the proton-photon collision is considered. Chapter 5 introduces the idea of a Hadron-Photon Collider for the production of low emittance pion and muon beams. Chapter 6 describes the kinematic of all the possible events generated by the proton-photon interaction. The phase spaces of the secondary beams are produced by means of a home-made event-generator and the beams characteristics such as emittance and energy spread are benchmarked against analytical formulas. The luminosity and the flux considerations are reported in Chapter 7.

At last we draw the conclusions for both Parts.

Part I

High brilliance γ beams production through Inverse Compton scattering

CHAPTER 1

High brilliance γ beams production through Inverse Compton Scattering

1.1 Introduction

The Inverse Compton effect describes, in a QED theoretical frame, the process occurring when a relativistic electron interacts with a low energy photon. The same process studied with a classical approach is called Thomson scattering: in this case the quantum effects are disregarded. Depending on the features of the incoming particles, the correct method has to be chosen. In both cases, if an electron in the MeV-GeV energy range and an optical photon are considered, the main result of the scattering is a Döppler up-shift of the photon energy by a factor approximately $4\gamma_i^2$ where γ_i is the Lorentz factor of the electron: the emitted radiation is in the X/γ range.

The idea of producing high energy photons in accelerators through Inverse Compton Scattering (ICS) has been proposed by H. Motz [1] and K. Landecker [2] in 1951-52 and it was developed by R. Milburn [3] in 1963 and independently by F. Arutyunian and V. Tumanian [4] later on. The laser and accelerator techniques at those times did not allow to consider that proposal from a practical point of view due to the very low value of the Compton scattering cross section (the maximum value is given by the Thomson cross section $\sigma_T = 0.67$ barn). In 1978 the first Compton X/γ-ray facility, the LADON beam, started to work in Frascati [5,6] and the outcoming flux was useful for the study of photonuclear reactions.

The recent advances in accelerators and lasers technology give the opportunity to conceive compact Compton sources producing high brilliance X and γ-ray beams. Such a new generation of γ photon beams opens the way to applications at the frontier of science, allowing us to deepen the fundamental knowledge and understanding of the properties of materials and living systems by probing the matter on microscopic-to-nuclear scales in space and time. They will permit the Nuclear Resonance Fluorescence technique: nuclear waste remote sensing and diagnosis, special nuclear material recognition for national security and non-proliferation related issues, isotope sensitive imaging for medical and cultural heritage investigations are among the most appealing and high social impact applications that will be made feasible by such advanced gamma photon beams. Not to mention several research fields in nuclear physics dealing with fundamental nuclear structure studies about giant resonances and astro-physical open problems in star nucleo-synthesis that will greatly benefit from the availability of these new probes [7–9].

Compton sources are among the most performing devices in producing radiation with short wavelength, high power, ultra-short time duration, large transverse coherence and tunability. To produce radiation at a given photon energy, the required energy of the electron beam for a Compton light source is significantly lower than that of a synchrotron light source, consequently the costs and the dimensions are much more contained. Compared with a Bremsstrahlung beam with a broad band spectrum, the typical energy-angle kinematic dependence of the photons emitted by ICS makes it possible to obtain a quasi-monochromatic X/γ-ray beams using a collimation system. In addition, the energy of the Compton beam is completely tunable and it can be extended to cover a wide energy range from soft x-ray to very high energy gamma-ray. Furthermore, a Compton photon beam is highly polarized, and its polarization is controlled by the polarization of the incident photon beam.

In the existing Compton devices with emitted photon energies below 100 keV [10–15, 15–17], the emission is generally provided by the collision between a high energy laser and a high brightness electron beam generated by Linacs or storage rings [14], while more sophisticated schemes and interaction mechanisms are rapidly becoming a reality. The most usual configuration is the head-on scattering, with the collision angle between the interaction beams $\alpha = 180^o$, but also geometries with $\alpha = 165^o$ or $\alpha = 90^o$ have been tested [15]. The mean photon energy actually measured in the various sources ranges between 7 and 70 keV, each device presenting a wide tunability. Experiments on the source characterization [13, 18–20], on the transmission, dark field and phase contrast imaging, computed microtomography, K-edge techniques on phantom [21], biological [14,22], animal [23] and human [15] samples have been then successfully performed. As regards existing Compton sources emitting in the MeV range [24–35], the facility HIγS [36–40], which represents the state of the art up to now, relies on the emission produced by the scattering of an electron beam and its Free-Electron Laser (FEL) radiation. The total gamma-ray intensities (energy between 2 and 100 MeV with linear and circular polarizations) can reach over 10^9 photons per second with few percent energy resolution.

At the Nuclear Physics Pillar of the European laser facility Extreme Light Infrastructure (ELI) [41–44] an advanced Gamma Beam System is foreseen as a major component of the infrastructure, aiming at producing extreme gamma ray beams for nuclear physics and nuclear photonics experiments characterized by unprecedented performances in terms of monochromaticity, brilliance, spectral density, tunability and polarization.

1.2 Extreme Light Infrastructure - Nuclear Physics Gamma Beam System

The Extreme Light Infrastructure - Nuclear Physics Gamma Beam System (ELI-NP-GBS) is presently under construction close to Bucharest, in Magurele (Romania). The conceivement and the design of the machine has been performed by the European collaboration EuroGammaS starting in 2011.

The ELI-NP-GBS is a linear machine based on the collision of an intense high power Yb:Yag J-class laser and a high brightness electron beam with a tunable energy up to 750 MeV. The main specifications of the Compton Source are: photon energy tunable in the $0.2 - 19.5$ MeV energy range, rms relative bandwidth smaller than 0.5% and spectral density lager than $5 \cdot 10^3$ photons/s·eV, with source spot sizes smaller than 100 μm and linear polarization of the gamma-ray beam larger than 95%. Moreover the peak brilliance of the γ beam is expected to be larger than 10^{19} photons/(s·mm^2·mrad^2·0.1%).

In order to achieve these very challenging specifications, the luminosity $\mathcal{L}$ of the source must be larger than 10^{35} s^{-1}cm^{-2}, as specified by

$$\mathcal{L} = \frac{N_e N_L r}{4\pi\sigma_0^2} \tag{1.1}$$

where N_L are the photons carried by the laser pulse at collision, N_e the electrons carried in the bunch, σ_0 the spot size at the Interaction Point (IP) and r the repetition rate of the collisions (assuming ideal overlap in space and time of the two colliding pulses, as well as negligible diffraction of the two beams over the interaction distance). Using ELI-NP-GBS nominal values for the colliding beams (0.4 J for the laser pulse energy, 250 pC the electron bunch charge, focused down to about 20 μm with an effective repetition rate of 3.2 kHz obtained by a recirculated laser pulse coupled to a multi-bunch electron beam time structure, delivering 32 electron bunches every RF pulse at a repetition rate of 100 Hz) we find $\mathcal{L} = 1.2 \cdot 10^{35}$ s^{-1}cm^{-2}. The total number of back-scattered photons per second, all over the spectrum and solid angle, is given by the luminosity multiplied by the total cross section $\mathcal{N} = \mathcal{L}\sigma_{tot}$, in our case $\mathcal{N} = 7 \cdot 10^{10}$ photons/s.

Any Compton source is a polychromatic source of back-scattered photons: in order to produce a monochromatic photon beam one needs to select a narrow cone around the electron beam propagation axis by means of special collimators, which become quite challenging at photon energies above 1 MeV [45]. So what really matters for experiments and applications of the collimated photon beams, is the number of photons N^{bw} carried by the back-scattered radiation pulse within such a small angle, and the rms bandwidth associated with it $\Delta\nu_p$ - that is the concept of spectral luminosity and spectral density, which are the real figure of merit for Nuclear Physics and Photonics applications. The Spectral Density, defined as

$$SD = \frac{N^{bw}r}{\sqrt{2\pi}\Delta\nu_p} \tag{1.2}$$

is typically expressed in units of photons/s· eV. Various generations of γ-ray sources have improved this figure of merit, from values of the order of 1 for bremsstrahlung sources, to about 100 for the present HIγS facility [38], toward the 10^4 range which is the goal of ELI-NP-GBS.

The strategy to achieve such an impressive upgrade in the performances is to adopt a multi-bunch operation mode for the electron Linac and to recirculate the laser pulse as many times as possible at the IP. In this way we will combine the capability of a RF Linac driven by high brightness photo-injector to provide outstanding peak electron beam quality in the single bunch with a higher repetition rate than the one typical of such Linacs (100 Hz). Since the laser pulse carries about 10^{18} photons at the IP, but only 10^7 photons maximum are back-scattered at each collision (in other words the electron beam is almost transparent to the laser pulse), then we can conceive to re-use the laser pulse and bring it back to a new collision at the same IP with a new fresh incoming electron bunch. This requires a Linac able to operate in multi-bunch mode and an optical device able to recirculate the laser pulse.

Such an advanced and innovative laser re-circulator is under test by the EuroGammaS collaboration and will be integrated in the ELI-NP-GBS installation phase starting end of this year 2015, for a full description of this new optical device see Refs. [46,47]. Due to several constraints to fulfill in its design, concerning mirror quality, damage threshold, alignment and synchronization of the 2 parabolic mirrors and the 32 plane mirror pairs (a challenging 20 μm and 20 μrad alignment tolerance is required), the focal length of the parabolic mirrors has been set at 1.2 m, implying a round-trip time for the laser pulse of about 16 ns. A total of 32 round-trips have been designed and carefully simulated with a physical laser transport simulation code in order to asses the quality of the laser pulse at the IP at any round-trip. The expected performance is quite close to 100% in the total accumulated spectral density over the 32 pulses as far as the 32 electron bunches will collide at the IP with same constant beam quality over the multi-bunch train. The time structure of the generated γ-ray pulses will be therefore made of 32 pulse long trains repeating at 100 Hz (10 ms far apart), consisting of 32 micro-pulses separated by 16 ns (each micro-pulse with rms pulse length of $0.7 - 1$ ps).

In order to generate the high brightness electron beam requested, ELI-NP-GBS adopts an S band photo-injector coupled to a C-band high gradient RF Linac capable to bring the electron beam up to a maximum energy of 750 MeV with outstanding beam quality [48]. An innovative C-band High Order Mode damped RF cavity has been conceived and designed in order to avoid emittance and energy spread degradation due to the Beam Break-Up (BBU) instability along the Linac over the 32 multi-bunch train. The low level RF tests successfully conducted at INFN-LNF were followed by successful high power tests with achievement of the nominal 33 MeV/m accelerating gradient in the accelerating structures with the requested rejection level of high order RF modes which are potentially dangerous for BBU [49].

Thanks to these advanced components and to many other devices developed specifically for the ELI-NP-GBS (like the collimator-characterization stage for the γ photon beam), the expected performances are at least two orders of magnitude higher than the present state of the art, in terms of bandwidth, brilliance and spectral density. These are summarized in the Table 1.1.

The lay-out of the machine is shown in Fig. 1.1. Downstream the photo-injector, a first Linac section brings the electron beam energy up to 350 MeV and a first dogleg delivers the beam to the low energy IP. The second part of the Linac raises the beam energy up to 750 MeV delivering the beam to the high energy IP through a second dogleg. The total length of the machine is about 90 m.

The completion of ELI-NP-GBS by EuroGammaS is foreseen by the end of 2018.

Table 1.1: ELI-NP-GBS expected performances: ranges for electron beam, laser pulse and γ-ray photon beam parameters are listed.

Electron beam parameters 32 bunches per RF pulse, 16 ns separation bunch-to-bunch, 100 Hz rep rate	
Mean energy [MeV]	$75 - 750$
Bunch charge [pC]	$25 - 250$
Bunch length [μm] rms	$200 - 300$
Total projected rms transverse emittance x,y [mm·mrad]	$0.3 - 0.5$
Relative rms energy spread [%]	$0.05 - 0.1$
Focal spot size x,y [μm] rms	$15 - 18$
Laser parameters 100 Hz repetition rate	
Laser pulse energy [J]	$0.2 - 0.4$
Laser wavelength [nm]	515
Laser photon energy [eV]	2.4
Laser pulse length [ps] rms	1.5
Laser focal spot size w_0 [μm]	28
Laser rms bandwidth	< 0.1
Laser M^2	< 1.2
Laser parameter a_0	$0.02 - 0.04$
Collision angle α [^{o}]	172
Laser repetition rate [Hz]	100
Recirculator rate per laser pulse	32
γ-ray Photon beam parameters	
Mean energy [MeV]	$0.2 - 19.5$
Spectral density [ph/s·eV]	$0.5 - 2 \cdot 10^4$
Relative rms bandwidth [‰]	$2 - 5$
Collimation angle [μrad]	$60 - 400$
Number photons per shot within collimation angle	$1.1 - 3.5 \cdot 10^5$
Number photons per second within collimation angle	$0.3 - 1.1 \cdot 10^9$
Source size x,y [μm] rms	$10 - 20$
Peak brilliance [ph/s·mm^2·mrad^2·0.1%]	$2 \cdot 10^{19} - 4 \cdot 10^{21}$
Radiation pulse length [ps]	$0.7 - 1$

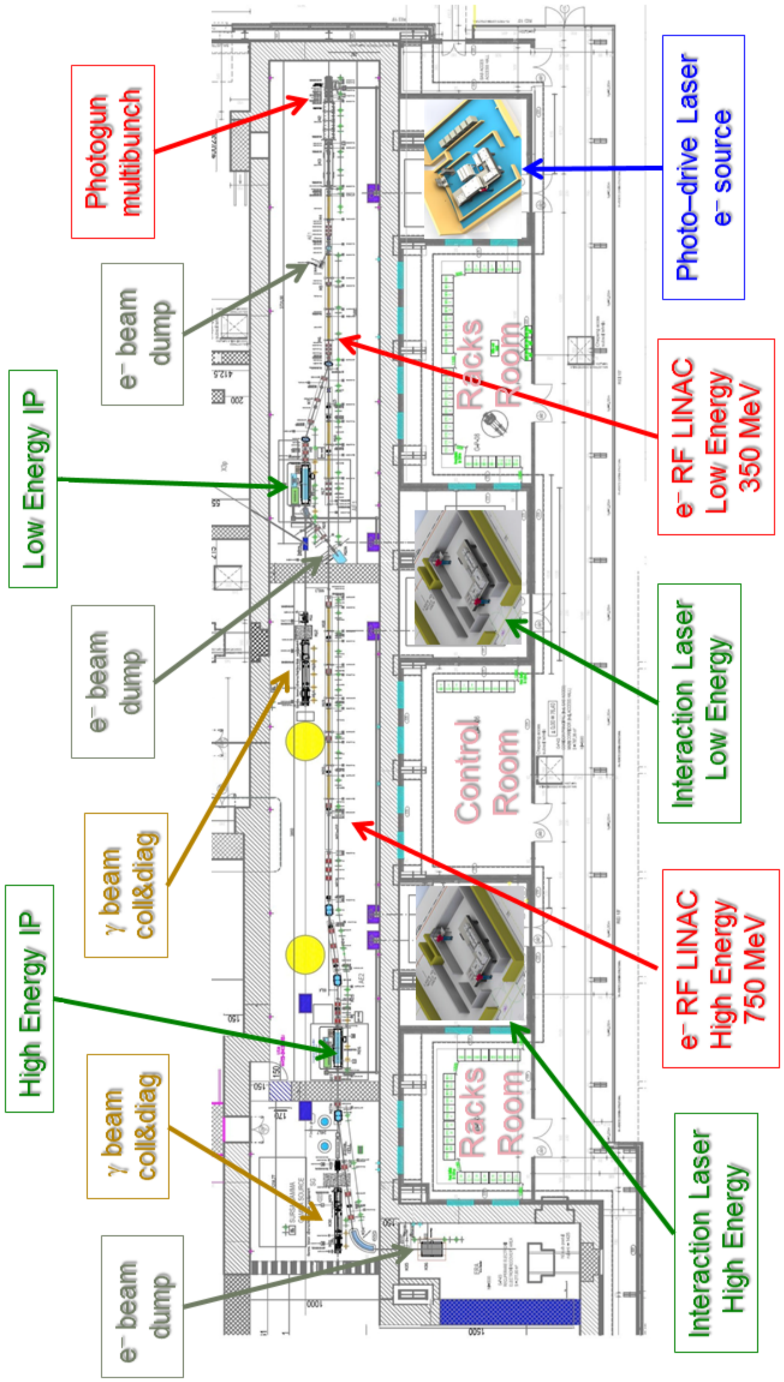

Figure 1.1: ELI-NP-GBS schematic layout.

CHAPTER 2

Inverse Compton scattering of an electron and a photon

2.1 Kinematics of the interaction

Let us consider the scattering between an electron and a photon both moving in the laboratory frame (LAB). Without loss of generality we can set the incoming electron momentum $\underline{p}_i$ along the z direction as in Fig. 2.1. The incoming photon momentum $\hbar\underline{k}_i$ draws the angle α close to 180^o with the electron's direction and the interaction occurs at the origin of the axis. After the interaction the photon is scattered with momentum $\hbar\underline{k}_f$ and angle θ, while the electron has momentum $\underline{p}_f$. In the following we will consider laser photons with energy in the range of eV and electrons of MeV-GeV energy.

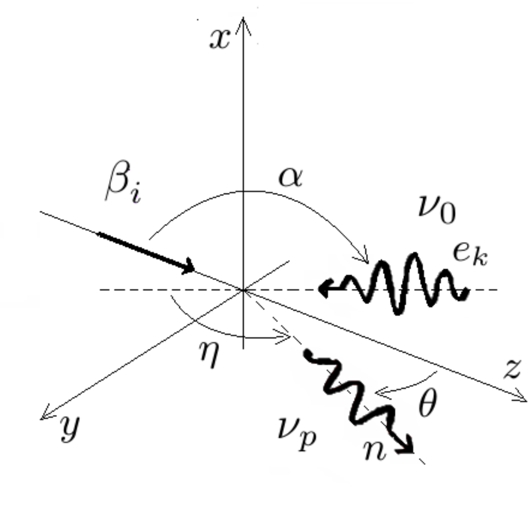

Figure 2.1: Geometry of the scattering. (x, y, z) is laboratory frame (LAB). The incoming electron moves along z while the incoming photon along e_k. The angle between their directions is α. The emitted photon has direction n which draws an angle θ with the z axis and η with e_k.

This process is an elastic scattering (the incoming and emitted particles are the same) and the total 4-momentum conservation before and after the scattering holds

$$P_i + K_i = P_f + K_f \tag{2.1}$$

where

$$P_i = \left(\frac{E_e}{c}, \underline{p}_i\right) = (\gamma_i mc, \gamma_i \underline{\beta}_i mc)$$

and

$$P_f = \left(\frac{E_s}{c}, \underline{p}_f\right) = (\gamma_f mc, \gamma_f \underline{\beta}_f mc)$$

are the incoming and emitted electrons 4-momenta, while

$$K_i = \left(\frac{h\nu_0}{c}, \hbar \underline{k}_i\right) = \left(\frac{h\nu_0}{c}, \frac{h\nu_0}{c}\underline{e}_k\right)$$

and

$$K_f = \left(\frac{h\nu_p}{c}, \hbar \underline{k}_f\right) = \left(\frac{h\nu_p}{c}, \frac{h\nu_p}{c}\underline{n}\right)$$

are the ones of the photons before and after interaction respectively. ν_0 is the frequency of the incident laser photon, $\underline{e}_k$ the unit vector of its direction, $\underline{n}$ is the direction of the scattered photon, h the Planck constant, $m = 511$ keV/c^2 the electron rest mass, $\underline{\beta}_i$ and γ_i the normalized velocity and the Lorentz factor of each electron.

By squaring both sides of eq. (2.1), after some manipulations we obtain the frequency of the emitted photon:

$$\nu_p = \nu_0 \frac{1 - \underline{e}_k \cdot \underline{\beta}_i}{1 - \underline{n} \cdot \underline{\beta}_i + \frac{h\nu_0}{\gamma_i mc^2}(1 - \underline{e}_k \cdot \underline{n})} \tag{2.2}$$

This formula describes the frequency-angle correlation, which is a typical feature of this kind of sources, and that permits to rule the bandwidth: the highest frequency of the emitted radiation is at $\theta = 0$ and decreases as shown in Fig. 2.2.
The maximum energy value corresponds to $\nu_p \simeq 4\gamma_i^2 \nu_0$ in the Thomson approximation on axis, this means that the incoming photon is boosted by a factor $4\gamma_i^2$ by the relativistic electron, therefore the emitted radiation is in the X/γ range.
If the electron and the photon are both moving along z in opposite direction, equation (2.2) becomes

$$\nu_p = \nu_0 \frac{1 + \beta_i}{1 - \beta_i + \frac{h\nu_0}{\gamma_i mc^2}(1 - \cos\eta)} \tag{2.3}$$

which is independent from the azimuthal angle. This means that at a given angle from the axis of propagation of the incoming electron, the energy is the same for every ϕ angle, i.e. the energy decreases in circles around z (see Fig. 2.3).
The last term of (2.2) in the denominator is related to the quantum red shift and gains importance as the electron energy goes into the GeV range, when the desired bandwidth

is very thin or when the laser energy is extremely high.

For example, the head-on collision of a 400 MeV electron a 515 nm (equivalent to 2.4047 eV) photon gives in the Thomson regime $h\nu_p^{max} = 4\gamma_i^2 h\nu_0 = 5.9$ MeV, while in the Compton approximation (by taking into account the electron recoil through the energy conservation) gives $h\nu_p^{max} = 5.8147$ MeV.

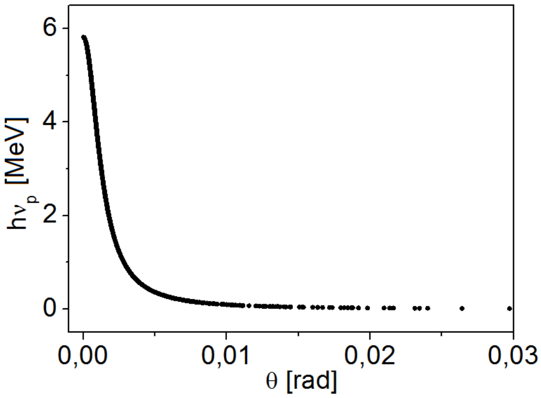

Figure 2.2: Photon energy $h\nu_p$ [MeV] as a function of the angle θ [rad] result of the scattering of an electron with 400 MeV energy and a laser of 515 nm wavelength.

The distributions of the radiation total energy a) and the intensity of the emitted radiation b) as a function of the normalized photon frequency $\nu = \nu_p/(4\nu_0\gamma_i^2)$ are shown in Fig. 2.4. We notice that the spectrum of the radiation is very broad, but the energy angle correlation permits to obtain an almost monochromatic spectrum by selecting the part of the radiation in a narrow θ angle.

It is also interesting to express eq. (2.2) in terms of wavelength:

$$\boldsymbol{\lambda}_p = \boldsymbol{\lambda}_0 \frac{1 - \underline{n} \cdot \underline{\beta}_i}{1 - \underline{e}_k \cdot \underline{\beta}_i} + \frac{h}{\gamma_i mc} \frac{1 - \underline{e}_k \cdot \underline{n}}{1 - \underline{e}_k \cdot \underline{\beta}_i}. \tag{2.4}$$

The first term on the right side of eq. (2.4) represents the classical Thomson effect, while the second part describes the shift due to the electron recoil after the scattering.
We can also write eq. (2.4) in terms of the angles (see Fig. 2.1) as

$$\lambda_p = \lambda_0 \left(\frac{1 - \beta_i \cos\theta}{1 - \beta_i \cos\alpha} \right) + \frac{h}{\gamma_i mc} \left(\frac{1 - \cos\eta}{1 - \beta_i \cos\alpha} \right).$$

The wavelength shift $\boldsymbol{\lambda}_p$ of the emitted photon is minimum (maximum energy gain) when the incoming electron and photon are perfectly counter-propagating, i.e. $\alpha = \pi$. Under this hypothesis, the radiation emitted along the incoming electron direction (at

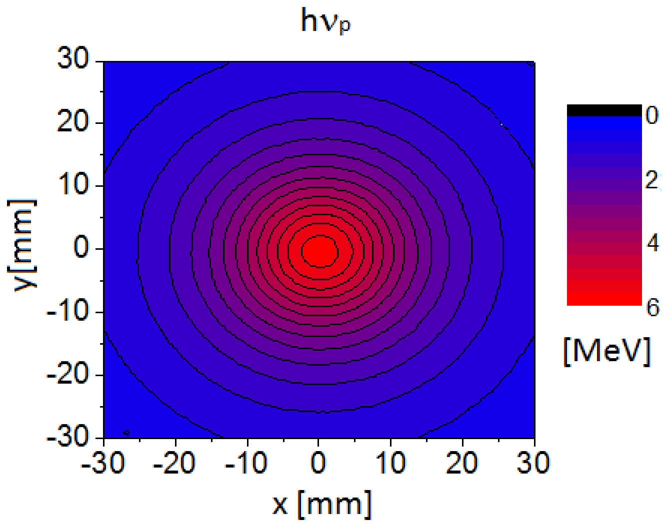

Figure 2.3: Photon energy $h\nu_p$ distribution on a screen perpendicular to the z axis at 10 m downstream the interaction point, result of the scattering of an electron with 400 MeV energy and a laser of 515 nm wavelength.

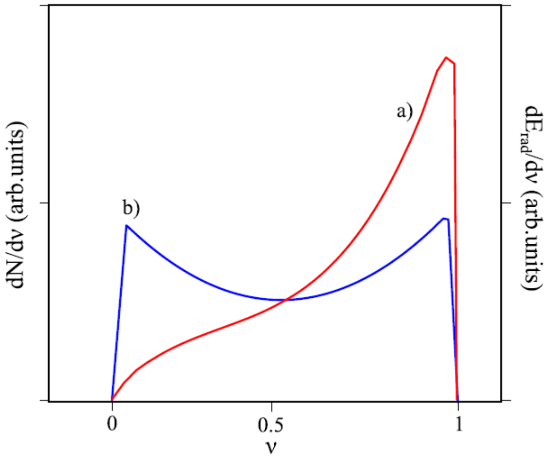

Figure 2.4: Photon energy a) and photon number b) distributions as function of the normalized photon frequency.

$\theta = 0$) in the relativistic limit of $\beta_i \to 1$ is

$$\boldsymbol{\lambda}_p = \boldsymbol{\lambda}_0 \frac{1-\beta_i^2}{(1+\beta_i)^2} + \frac{h}{\gamma_i mc}\frac{2}{1+\beta_i} \simeq \frac{\boldsymbol{\lambda}_0}{4\gamma_i^2} + \frac{h}{\gamma_i mc} = \boldsymbol{\lambda}_T + \boldsymbol{\lambda}_R. \tag{2.5}$$

The recoil, quantum effect, term $\boldsymbol{\lambda}_R$ goes to zero slower than the classical one $\boldsymbol{\lambda}_T$ as γ_i grows, and at high values of γ_i it is even dominant as shown in graph a) of Fig. 2.5. In our range of interest (up to 1 GeV) the Thomson effect is definitely the dominant effect (see graph b)) and the recoil effect, as reported in graph c), is of the order of $\boldsymbol{\lambda}_R/\boldsymbol{\lambda}_p \simeq 0.01 - 0.03$.

Calculating eq. (2.5) for some ELI-NP typical values, $\gamma_i = 700$, 1500 and $\boldsymbol{\lambda}_0 = 515$ nm, we obtain the values reported in the Table 2.1.

Table 2.1: Values of $\boldsymbol{\lambda}_T$, $\boldsymbol{\lambda}_R$ and $\boldsymbol{\lambda}_p$ [m], for $\gamma_i = 700, 1500$ and $\boldsymbol{\lambda}_0 = 515$ nm.

γ_i	$\boldsymbol{\lambda}_T$ [m]	$\boldsymbol{\lambda}_R$ [m]	$\boldsymbol{\lambda}_p$ [m]
700	$2.958 \cdot 10^{-13}$	$3.726 \cdot 10^{-15}$	$2.995 \cdot 10^{-13}$
1500	$5.945 \cdot 10^{-14}$	$1.670 \cdot 10^{-15}$	$6.112 \cdot 10^{-14}$

We notice that to neglect the recoil effect causes some percent shift in the wavelength value, which is not a small shift compared to the relative bandwidth of 0.5% or even less desired for the ELI-NP experiment.

2.2 Scattering cross section

Once a certain reaction is observed or predicted by the theory, the major concern is to establish the probability of it to happen given the initial particles energies and momenta (total cross section) and more into details, the probability that the particles are emitted at specific angles (differential cross section). By integrating over the solid angle the latter one we obtain the total cross section.

The first attempt of writing the electron-photon cross section was performed by Klein and Nishina [52]: starting from the Dirac equation and assuming an interaction Hamiltonian based on a classical electromagnetic potential, they deduced the cross section in the electron rest frame. This cross section σ_{KN} describes the Compton effect observed in the first experiments [53] performed by illuminating with a Röntgen produced X radiation a graphite thin target, in which the electrons are considered at rest.
A similar calculation is performed in Ref. [54] with the potential written as the sum of a finite number of monochromatic plane waves. The time integration of the plane waves leads to a Dirac delta in the matrix elements. The passage to the transition probability involves the squaring of the delta function, which is problematic procedure under the

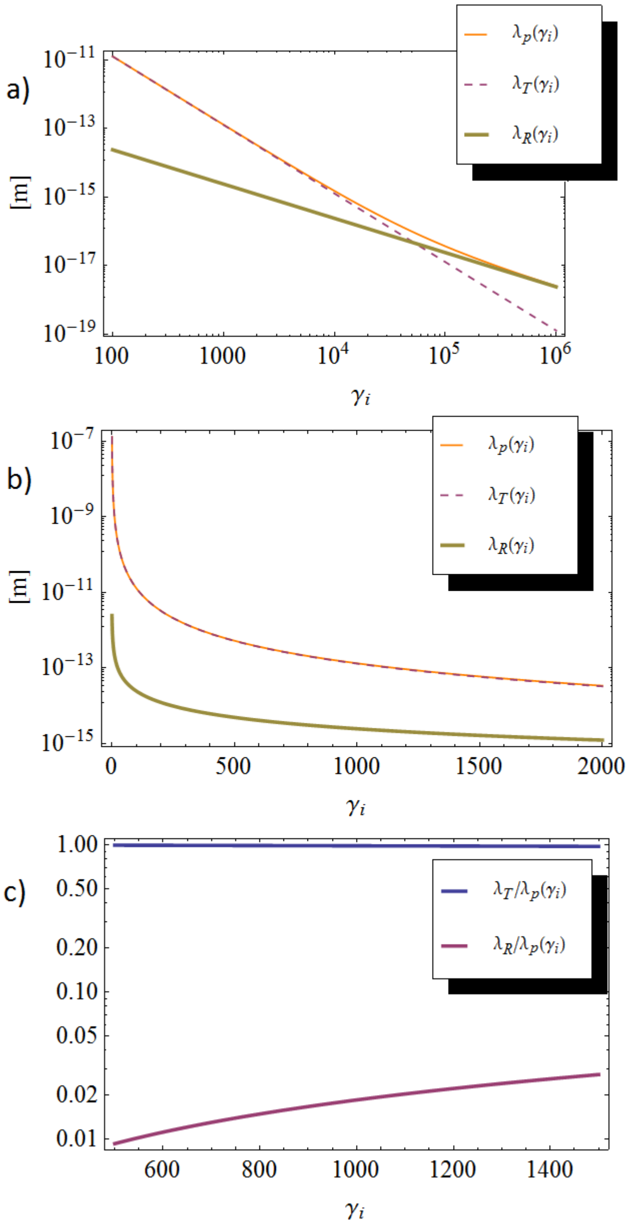

Figure 2.5: Wavelength of the emitted photon $\boldsymbol{\lambda}_p$ [m] as a function of γ_i, for $\boldsymbol{\lambda}_0 = 0.515\,\mu m$. The contributes of the Thomson effect only $\boldsymbol{\lambda}_T$ and of the electron recoil $\boldsymbol{\lambda}_R$ [m] are also shown.

mathematical point of view.

The analysis of scattering experiments between electron and photon beams, requires the use of the scattering cross section for electron-photon particles both in motion. Since the theory is relativistic, the result expressed by the Klein and Nishina formula is supposed to be generalized to the case $\underline{p}_i \neq 0$ with an appropriate Lorentz transformation. This transformation acts on the photon's 4-momentum K and polarization vectors $\epsilon_\lambda(k)$ with $\lambda = 0, 1, 2, 3$, which are related to the plane waves of the electromagnetic field potential $A^\mu(x,t)$. In each inertial frame, only the vectors whose index is $\lambda = 1, 2$ correspond to physical photons. This choice is not covariant: for this reason the Lorentz transformation has to be associated to a gauge transformation or it is necessary to consider the transformation law of the electromagnetic field's tensor and to write the electric field through the vectors $\epsilon_\lambda(k)$.

Such dissertation is reported in Jauch-Roerlich [55] following the Feynman-Dyson diagrams method.

An alternative method is presented in Ref. [56], where the Klein and Nishina expression is transformed to laboratory frame where both particles are moving by using the Lorentz transformations.

The [59] approach is similar to the latter one, except the fact that the Lorentz transformations are applied to the electric field instead that to the vector potential, avoiding the necessity of a gauge transformation (see B).

In the following we resume the results of the [60] method based on Dyson-Feynman diagrams and Mandelstam invariants, which constitutes the theoretical framework of the Monte Carlo code CAIN [61,62] we use for our simulations.

In appendix A, we present a rigorous method to obtain the inverse Compton cross section in the general case of not null initial momentum of the electrons from a pure QED calculation, avoiding the usual approaches based on the derivation of this cross section either from the Klein and Nishina formula and the Lorentz transformations or through Dyson-Feynman diagrams and Mandelstam invariants.

2.2.1 Unpolarized differential cross section

The differential cross section for an unpolarized photon by an unpolarized electron, without regard to their polarization after the scattering is given by [60]

$$d\sigma = 8\pi r_e^2 \frac{(mc)^2 dt}{(s-(mc)^2)^2} \left[\left(\frac{(mc)^2}{s-(mc)^2} + \frac{(mc)^2}{u-(mc)^2} \right)^2 + \left(\frac{(mc)^2}{s-(mc)^2} + \frac{(mc)^2}{u-(mc)^2} \right) - \frac{1}{4} \left(\frac{s-(mc)^2}{u-(mc)^2} + \frac{u-(mc)^2}{s-(mc)^2} \right) \right] \quad (2.6)$$

where s, t, u are the Lorentz invariant quantities called Mandelstam invariants defined as

$$\begin{cases} s = (P_i + K_i)^2 = (P_f + K_f)^2 = (mc)^2 + 2P_iK_i = (mc)^2 + 2P_fK_f \\ t = (P_i - P_f)^2 = (K_f - K_i)^2 = 2((mc)^2 - P_iP_f) = -2K_iK_f \\ u = (P_i - K_f)^2 = (P_f - K_i)^2 = (mc)^2 - 2P_iK_f = (mc)^2 - 2P_fK_i \\ s + t + u = 2(mc)^2 \end{cases} \tag{2.7}$$

with P_i, K_i, P_f and K_f the 4-momenta satisfying eq. (2.1).

This equation expresses the cross section in terms of invariant quantities, allowing therefore to write it easily in terms of the collision parameters in any reference frame.

In the laboratory frame in which the electron is at rest before the collision (ERF), $P_i = (mc, 0, 0, 0)$, the Mandelstam invariants are

$$s - (mc)^2 = 2mh\nu_0' \qquad u - (mc)^2 = -2mh\nu_p' \qquad t = -\frac{2h^2\nu_0'\nu_p'}{c^2}(1 - \cos\theta') \tag{2.8}$$

and eq. (2.2) gives in this frame ($\underline{\beta}_i = 0$, $\gamma_i = 1$)

$$\nu_p' = \nu_0' \frac{1}{1 + \frac{h\nu_0'}{mc^2}(1 - \cos\theta')} \tag{2.9}$$

where ν_0' and ν_p' are the photon frequencies before and after scattering in ERF and θ' the angle between their directions (see Fig. 2.6).

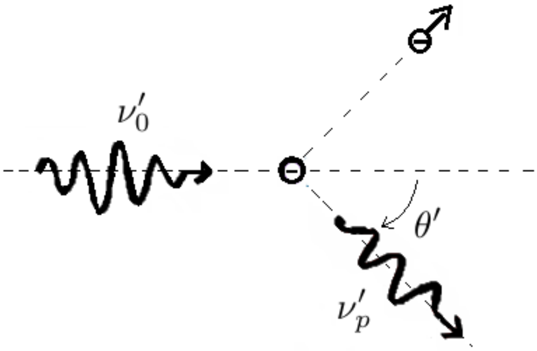

Figure 2.6: Scattering geometry in ERF: the incoming photon of frequency ν_0' hits the electron at rest, the electron is scattered and the emitted photon has frequency ν_p' and its direction forms an angle θ' with the incoming photon one.

By using eq. (2.9) we obtain

$$dt = -\frac{2h^2{\nu_p'}^2}{c^2} d\cos\theta' = \frac{2h^2{\nu_p'}^2}{c^2} \sin\theta' d\theta'.$$

If we plug all of these equations in (2.6) we obtain the Klein-Nishina differential cross section [52]

$$\frac{d\sigma}{d\Omega'} = \frac{r_e^2}{2}\left(\frac{\nu_p'}{\nu_0'}\right)^2\left(\frac{\nu_0'}{\nu_p'} + \frac{\nu_p'}{\nu_0'} - \sin^2\theta'\right) \tag{2.10}$$

with $d\Omega' = sin\theta' d\theta' d\phi'$. Since eq. (2.9) sets a biunivocal correspondence between frequency and angle in ERF, the cross section can be expressed in terms of θ' as

$$\begin{aligned}\frac{d\sigma}{d\theta' d\phi'} = r_e^2\left(\frac{2}{2+\Delta(1-cos\theta')}\right)^2\left(\frac{1+cos^2\theta'}{2}\right)\cdot \\ \left(1+\frac{\Delta^2(1-cos\theta')^2}{2(1+cos^2\theta')(2+\Delta(1-cos\theta'))}\right) sin\theta'\end{aligned} \tag{2.11}$$

where

$$\Delta = 2h\nu_0'/mc^2 \tag{2.12}$$

is the parameter describing the effect of the recoil of the electron on the emitted radiation frequency value. Equation (2.9) also determines the limit values for the energy of the emitted photon in ERF:

$$\begin{cases} h{\nu'}_p^{max} = h\nu_0' & \text{for} \quad \theta' = 0 \\ h{\nu'}_p^{min} = \dfrac{h\nu_0'}{1+\Delta} & \text{for} \quad \theta' = \pi. \end{cases} \tag{2.13}$$

If the energy of the incoming photon is much smaller than the electron rest mass, i.e. $h\nu_0' \ll mc^2$ or $\Delta \ll 1$, then $h\nu_p' \approx h\nu_0'$ and (2.10) turns into the classical Thomson formula.

The total cross section can be obtained from eq. (2.11) by integrating over θ' and ϕ'

$$\sigma_{tot} = 2\pi r_e^2 \frac{1}{\Delta}\left[\left(1-\frac{4}{\Delta}-\frac{8}{\Delta^2}\right)\log(1+\Delta)+\frac{1}{2}+\frac{8}{\Delta}-\frac{1}{2(1+\Delta)^2}\right] \tag{2.14}$$

and

$$\begin{cases} \lim\limits_{\Delta\to 0}\sigma_{tot} = \dfrac{8\pi r_e^2}{3}(1-\Delta) = \sigma_T(1-\Delta) & \text{non-relativistic case} \\ \lim\limits_{\Delta\to\infty}\sigma_{tot} = \dfrac{2\pi r_e^2}{\Delta}\left(\log\Delta+\dfrac{1}{2}\right) & \text{ultra-relativistic case.} \end{cases} \tag{2.15}$$

For example, the recoil parameter Δ associated with the head-on scattering of an electron at $E_e = 400$ MeV and a photon with $h\nu_0 = 2.4047$ eV (these energies are in LAB) is given by

$$\Delta = \frac{2h\nu_0'}{mc^2} = \frac{4\gamma_i h\nu_0}{mc^2} = 7.37\cdot 10^{-3}$$

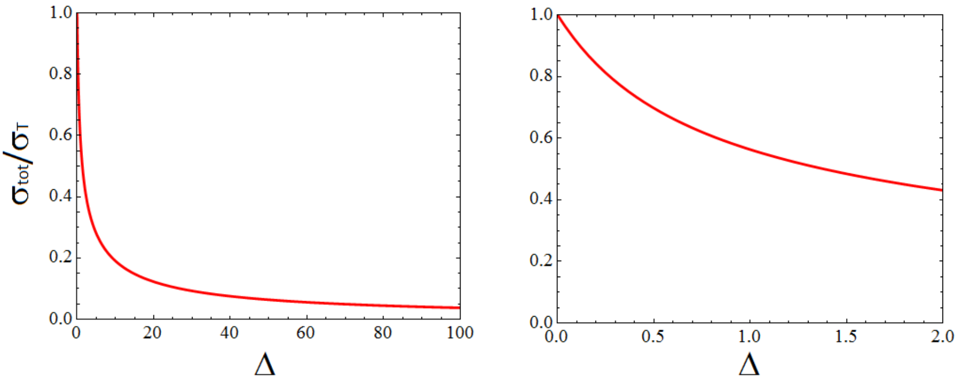

Figure 2.7: Total Compton cross section normalized by the total Thomson cross section as a function of the recoil parameter Δ.

since the relativistic Döppler effect rules the transformation of the photon energy from LAB to ERF by means of the formula

$$h\nu_0' = h\nu_0\gamma_i(1 - \underline{\beta}_i \cdot \underline{e}_k). \tag{2.16}$$

The differential cross section shape as a function of the angle θ' in ERF, which is the angle between the incoming and the emitted photon directions, is reported in Fig. 2.8 for different values of the recoil parameter Δ.

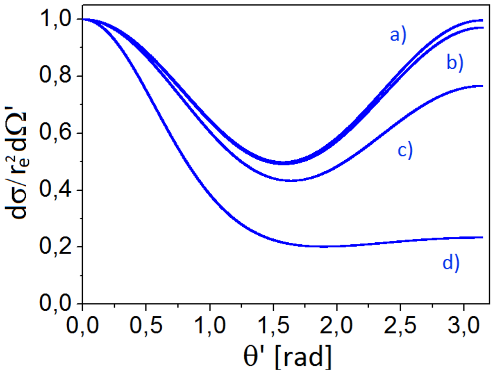

Figure 2.8: Differential Compton cross section $d\sigma/d\Omega'$ in ERF normalized by r_e^2 as a function of θ' [rad] for different values of Δ: $7.37 \cdot 10^{-4}$ a), $7.37 \cdot 10^{-3}$ b), $7.37 \cdot 10^{-2}$ c), 0.737 d).

2.2.2 Polarized differential cross section

The Lorentz invariant form for the differential cross section for an unpolarized electron with a polarized photon is [60]

$$\begin{aligned}\frac{d\sigma}{dY d\phi} = \frac{2r_e^2}{X^2}\Bigg\{&\left(\frac{1}{X}-\frac{1}{Y}\right)^2 + \frac{1}{X} - \frac{1}{Y} + \frac{1}{4}\left(\frac{X}{Y}+\frac{Y}{X}\right) - \\ &(S_3^i+\tilde{S}_3)\left[\left(\frac{1}{X}-\frac{1}{Y}\right)^2+\frac{1}{X}-\frac{1}{Y}\right] + S_1^i\tilde{S}_1\left(\frac{1}{X}-\frac{1}{Y}+\frac{1}{2}\right) + \\ &S_2^i\tilde{S}_2\frac{1}{4}\left(\frac{X}{Y}+\frac{Y}{X}\right)\left(1+\frac{2}{X}-\frac{2}{Y}\right)+S_3^i\tilde{S}_3\left[\left(\frac{1}{X}-\frac{1}{Y}\right)^2+\frac{1}{X}-\frac{1}{Y}+\frac{1}{2}\right]\Bigg\}\end{aligned} \qquad (2.17)$$

where X and Y are the Lorentz invariant quantities defined as

$$X = \frac{s-(mc)^2}{(mc)^2} \qquad\qquad Y = \frac{u-(mc)^2}{(mc)^2} \qquad (2.18)$$

and $\underline{S}^i$, $\underline{\tilde{S}}$ are the Stokes parameters described in the following.

$\underline{S}^i = (S_1^i, S_2^i, S_3^i)$ are the Stokes parameters of the incoming photon defined in the coordinate system given by the right-handed orthonormal basis ($\underline{e}_1$, $\underline{e}_2$, $\underline{e}_k$). $\underline{e}_k$ is the direction of the incoming photon, $\underline{e}_1$ the versor perpendicular to the scattering plane

$$\underline{e}_1 = \frac{\underline{k}_i \times \underline{k}_f}{|\underline{k}_i \times \underline{k}_f|} \qquad (2.19)$$

and the versor $\underline{e}_2$ is given by

$$\underline{e}_2 = \frac{\underline{k}_i \times \underline{e}_1}{|\underline{k}_i \times \underline{e}_1|}. \qquad (2.20)$$

The polarization vector $\underline{\epsilon}$ of the incoming photon, lies in the plane orthogonal to $\underline{e}_k$ and can therefore be written as

$$\underline{\epsilon} = (\underline{\epsilon}\cdot\underline{e}_1)\underline{e}_1 + (\underline{\epsilon}\cdot\underline{e}_2)\underline{e}_2 = \epsilon_1\underline{e}_1 + \epsilon_2\underline{e}_2. \qquad (2.21)$$

The Stokes parameters $\underline{S}^i$ are defined by the following relation with the photon density matrix [67]

$$\rho = \begin{pmatrix} \epsilon_1^2 & \epsilon_1\epsilon_2^* \\ \epsilon_2\epsilon_1^* & \epsilon_2^2 \end{pmatrix} = \frac{1}{2}\begin{pmatrix} 1+S_3^i & S_1^i - iS_2^i \\ S_1^i + iS_2^i & 1-S_3^i \end{pmatrix}. \qquad (2.22)$$

Each parameter has value between 1 and -1 and they represent

- $S_1^i = \epsilon_1\epsilon_2^* + \epsilon_2\epsilon_1^* \rightarrow$ linear polarization along the direction $\frac{\underline{e}_1+\underline{e}_2}{\sqrt{2}}$ or $\frac{\underline{e}_1-\underline{e}_2}{\sqrt{2}}$;
- $S_2^i = i(\epsilon_1\epsilon_2^* - \epsilon_2\epsilon_1^*) \rightarrow$ circular polarization clockwise or counterclockwise;

- $S_3^i = \epsilon_1^2 - \epsilon_2^2 \rightarrow$ linear polarization along the direction $\underline{e}_1$ or $\underline{e}_2$.

$\underline{\tilde{S}}$ are the Stokes parameters describing which would be the polarization of the emitted photon if it was measured by a detector, not the final polarization of the photon itself. $\underline{\tilde{S}}$ are defined in the coordinate system given by the right-handed orthonormal basis ($\underline{\tilde{e}}_1$, $\underline{\tilde{e}}_2$, $\underline{n}$).
The final polarization of the emitted photon will be discussed in the next section and it will be described by the Stokes parameters $\underline{S}$.

If we disregard the polarization of the emitted photon, by averaging and summing over the emitted photon polarizations (setting $\tilde{S}_{1,2,3} = 0$ in eq. (2.17) and multiplying by 2 the result), the cross section becomes

$$\frac{d\sigma}{dY d\phi} = \frac{4r_e^2}{X^2} \left\{ (1 - S_3^i) \left[\left(\frac{1}{X} - \frac{1}{Y} \right)^2 + \frac{1}{X} - \frac{1}{Y} \right] + \frac{1}{4} \left(\frac{X}{Y} + \frac{Y}{X} \right) \right\}. \tag{2.23}$$

and it only depends on S_3^i.

As we said, S_3^i is defined with respect to a coordinate system defined by the scattering plane. If we consider the head-on scattering of a photon and an electron propagating along z, any possible scattering plane is univocally defined by the z axis and the azimuthal angle ϕ calculated counter-clockwise starting from the x axis (see Fig. refscattplane).

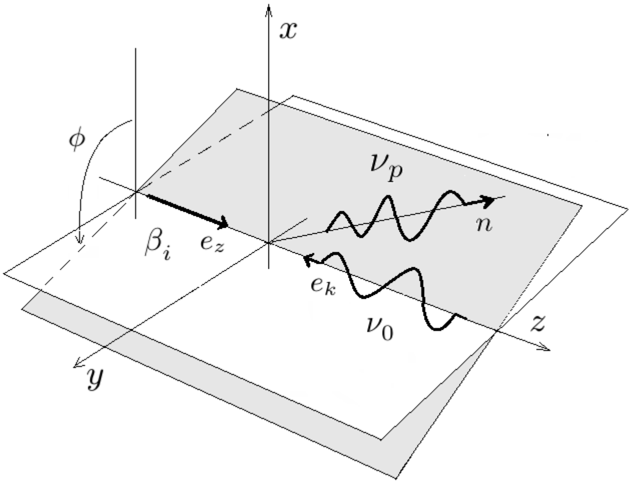

Figure 2.9: Geometry of the interaction. The incoming electron moves along e_z while the incoming photon is characterized by $e_k = -e_z$. The emitted photon has direction n which, together with e_k, defines the scattering plane. The angle between the scattering plane and the x axis is the azimuthal angle ϕ.

Since the polarization 3-vector $\underline{\epsilon}$ is orthogonal to the photon momentum direction $\underline{e}_k = -\underline{e}_z$, if the incoming photon is linearly polarized, $\underline{\epsilon}$ can be expressed in the laboratory frame as

$$\underline{\epsilon} = \cos\tau \underline{e}_x + \sin\tau \underline{e}_y \tag{2.24}$$

in terms of the azimuthal angle τ of the polarization vector calculated counter-clockwise starting from the x axis as shown in Fig. 2.10.

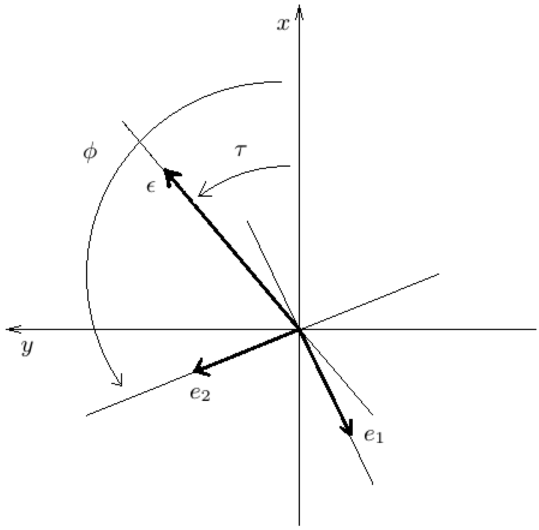

Figure 2.10: Scattering geometry in the transverse plane x, y (the z axis exits the page). The angle between the x axis and polarization vector ϵ calculated counter-clockwise is τ.

By inserting eq. (2.24) into eq. (2.21) we obtain

$$\epsilon_1 = -\sin(\tau - \phi) \qquad\qquad \epsilon_2 = -\cos(\tau - \phi). \tag{2.25}$$

and we can therefore express the Stokes parameters $\underline{S}^i$ in terms of the LAB reference frame versors ($\underline{e}_x$, $\underline{e}_y$, $\underline{e}_z$):

$$S_1^i = \mathbf{P_l}\sin(2\tau - 2\phi), \qquad S_2^i = \mathbf{P_c}, \qquad S_3^i = -\mathbf{P_l}\cos(2\tau - 2\phi) \tag{2.26}$$

where $\mathbf{P_l}$ and $\mathbf{P_c}$ are the degrees of linear and circular polarization of the incident photon.

Plugging eq. (2.26) in eq. (2.23) we obtain

$$\frac{d\sigma}{dY d\phi} = \frac{4r_e^2}{X^2}\left\{(1 + \mathbf{P_l}\cos(2\tau - 2\phi))\left[\left(\frac{1}{X} - \frac{1}{Y}\right)^2 + \frac{1}{X} - \frac{1}{Y}\right] + \frac{1}{4}\left(\frac{X}{Y} + \frac{Y}{X}\right)\right\}. \tag{2.27}$$

We can notice that the differential cross section has different behaviors depending on the polarization of the incoming photon: if the incoming photon is linearly polarized, i.e. $\mathbf{P}_l \neq 0$, the differential cross section depends on the azimuthal angle and it is therefore asymmetric in ϕ; otherwise (for unpolarized or circular polarized incoming photon) it is symmetric in ϕ. In Fig. 2.11 is reported the intensity of the radiation on a screen at 10 m from IP produced by the scattering of a 400 MeV electron colliding head-on with a laser circularly polarized (left) and linearly polarized in y ($\tau = \pi/2$) direction (right).

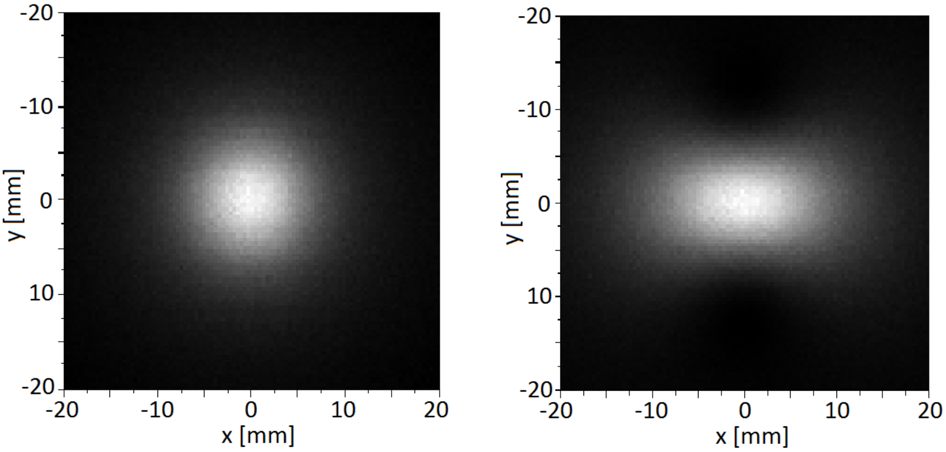

Figure 2.11: Intensity of the emitted radiation on a screen at 10 m from the IP due to the interaction between a 400 MeV electron and 515 nm wavelength photon beam with circular polarization (left) and linear polarization along y (right). The units for x and y are mm.

2.3 Polarization of the emitted photon

The polarization of the emitted photons can be obtained by using a quantum model with the same approach adopted in the precedent section (an alternative quantum approach leading to the same results is reported in Appendix B). We also report a classical model.

2.3.1 Quantum model

The differential cross section (2.17) can be rewritten as

$$\frac{d\sigma}{dY d\phi} = \frac{2r_e^2}{X^2}\left(F_0 + \sum_{i=1}^{3} F_i \tilde{S}_i\right) \tag{2.28}$$

$\underline{\tilde{S}}$ are the Stokes parameters describing which would be the polarization of the emitted photon if it was measured by a detector, they depend on the detectors setup. The term $\sum_{i=1}^{3} F_i \tilde{S}_i$ means that if one observes the polarization $\underline{s}$, the probability to be found in a state $\pm\underline{s}$ is given by [60,62]

$$\frac{2r_e^2}{X^2}\left(F_0+\sum_{i=1}^{3}F_i s_i\right).$$

The final polarization of the emitted photon, ones the energy $h\nu_p$ and the azimuthal angle ϕ are defined, is

$$\underline{S}=\frac{F_i(h\nu_p,\phi)}{F_0(h\nu_p,\phi)}. \tag{2.29}$$

Let us consider again the head-on scattering depicted in Fig. 2.24. If we also take into account the fact that the θ angle is small in the relativistic case, especially for the most energetic photons, we can write [38] the Stokes parameters $\tilde{S}_i$ as a function of $\hat{S}_i$ which are the same parameters expressed in the ($\underline{e}_x$, $\underline{e}_y$, $\underline{e}_z$) frame (basically it is a rotation around z):

$$\begin{aligned}\tilde{S}_1 &\approx -\hat{S}_1\cos 2\phi+\hat{S}_3\sin 2\phi\\ \tilde{S}_2 &\approx \hat{S}_2\\ \tilde{S}_3 &\approx -\hat{S}_1\sin 2\phi-\hat{S}_3\cos 2\phi\end{aligned} \tag{2.30}$$

By substituting eq. (2.26) and (2.30) in (2.28) we have

$$\frac{d\sigma}{dYd\phi}=\frac{2r_e^2}{X^2}\left(\Phi_0+\sum_{i=1}^{3}\Phi_i\hat{S}_i\right) \tag{2.31}$$

where

$$\begin{aligned}\Phi_0 =&\left(\frac{1}{X}-\frac{1}{Y}\right)^2+\frac{1}{X}-\frac{1}{Y}+\frac{1}{4}\left(\frac{X}{Y}+\frac{Y}{X}\right)+\\ &\mathbf{P_l}\cos(2\tau-2\phi)\left[\left(\frac{1}{X}-\frac{1}{Y}\right)^2+\frac{1}{X}-\frac{1}{Y}\right]\\ \Phi_1 =&\left[\left(\frac{1}{X}-\frac{1}{Y}\right)^2+\frac{1}{X}-\frac{1}{Y}+\frac{1}{2}\right]\mathbf{P_l}\cos(2\tau-2\phi)\sin 2\phi-\\ &\left[\frac{1}{X}-\frac{1}{Y}+\frac{1}{2}\right]\mathbf{P_l}\sin(2\tau-2\phi)\cos 2\phi+\left[\left(\frac{1}{X}-\frac{1}{Y}\right)^2+\frac{1}{X}-\frac{1}{Y}\right]\sin 2\phi\\ \Phi_2 =&\frac{1}{4}\left(\frac{X}{Y}+\frac{Y}{X}\right)\left(1+\frac{2}{X}-\frac{2}{Y}\right)\mathbf{P_c}\\ \Phi_3 =&\left[\left(\frac{1}{X}-\frac{1}{Y}\right)^2+\frac{1}{X}-\frac{1}{Y}+\frac{1}{2}\right]\mathbf{P_l}\cos(2\tau-2\phi)\cos 2\phi+\\ &\left[\frac{1}{X}-\frac{1}{Y}+\frac{1}{2}\right]\mathbf{P_l}\sin(2\tau-2\phi)\sin 2\phi+\left[\left(\frac{1}{X}-\frac{1}{Y}\right)^2+\frac{1}{X}-\frac{1}{Y}\right]\cos 2\phi\end{aligned} \tag{2.32}$$

Finally, the emitted photon final polarization expressed through the Stokes parameters in the LAB frame is given by

$$\underline{S}=\frac{\Phi_i(h\nu_p,\phi)}{\Phi_0(h\nu_p,\phi)}. \tag{2.33}$$

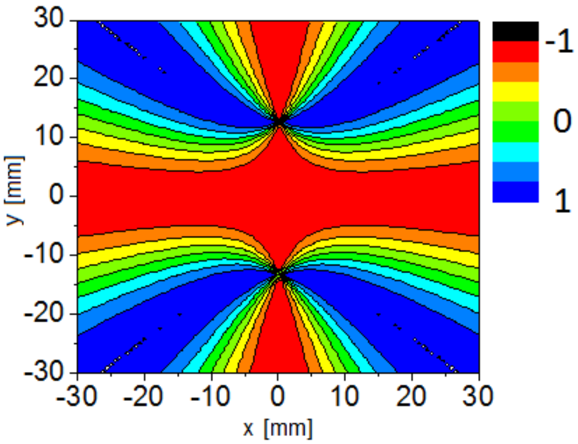

Figure 2.12: Stoke parameter $\langle S_3 \rangle$. Laser polarization: $\tau = \pi/2$ and $\mathbf{P}_1 = 1$ ($S = (0, 0, -1)$). Transverse distribution on a screen at 10 m from the IP. x, y coordinates expressed in mm.

2.3.2 Classical model

In the classical model [63], the electric field of the radiation in the far field approximation is given by:

$$\underline{E} = \frac{e}{c} \left[\frac{\underline{n} \times ((\underline{n} - \underline{\beta}_i) \times \dot{\underline{\beta}}_i)}{(1 - \underline{\beta}_i \cdot \underline{n})^3 R} \right]_{ret} \tag{2.34}$$

where $\underline{n} = (sin\theta cos\phi, sin\theta sin\phi, cos\theta)$ is the direction of the observer at distance R, $\underline{\beta}_i$ and $\dot{\underline{\beta}}_i$ are respectively the velocity and the acceleration of the electron, and the expression is calculated at the retarded time.

The motion equation can be cast in the form:

$$\dot{\underline{\beta}}_i = -\frac{e}{mc\gamma_i} \left[\underline{E}_L \left(1 - \underline{\beta}_i \cdot \underline{e}_k \right) + \underline{\beta}_i \cdot \underline{E}_L (\underline{e}_k - \underline{\beta}_i) \right]$$

where $\underline{E}_L$ is the laser electric field. If the laser propagation direction is along z ($\underline{e}_k = -\underline{e}_z$) and its polarization linear and directed along y, the acceleration is proportional to the vector

$$\underline{\lambda} = \underline{e}_y (1 + \beta_z) + \beta_y (-\underline{e}_z - \underline{\beta}_i).$$

Supposing for the sake of simplicity $\underline{\beta}_i = \beta_z \underline{e}_z$, in the linear limit (the velocity is considered not altered by the scattering) we obtain:

$$\begin{aligned} &\underline{n} \times ((\underline{n} - \underline{\beta}_i) \times \underline{\lambda}) = \\ &\quad (1 + \beta_z) \left[\underline{e}_y (-n_x^2 - n_z (n_z - \beta_z)) + \underline{e}_x n_x n_y + \underline{e}_z n_x (n_z - \beta_z) \right]. \end{aligned} \tag{2.35}$$

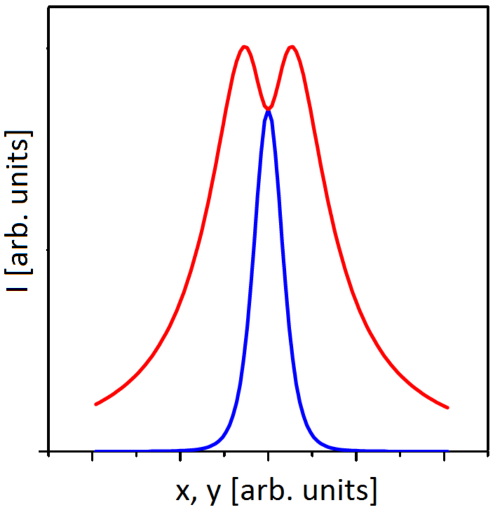

Figure 2.13: Distribution of the radiation intensity along x (red) and y (blue).

The asymmetry of the radiation spot can therefore be deduced directly from (2.35), because:

$$|E|^2(x,y=0) = \frac{4e^4E_L^2}{m^2c^4\gamma_i^2(1-\beta_z\frac{z}{R})^6R^2}\left(-\frac{1}{2\gamma_i^2}+\frac{y^2}{R^2}\right)^2 \tag{2.36}$$

while:

$$|E|^2(x=0,y) = \frac{e^4E_L^2}{m^2c^4\gamma_i^6(1-\beta_z\frac{z}{R})^6R^2}. \tag{2.37}$$

In Fig. 2.13 the profiles of the radiation along x and y are shown.
The relevant Stokes parameter S_3 is therefore:

$$S_3 = \frac{|E_x|^2-|E_y|^2}{|E|^2} = \frac{-\frac{1}{\gamma_i^4}-\frac{2}{\gamma_i^2}sin^2\theta cos2\phi - sin^4\theta cos4\phi}{\frac{1}{\gamma_i^4}+\frac{2}{\gamma_i^2}sin^2\theta cos2\phi + sin^4\theta} \tag{2.38}$$

and it vanishes at $z=R$ along the four curves:

$$y = \pm x \pm \sqrt{2x^2+\frac{R^2}{\gamma_i^2}} \tag{2.39}$$

Formula 2.38 can be analyzed in the limit $\theta \ll 1/\gamma_i$ ($\gamma_i sin\theta \ll 1$) giving:

$$S_3 = -\left[1-3\gamma_i^4 sin^4\theta(1-cos4\phi)\right] \tag{2.40}$$

while, if $\theta \geq 1/\gamma_i$ ($\gamma_i sin\theta \gg 1$)

$$S_3 = -\left[cos4\phi - +\frac{cos2\phi}{\gamma_i^2 sin^2\theta}(1-cos4\phi)\right] \tag{2.41}$$

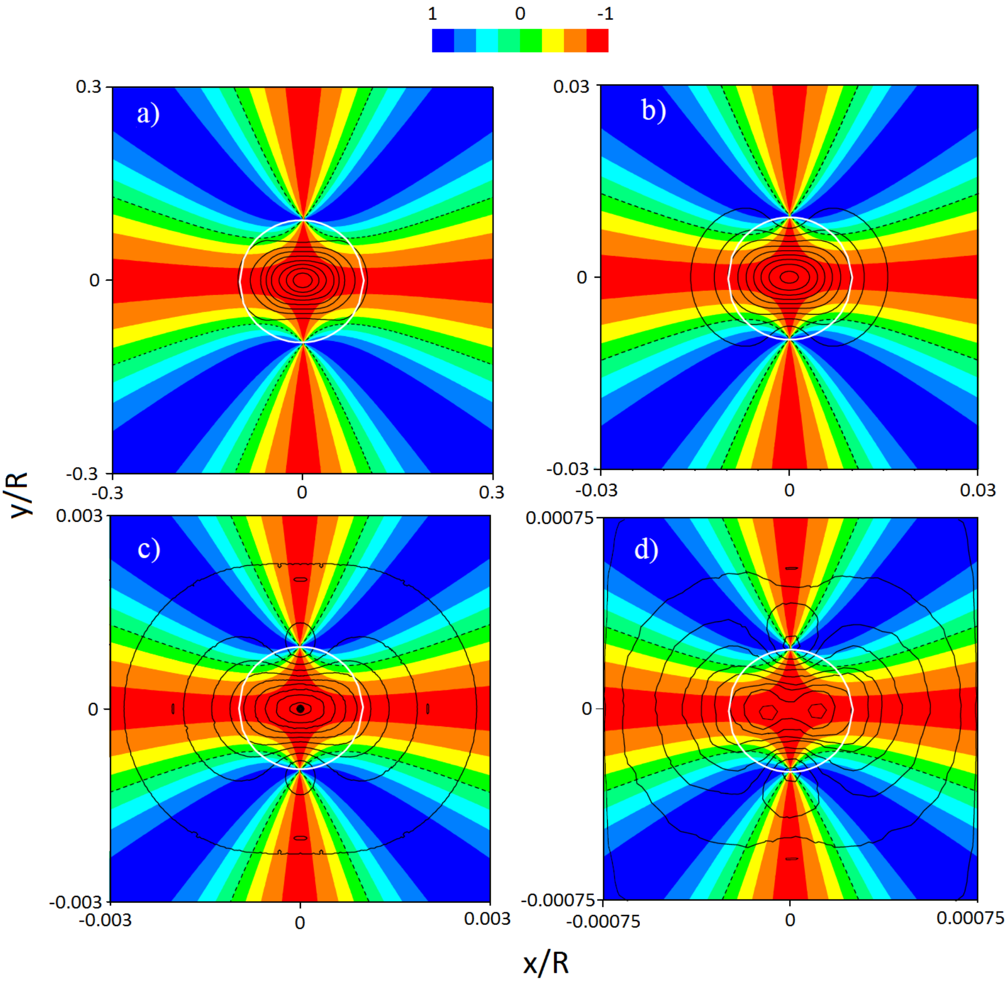

Figure 2.14: Stokes parameter S_3 and level lines of radiation intensity in the plane $(x/R,\, y/R)$ (R being the distance between the source and the observation plane), a) $E_e = 5.3$ MeV, b) $E_e = 53$ MeV c) $E_e = 530$ MeV d) $E_e = 2000$ MeV . Classical treatment. In white, the circle $1/\gamma_i$. The dashed curves are the solution of equation 2.39.

showing the typical structure of a double cross. The central part of the pulse, within the $1/\gamma_i$ circle, has almost the same polarization of the laser beam. At the border and outside this circle, the polarization changes, forming optical vortexes. Along the diagonals, polarization along x is dominant. Fig. 2.14 represents the Stokes parameter for linear polarization as given by a classical Thomson code [65] on a screen, with electron beams with energies of $5\,MeV$, $53\,MeV$, $530\,MeV$ and $2\,GeV$. The portion of the screen shown in the figures scales as $1/\gamma_i$. With increasing γ_i, the polarization presents an almost complete similarity. Instead, the intensity, with increasing γ_i, develops a more pronounced dipolar structure and higher wings.

For a circular polarization, the Stokes parameter:

$$S_2 = \frac{|E_r|^2 - |E_l|^2}{|E_r|^2 + |E_l|^2} \tag{2.42}$$

with E_r and E_l clockwise and counterclockwise components of the electric field, vanishes on the circle $\theta = 1/\gamma_i$ and the profiles along $\xi = x, y$ are given by:

$$|E_r|^2 = \frac{2eE_L^2}{m^2c^4\gamma_i^2(1-\beta_z\frac{z}{R})^6}\frac{\xi^4}{R^6}. \tag{2.43}$$

In the linear approximation, the radiation intensity (2.36), (2.37) and (2.43) are proportional to the laser intensity $|E_L|^2$, while the Stokes parameters (2.38) and (2.42) turn out to be independent of it.

CHAPTER 3

Inverse Compton scattering of beams

The features of the emitted γ beam are determined by the characteristics of the incoming beams, therefore accurate simulations of the electron beam and laser pulse interaction are needed in order to obtain reliable predictions. The particle-particle scattering has to be applied to all the elements constituting the primary beams with the aim of describing the beam-beam interaction. After some general considerations about the beam-beam scattering and some scaling laws, we introduce the code CAIN, which is the main code used for our simulations. A simulation performed with ideal beams is reported and discussed.

3.1 Beam-beam scattering

An electron beam and a laser pulse with distributions $f_e(\underline{r}, \underline{p}, t)$ and $f_L(\underline{r}, \underline{k}, t)$ respectively, are moving in opposite directions in the laboratory. The number of emitted photons per unit time dt and phase space volume $d\underline{p}\, d\underline{k}\, dV$ generated in the interaction is defined as

$$dN(\underline{r}, \underline{p}, \underline{k}) = \sigma_{tot}(\underline{p}, \underline{k}) c(1 - \underline{\beta}_i \cdot \underline{e}_k) N_e f_e(\underline{r}, \underline{p}, t) N_L f_L(\underline{r}, \underline{k}, t) d\underline{p}\, d\underline{k}\, dV\, dt \qquad (3.1)$$

where σ_{tot} is the total Compton cross section (2.14) which depends only on the momenta of the incoming electron and photon, N_e and N_L are the total number electrons and photons and $c(1 - \underline{\beta}_i \cdot \underline{e}_k)$ is the relative velocity of the two beams. The total number of scattered photons can be obtained by integrating eq. (3.1) on time, volume and momenta.

In the simplest case of an head-on collision occurring at waists of both beams, the number of photons per shot can be approximated by

$$N = \mathcal{L}_s \sigma_{tot} \simeq \frac{N_e N_L \sigma_{tot}}{2\pi \Sigma_i} \qquad (3.2)$$

where

$$\Sigma_i = \sqrt{\sigma_x^2 + \frac{w_0^2}{4}} \sqrt{\sigma_y^2 + \frac{w_0^2}{4}}, \qquad (3.3)$$

$\mathcal{L}_s$ is the single collision luminosity, σ_x and σ_y are the transverse rms sizes of the electron beam and w_0 the laser focal spot size. Equation (3.2) is valid whenever we can neglect the diffraction of both the electron beam and the laser beam across the interaction (focal) plane.
This formula shows in first approximation the main ingredients needed to maximize the number of γ scattered photons: a high density of both electron and laser beams is necessary to compensate the low value of the Compton cross section which is of the order of one barn; it is also essential a precise space overlap and synchronization of the beams, correctly focalized at the interaction point.

In terms of operative quantities eq. (3.2) can be calculated as

$$N \simeq 4.12 \cdot 10^8 \frac{E_L[J]Q[pC]}{h\nu_0[eV]\Sigma_i[\mu m^2]} \tag{3.4}$$

with E_L laser pulse energy, Q electron bunch charge, $h\nu_0$ laser photon energy and Σ_i as in eq. (3.3).

Since N represents the total number of scattered photons per shot over the entire solid angle and the entire energy spectrum (from the minimum energy up to the maximum one, at the Compton edge), we should instead consider the beam of photons which is emitted within a small solid angle. It is in fact by selecting the part of the beam close to the emission axis (where the most energetic photons are emitted) that we create a high energy and quasi-monochromatic γ beam. The monochromaticity is measured in terms of relative bandwidth $\Delta\nu_p/\nu_p$, defined as the ratio between the rms and the mean frequency values. From the computational point of view, the bandwidth is calculated on the photons emitted inside a cone defined by a maximum angle θ_{max} around the mean direction of the electrons (usually the z axis).

The value of the bandwidth can be expressed in terms of the laser and the electron beam parameters as shown by the following formula [1]:

$$\frac{\Delta\nu_p}{\nu_p} \simeq \sqrt{\left(\frac{\Psi^2}{\sqrt{12}} + 2\frac{\epsilon_n^2}{\sigma_x^2}\right)^2 + 4\left(\frac{\Delta\gamma}{\gamma}\right)^2 + \left(\frac{\Delta\nu_0}{\nu_0}\right)^2 + \left(\frac{M^2\lambda_0}{2\pi w_0}\right)^4 + \left(\frac{a_0^2/3}{1+a_0^2/2}\right)^2}. \tag{3.5}$$

$\Psi = \gamma\theta_{max}$ is the acceptance angle, σ_x and ϵ_n are the rms spot size at interaction point and the normalized projected emittance of the electron beam (the electron beam is supposed symmetric for simplicity) and $\Delta\gamma/\gamma$ is the electron beam energy spread. $\Delta\nu_0/\nu_0$ is the laser bandwidth, M^2 the laser quality factor, λ_0 the laser wavelength, w_0 the laser focal spot size and $a_0 = 4.3(\lambda_0\sqrt{E_L/\sigma_{z_L}})/w_0$ (dimensionless amplitude of the vector potential associated to the laser e.m. wave) with E_L the energy of the laser and σ_{z_L} the rms laser pulse length. This formula has been obtained by both analytical calculations

---

[1] This is the updated version of the bandwidth value estimation formula reported in Ref. [59].

and simulations on various kind of beams. The different contributions to the bandwidth increase are summed quadratically. In particular, the link between the bandwidth and the emittance of the electron beam is difficult to define, since the emittance and the acceptance angle are correlated in the contribution to the bandwidth spread. Formula (3.5) holds in small θ angle approximation and it shows a very good agreement with the simulations in the ELI-NP-GBS range of parameters (some examples are reported in the next chapter). The last term represents the non-linear effects due to the laser intensity: when the laser parameter a_0 is not much smaller than 1, multi-photon absorption starts being effective and the radiation spectrum is significantly modified in shape and frequency distribution [71]. Narrow bandwidth ICS, as those for Nuclear Physics and Photonics, must minimize these non-linear effects by using laser pulses characterized by small value of a_0. In case of ELI-NP-GBS we have, at maximum, $a_0 = 0.04$.

3.2 Simulation Codes

The simulations for the ELI-NP Gamma Beam System are mainly performed by means of the Monte Carlo code CAIN [62].
The CAIN results have been also compared to ones given by the classical nonlinear code TSST [65] and by a semi-analytical quantum code (see [59] for a detailed dissertation).
In the following we present the structure of the code CAIN and an example of simulation performed using ideal electron beams.
We have also developed a Monte Carlo event-generator code (Compton Monte Carlo Code - CMCC): a brief description and comparison with CAIN results is reported in Appendix B.

3.2.1 CAIN code

CAIN is a well known and benchmarked [38] Monte Carlo code developed by K. Yokoya [61]. For the particle-particle scattering it follows the QED Landau-Lifshitz approach that we resumed in the previous chapter. The extension to real beams interaction is based on the Monte Carlo probabilistic method. This code takes into account all the linear Compton scattering features comprise the scattering angle α, the multiple scattering and the emitted photons polarization.

The electron beam can be generated by the code according to the parameters given in the input file, or it can be inserted from the user by an external file. We usually apply the latter option. The laser beam has a Gaussian distribution defined by the parameters given in the input file and it is supposed to be transform limited. The laser beam is defined in its own coordinate systems $(x_L,\, y_L,\, z_L)$ as shown in Fig. 3.1.

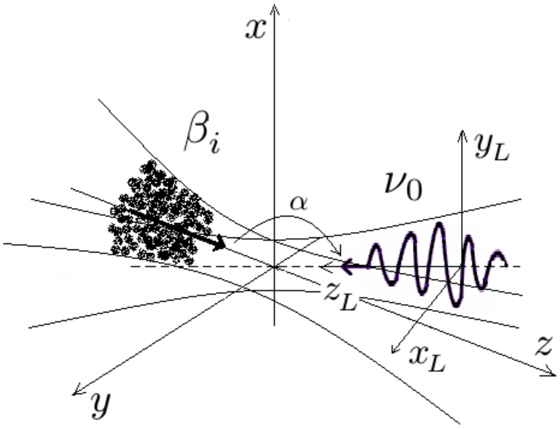

Figure 3.1: Beam-beam scattering geometry. The beams interact at their waists. α is the collision angle between the directions of the two beams. The laser proper coordinate system is (x_L, y_L, z_L).

The particles inside the two beams are clustered into macroparticles during the simulation. Each macroparticle is constituted by a certain number of real particles (the total number of particles in the beam divided by the number of macroparticles used in the simulation) with the same position, momentum and energy values. Also the emitted photons are expressed in terms of macroparticles: the number of real photons is calculated only at the end of the process using the so called "weight" of the macrophotons.

Let us briefly describe the algorithm.

- The simulation starts at $t = 0$ and it is divided in time steps. Each macroelectron is tracked separately.
- The tracking of the i-th macroparticle starts: the position of the macroparticle and the local vector of the laser are calculated.
- The Compton scattering event is sampled with a rejection method which compares a random number $r_1 \in (0, 1)$ with the normalized to 1 value of $\sigma_{tot}(\underline{p}, \underline{k})$, which is the total Compton cross section (2.14). $\sigma_{tot}(\underline{p}, \underline{k})$ depends only on the momenta of the incoming electron and photon and is proportional to the probability of a photon being emitted. Only the Lorentz transformation (2.16) of the laser frequency to the ERF is needed at this step. If $r_1 \geq \sigma_{tot}$ the event is rejected and the code moves to the next macroparticle, otherwise a photon is generated.
- If a photon is generated, the code moves to the macroelectron's rest frame ERF. Here the differential cross section (2.27) integrated over the azimuthal angle ϕ is

used to sample the emitted photon energy. A random value e of the photon energy is generated and plugged in $d\sigma/dY$. Another random number $r_2 \in (0,1)$ is generated. If $r_2 \geq d\sigma(e)/dY$, the energy value is rejected and the energy sample repeated, otherwise the emitted photon energy is decided.

- The azimuthal angle is sampled by using the differential cross section (2.27).
- The polarization of the emitted photon, as described in Section 2.3.1, and the features of the scattered electron are calculated.
- The code by Lorentz transforming all the involved quantities moves back to LAB frame and the next macroparticle is considered.
- When all the macroparticles are considered, the code moves to the next time step.

Any further information is contained in the CAIN manual [62].

Remark. *The CAIN version we use is the Unix one. The Windows version contains a bug: the transverse momenta of the emitted photons are slightly underestimated. This doesn't affect the total number of photons, but creates problems in the bandwidth computation.*

3.2.2 Example of simulation with ideal beams

An ideal electron beam has been built by adding one by one the typical characteristics of its phase space distribution: by means of the following simulations the link between the electron beam features and the emitted photon beam is shown. We will see how the spectrum, the bandwidth and the number of photons change while the electron beam changes. At first we consider a completely monochromatic beam, beam A: in this case the interaction can be seen as a single electron-laser interaction. In beams B and C we add the transverse dimensions σ_x, σ_y (supposing $\sigma_x = \sigma_y$) and the energy spread. Beam D is obtained by removing σ_x, σ_y and by adding the transverse momenta ($p_x = p_y$). The final beam (E) is comprehensive of all the mentioned features.

Table 3.1 reports the varying parameters of the five sample electrons beams. The common values are the charge of 250 pC and the length of the beams, $\sigma_z = 280$ μm. The electrons collide with a 515 nm wavelength laser with $w_0 = 28$ μm, energy 0.4 J, length 1.5 ps and linear polarization along the y axis (horizontal direction). The collimation angle θ_{max} is fixed at 160 μrad, while the collision angle is $\alpha = \pi$ (head-on collision).

The electron beam E features are presented in details in Fig. 3.2: transverse distribution in x, transverse momentum distribution p_x and the graph of x vs p_x. In the bottom line the longitudinal space and momentum distributions are reported.

The total number of photons obtained by the collision of beam A is $N = 8.6 \cdot 10^7$ and as we can see in graph a) of Fig. 3.3 the spectrum is very broad, ranging between 4 eV

Table 3.1: Ideal beam features used in the simulations.

Beam	σ_x [μm]	$\Delta\gamma/\gamma$	σ_{p_x} [keV/c]	ϵ_n [mm·mrad]
A	0	0	0	0
B	18	0	0	0
C	18	$8.25 \cdot 10^{-4}$	0	0
D	0	$8.25 \cdot 10^{-4}$	15	0
E	18	$8.25 \cdot 10^{-4}$	15	0.53

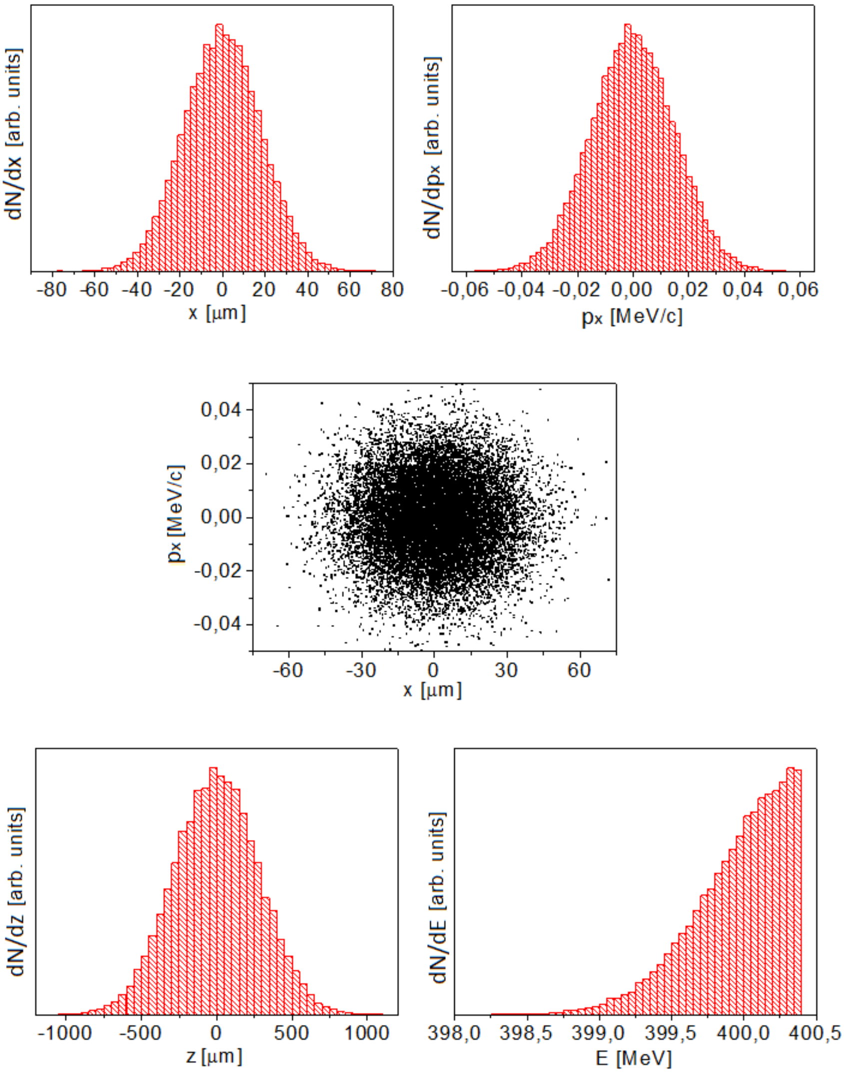

Figure 3.2: Ideal electron beam E features: p_x [MeV/c] as a function of x [μm] x [μm] and distributions of x [μm], p_x [MeV/c], z [μm], E_e [MeV].

and 5.81 MeV. The thin and highly monochromatic part of the beam selected by the collimation angle is presented in terms of spectrum in graph b) and in red in the transverse plane in window c).

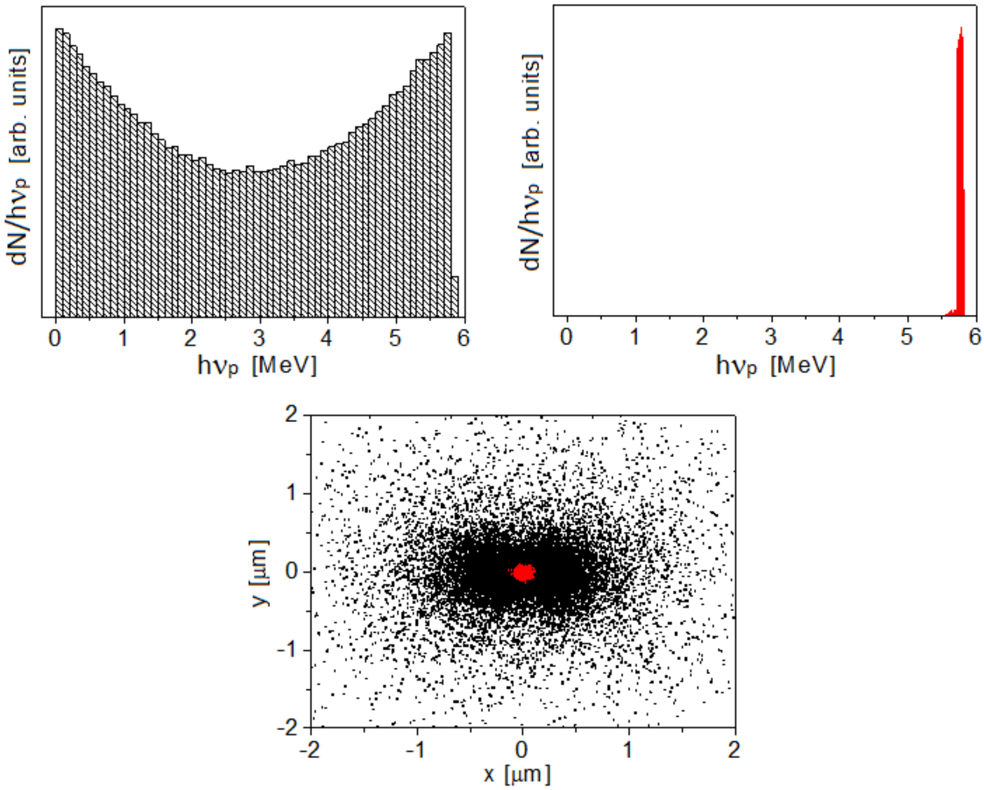

Figure 3.3: Result of the beam A simulation: emitted photons spectrum dN/dhν_p [arb. units] as a function of energy hν_p [MeV] and transverse distribution at the IP [μm]. Total beam in black, collimated beam in red.

We are interested in the value of bandwidth and in the number of corresponding photons N^{bw}: the results of the simulations are reported in Table 3.2. Since CAIN takes into account the possibility that an electron undergoes more than one collision by passing through the laser beam (multiple scattering), we distinguish between the first generation emitted photons and the next generations (in this case up to the third). The second and third generations emitted photons contribute to the presence of lower energy photons within the collimation angle: they create a long tail (see Fig. 3.4) in the collimated spectrum which affects the calculation of the rms bandwidth. Table 3.2 shows that this effect is important for the more ideal beams, while tends to vanish in cases D and E. In Fig. 3.5 the particles which constitute the tails in the collimated spectra (especially for beams A, B, C) are clearly visible.

Table 3.2: Results of the simulations performed using the electron beams described in Table 3.1. The values of bandwidth and corresponding number of photons are reported considering all the photons (columns 2-3) and only the first generation photons (columns 4-5).

	All photons		I gen photons only	
Beam	$\Delta\nu_p/\nu_p$ [‰]	N^{bw}	$\Delta\nu_p/\nu_p$ [‰]	N^{bw}
A	5.19	$1.94 \cdot 10^6$	4.43	$1.89 \cdot 10^6$
B	4.91	$7.39 \cdot 10^5$	4.43	$7.27 \cdot 10^5$
C	5.17	$7.39 \cdot 10^5$	4.70	$7.27 \cdot 10^5$
D	7.46	$1.93 \cdot 10^6$	6.90	$1.88 \cdot 10^6$
E	7.26	$7.28 \cdot 10^5$	6.90	$7.16 \cdot 10^5$

Beams A and B exhibit the same collimated spectra shape (Fig. 3.4) and a very similar value of bandwidth, but N^{bw} in case B is much lower. This is due to the fact that in case B the electrons do not interact any more with the most intense part of the laser only (the laser transverse distribution is also a Gaussian).

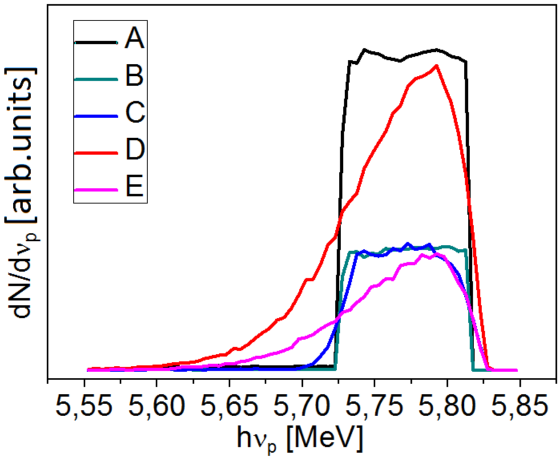

Figure 3.4: Spectrum of the emitted photons dN/dhν_p [arb. units] in the collimation angle as a function of energy hν_p [MeV] obtained by the interaction of the electron beams reported in Table 3.1. The spectra colors are related to the electron beam as follows: A black, B dark cyan, C blue, D red, E magenta.

In case C we notice a slight bandwidth enlargement: even though the electrons are still moving parallel to the z axis, the energy spread causes a degradation of the spectrum. N^{bw} is not affected.

By removing the transverse distribution as in case D, the N^{bw} returns to case A value (only the central part of the laser is involved). On the other hand, the transverse momenta, even if their value is contained, cause a strong enlargement of the bandwidth. The final beam E couples the bandwidth and N^{bw} degradation, while the shape of the spectrum is the same as case D.

This simulation is just an example: the correlations between the various parameters are very complicated, especially when dealing with realistic beams. It is therefore necessary to simulate each interaction in order to obtain reliable previsions on the emitted photons features.

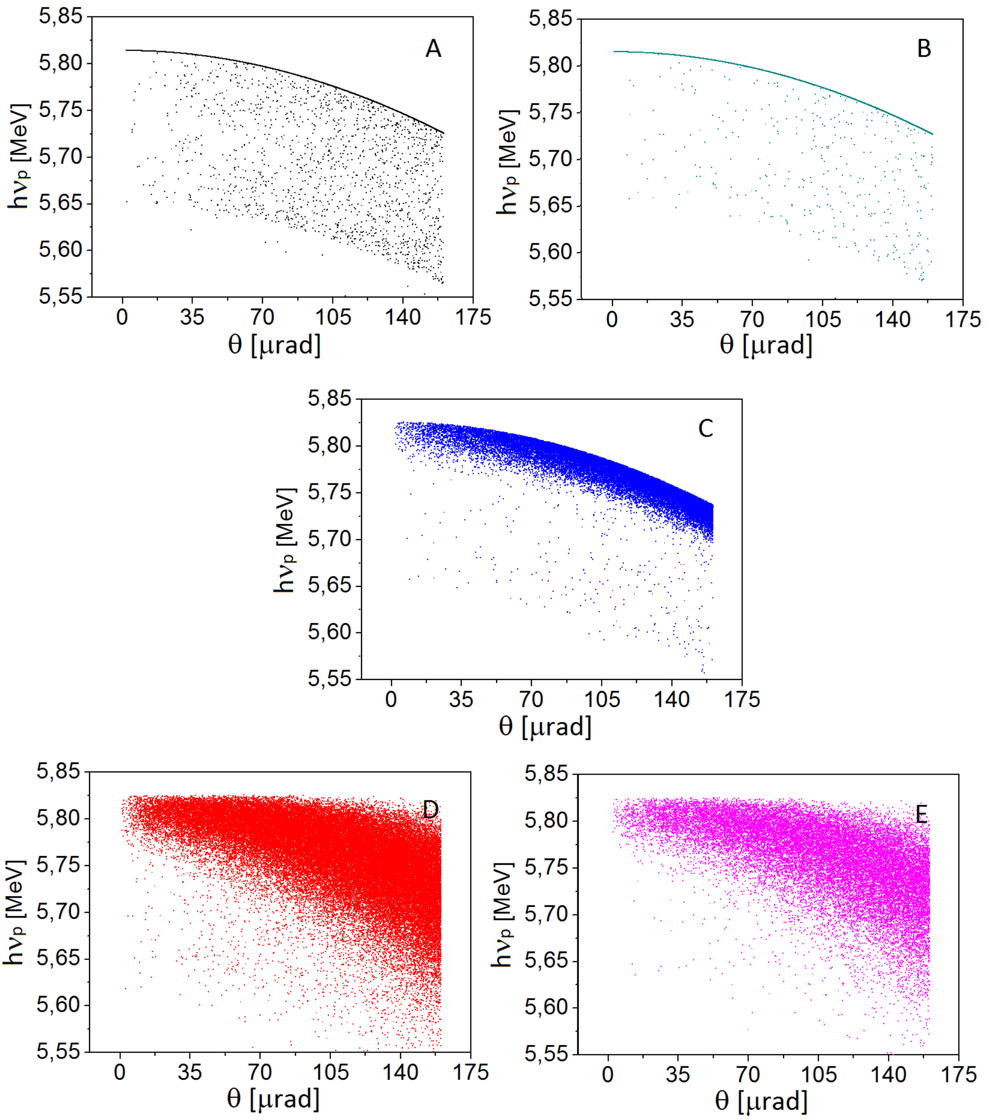

Figure 3.5: Energy of the emitted photons hν_p [MeV] in the collimation angle as a function of θ [μrad] for the five electron beams simulations.

CHAPTER 4

ELI-NP γ beam simulations

The general electron and laser beams parameters of the ELI-NP Gamma Beam System are reported in the introductive Table 1.1. Our simulations are performed on several working points. The electron beams we insert in CAIN are generated and tracked by means of the codes ASTRA, TStep and elegant [72–75] from the cathode to the interaction point [48], while the laser beam is generated by CAIN itself. In the following, an example of full simulation of the 3.5 MeV γ beam is reported. The chapter continues with a dissertation about the emitted photon beam polarization for 6 main working points (the electron and laser beam energies are reported in Table 4.4), which correspond to the emitted photons energies of 1, 2, 3.5 MeV for the low energy line and 10, 13, 19.5 MeV for the high energy line. The analysis of the possible misalignments and jitters of both the electron beam and the laser conclude the chapter.

4.1 Example of full simulation

The data of the incoming beams are collected in Tables 4.1 and 4.2.

Table 4.1: Incoming electron beam parameters.

Electron beam parameters	
Mean energy [MeV]	311.65
Bunch charge [pC]	250
Bunch length [μm] rms	278.74
Transvese emittance x,y [mm·mrad]	0.50, 0.48
Relative energy spread [%]	$7.25 \cdot 10^{-2}$
Focal spot size x,y [μm] rms	19.62, 19.65

The electron beam features are presented in Fig. 4.1: graph a) shows a simil-Gaussian space distribution in both x and y coordinates. The x and y distributions are symmetric and centered in 0, on the opposite there is no symmetry in the longitudinal coordinate (graph c)). The transverse momenta present symmetric distributions (graph b)) and the transverse phase space distributions are reported in graphs d) and e). The p_z distribution and p_z as a function of z are given in graphs f) and g).

Table 4.2: Laser parameters.

Laser parameters	
Laser pulse energy [J]	0.2
Laser wavelength [nm]	515
Laser photon energy [eV]	2.4
Laser pulse length [ps] rms	1.5
Laser focal spot size w_0 [μm]	28
Laser parameter a_0	0.02
Laser polarization	$(0,\ 0,\ -1)$
Collision angle α [^{o}]	172
Laser repetition rate [Hz]	100
Laser recirculator round trips	32

This working point at 311 MeV belongs to the low energy line, therefore the laser energy is 0.2 J. The collision angle $\alpha = \pi - 8^o$ in our geometry is placed in the $x - z$ plane as shown in Fig. 4.2. Even though the collision angle is very small, the difference with the head-on collision is not negligible especially in terms of the emitted photons number. The comparison between the $\alpha = 172^o$ and the $\alpha = \pi$ cases is reported in Table 4.3. The laser is linearly polarized along the y axis: in terms of the Stokes parameters, $S = (0, 0, -1)$.

In Table 4.3 the emitted photons characteristics are reported for both the real collision angle $\alpha = 172^o$ and the ideal head-on collision ($\alpha = 180^o$).

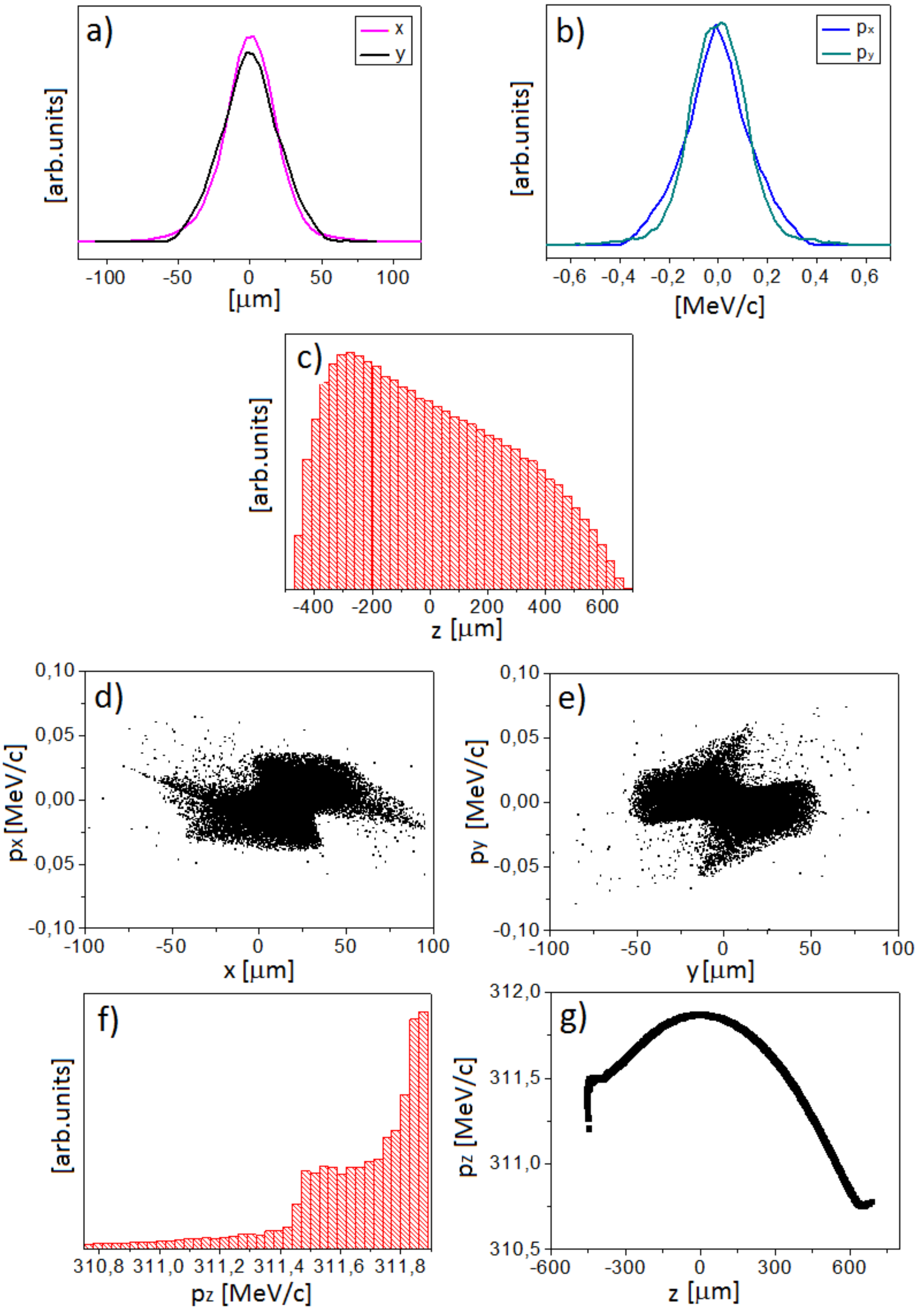

Figure 4.1: Incoming electron beam features: distributions of x [μm], y [μm], z [μm], p_x [MeV/c], p_y [MeV/c], p_z [MeV/c]. p_x [MeV/c] as a function of x [μm], p_y [MeV/c] as a function of y [μm] and p_z [MeV/c] as a function of z [μm].

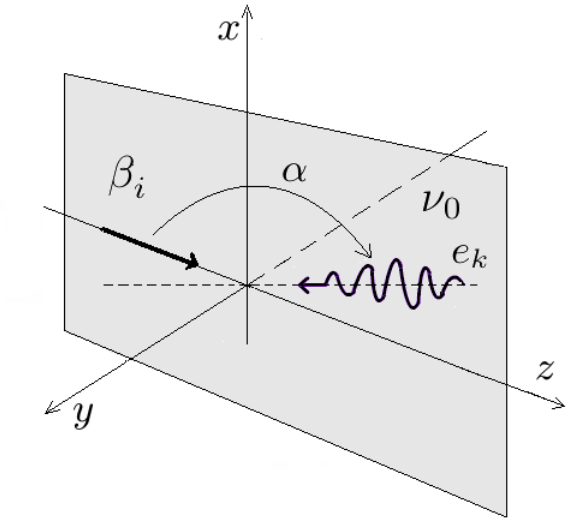

Figure 4.2: Interaction geometry: the incoming electron beam propagates along the z axis. The laser direction forms an angle α with the electrons direction in the $x-z$ plane.

Table 4.3: Emitted photons resulting from the collision of the electron and the laser beams described respectively in Table 4.1 and 4.2: parameters in the two cases of $\alpha = 172^o$ and $\alpha = 180^o$.

Emitted γ Photons parameters		
	$\alpha = 172^o$	$\alpha = 180^o$
Mean energy [MeV] ($\langle h\nu_p \rangle$)	3.50	3.52
Peak energy [MeV] ($h\nu_p^{peak}$)	3.51	3.53
Collimation angle [μrad] (θ_{max})	165	165
Bandwidth [keV] rms ($\Delta\nu_p$)	17.68	18.12
Relative bandwidth [‰] rms ($\Delta\nu_p/\langle\nu_p\rangle$)	5.04	5.15
Number photons per shot (N)	$7.86 \cdot 10^6$	$1.41 \cdot 10^7$
Number photons per shot in collimation angle (N^{bw})	$1.15 \cdot 10^5$	$2.07 \cdot 10^5$
Number photons per shot within rms ($\tilde{N}$)	$4.95 \cdot 10^4$	$8.68 \cdot 10^4$
Spectral density [ph/s·eV] (SD)	$8.96 \cdot 10^3$	$1.53 \cdot 10^4$
Source size x, y [μm] rms (σ_x^γ, σ_y^γ)	18.42, 11.62	11.50, 12.17
Source divergence x,y [μrad] rms ($\sigma_{x'}^\gamma$, $\sigma_{y'}^\gamma$)	73.24, 73.10	70.35, 70.49
Source divergence [μrad] rms (Div)	39.11	39.12
Radiation pulse length [ps] rms (σ_t^γ)	0.82	0.83
Peak brilliance [ph/s·mm^2·mrad^2·0.1%] (B^{peak})	$1.05 \cdot 10^{20}$	$3.17 \cdot 10^{20}$
Average brilliance [ph/s·mm^2·mrad^2·0.1%] (B^{ave})	$6.93 \cdot 10^{11}$	$1.97 \cdot 10^{12}$
Spot size at 10 meters x,y [mm] rms	0.83, 0.82	0.83, 0.82

Legend of Table 4.3:

- Source divergence:

$$Div = \theta_{rms} = \sqrt{\langle \theta^2 \rangle - \langle \theta \rangle^2} \qquad \text{where} \qquad \theta = \arctan\left(\frac{\sqrt{k_x^2 + k_y^2}}{k_z}\right) \tag{4.1}$$

  is calculated on the collimated beam, i.e. by taking into account the photons with $0 < \theta < \theta_{max}$ being θ_{max} the collimation angle.

- Spectral density:

$$SD = \frac{\tilde{N} \cdot r}{\Delta\nu_p} \qquad \text{where} \qquad \tilde{N} = \int_{\nu_p^{peak} - \frac{\Delta\nu_p}{2}}^{\nu_p^{peak} + \frac{\Delta\nu_p}{2}} \frac{dN}{d\nu_p}(\nu'_p)\, d\nu'_p. \tag{4.2}$$

  $dN/d\nu_p$ is the spectrum of the collimated beam, $\Delta\nu_p$ is the rms value of the collimated photons frequency, r is the number of shots per second (product of the laser repetition rate 100 Hz and the recirculator rate 32).

- Peak brilliance:

$$B^{peak} = \frac{\tilde{N}}{(2\pi)^{\frac{5}{2}} \sigma_x^\gamma \sigma_y^\gamma \sigma_{x'}^\gamma \sigma_{y'}^\gamma \sigma_t^\gamma \frac{\Delta\nu_p}{\langle \nu_p \rangle}} \tag{4.3}$$

  with $\tilde{N}$ as above, $\Delta\nu_p/\langle\nu_p\rangle$ the rms relative bandwidth in units of $[0.1\%]$ calculated on the photons in the collimation angle.
  $\sigma_\cdot^\gamma$ are the x, y, x', y' and t rms values of the emitted γ photons with frequency in the range $[-\Delta\nu_p/2, +\Delta\nu_p/2]$ around the frequency peak value.

- Average brilliance:

$$B^{ave} = \frac{\tilde{N} \cdot r}{4\pi^2 \sigma_x^\gamma \sigma_y^\gamma \sigma_{x'}^\gamma \sigma_{y'}^\gamma \frac{\Delta\nu_p}{\langle \nu_p \rangle}} \tag{4.4}$$

  represents the average brilliance calculated on one second.

The collimation angle $\theta_{max} = 165$ μrad has been chosen in order to have a relative bandwidth value of 0.005 as shown in window a) of Fig. 4.3. In the graph the simulated bandwidth value (magenta) is compared to the values calculated by means of formula (3.5): the results are in perfect agreement. The number of photons in the collimation angle as a function of the angle is reported in window b) of Fig. 4.3.

The spectrum of the $7.86 \cdot 10^6$ emitted photons is reported in graph a) of Fig. 4.4: the typical Compton shape extends from 7.7 eV to 3.53 MeV. The photons in the collimation angle $\theta_{max} = 165$ μrad are highly monochromatic, the spectrum is reported in graphs b) and c). The multiple scattering has been considered in the simulation: the collimated spectrum of graphs b) and c) is comprehensive of the emitted photons up to the fourth generation (the highest reached in this specific case). Window d) shows that the more

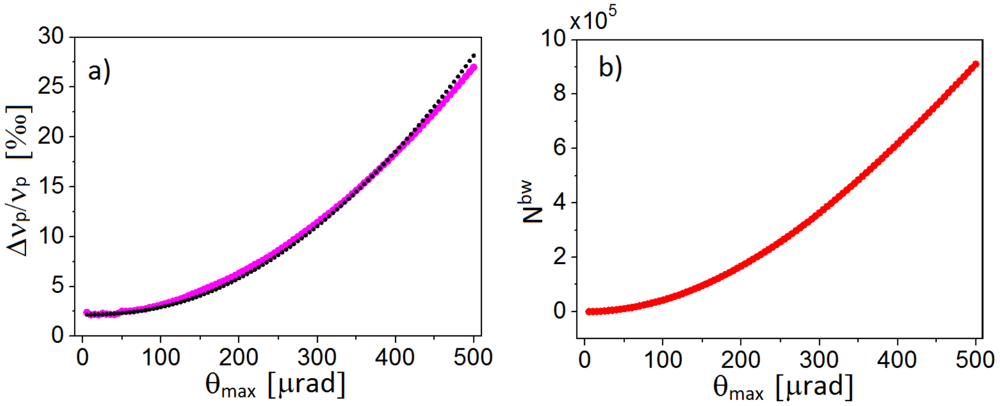

Figure 4.3: Window a): simulated relative bandwidth (magenta) and expected relative bandwidth value from formula (3.5) (black) as a function of the collimation angle θ_{max} [μrad]. Window b): simulated number of photons in the collimation angle as a function of the collimation angle θ_{max} [μrad].

energetic photons are concentrated within a tiny angle around the z axis. In the last window the energy of the collimated beam is presented as a function θ.

Fig. 4.5 represents the transverse features of the gamma beam at the IP. We notice an asymmetry in the x and y coordinates due mainly to the collision angle which is in the $x-z$ plane. The transverse momenta distribution plotted in graph b) is determined by the laser pulse linear polarization in the y direction. This transverse momenta distribution leads to the oblong shape of the γ beam transverse distribution shown in Fig. 2.11. From the values reported in Table 4.3, we notice that the rms spot size of the emitted beam is smaller compared to the incoming beam spot sizes (the effect is even more evident in the $\alpha = 180^o$ case): assuming an ideal Gaussian shape for both electron and laser beams, the emitted beam spot size is given by the product of the two Gaussian distributions. If we consider for example the x component, the spot size of the emitted beams is

$$\sigma_x^{out} \simeq \sqrt{\frac{\sigma_{x_e}^2 \sigma_{x_L}^2}{\sigma_{x_e}^2 + \sigma_{x_L}^2}}, \tag{4.5}$$

which in our simulation gives $\sigma_x^{out} \simeq 11.4\ \mu$m ($\sigma_{x_e} = 19.62\ \mu$m and $\sigma_{x_L} = 14\ \mu$m).

As shown in Fig. 4.6, the linear polarization Stoke parameter mean value $\langle S_3 \rangle$ is very close to -1 on beams collimated within small collimation angles. This means that the most energetic photons (the ones emitted close to the z axis) retain the laser polarization. The emitted full beam has been propagated and snapshots of $\langle S_3 \rangle$ and of the transverse space distribution on a screen perpendicular to the z axis at 0.0001, 0.001, 0.01, 0.1 m from the IP are presented in Fig. 4.7. The typical S_3 double cross shape starts appearing at some distance from the IP.

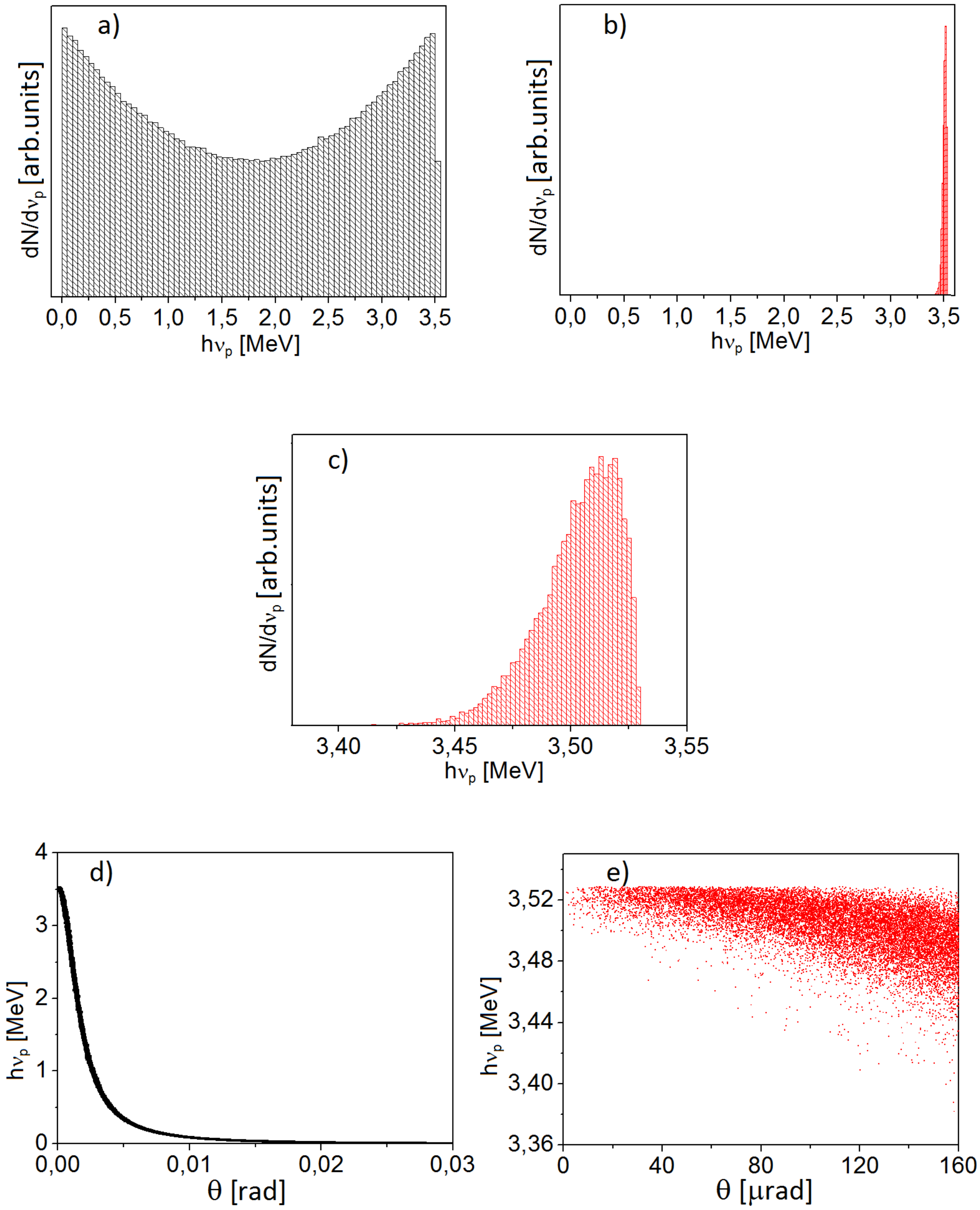

Figure 4.4: Emitted photons characteristics: full beam (black) and beam in the collimation angle $\theta_{max} = 165$ μrad (red). Number of photons as a function of the photon energy $h\nu_p$ [MeV] a), b) and c). Energy of the photons $h\nu_p$ [MeV] as a function of θ [rad] d) and [μrad] e).

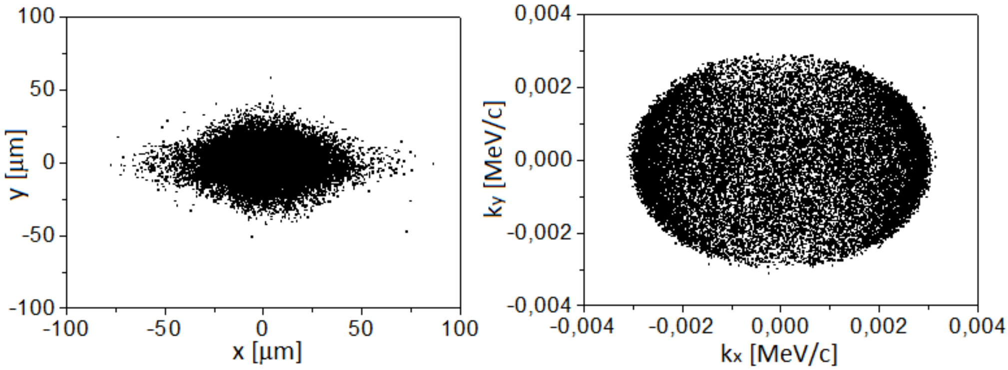

Figure 4.5: Gamma beam: snapshot of the transverse space coordinates x vs y and of the transverse momenta p_x vs p_y at the IP.

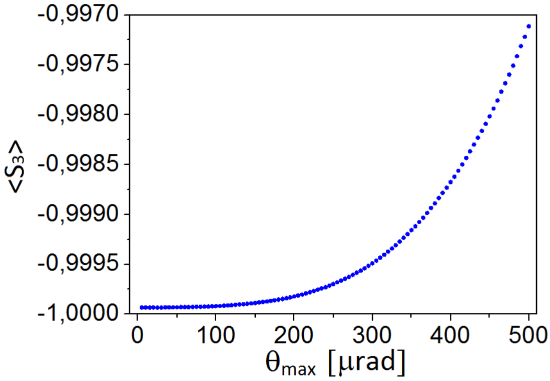

Figure 4.6: $\langle S_3 \rangle$ Stoke parameter mean value calculated on the emitted γ beam as a function of the collimation angle [μrad].

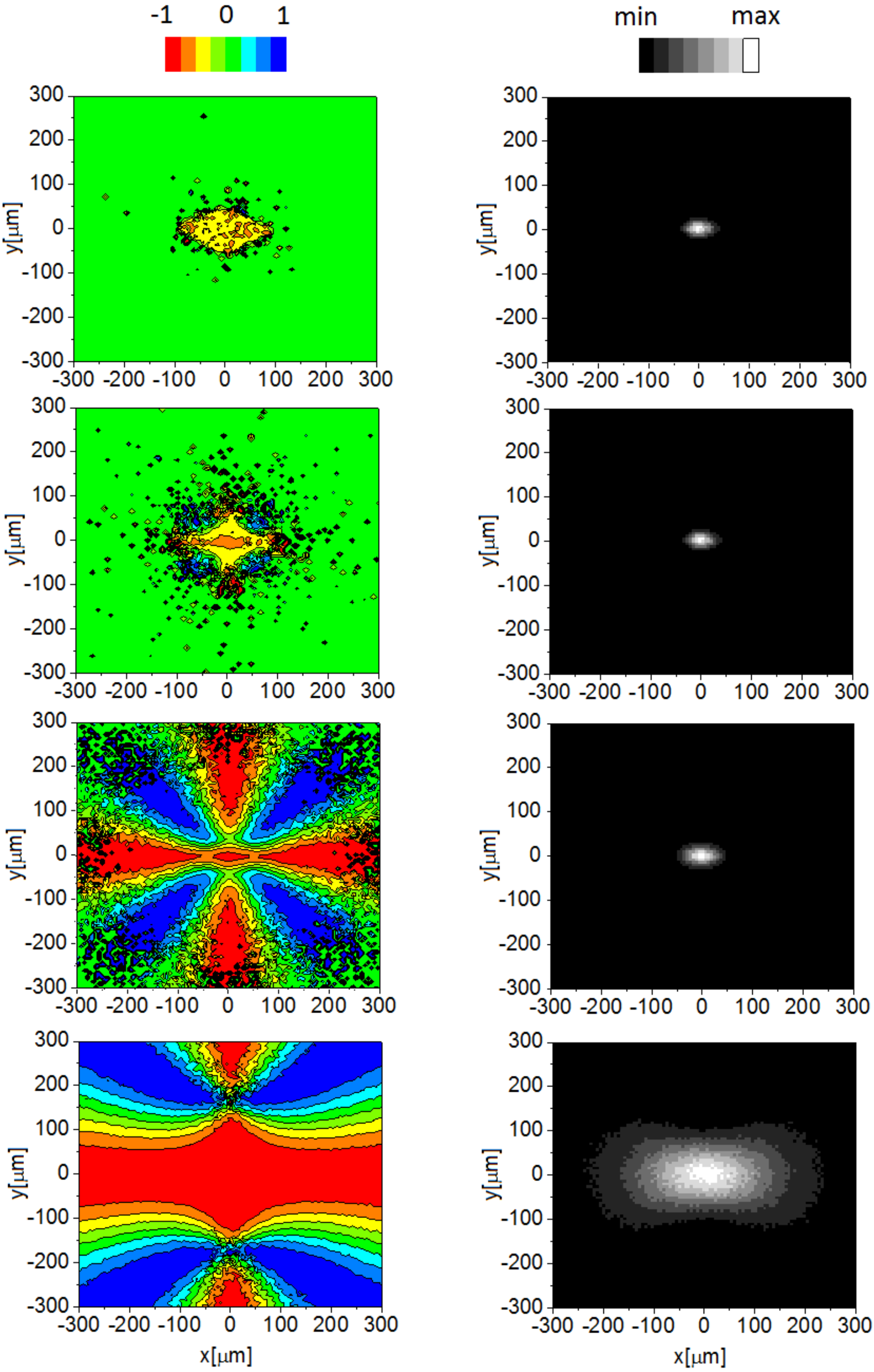

Figure 4.7: Stoke parameter mean value $\langle S_3 \rangle$ (left column) and space distribution (right column) of the emitted photons on a screen perpendicular to the z axis at 0.0001, 0.001, 0.01, 0.1 m from the IP. The x and y coordinates are expressed in μm.

4.2 Polarization of the emitted photons

The characteristics of the emitted photons' polarization of the ELI-NP-GBS 6 main working points above mentioned are discussed in the following. The reference electron beams and the nominal laser parameters and interaction conditions have been used. In particular, in our calculations, the laser is considered 100% polarized. Since, however, the expected laser polarization at ELI-NP-GBS is higher than 98% [46], the effective polarization figures reported in graphs and tables should be normalized by a factor 0.98.

The average values of flux and of the Stokes parameters $\langle|S_2|\rangle$ and $\langle|S_3|\rangle$ for circular and linear laser polarization respectively for the 6 main working points, calculated in the typical ELI-NP-GBS bandwidth value of 0.005 and for a larger acceptance, corresponding to a bandwidth of 0.2 are listed in Table 4.4.

Table 4.4: Average values of flux and of the Stokes parameters $\langle|S_2|\rangle$ and $\langle|S_3|\rangle$ for circular and linear laser polarization respectively for the main working points, in the bandwidth 0.005 and for a larger acceptance, corresponding to a bandwidth of 0.2. Laser energy at $0.2\,J$. In the cases with star, the laser energy is $0.4\,J$.

E_e [MeV]	$h\nu_p$ [MeV]	$\mathrm{N}^{0.005}$ $\times 10^5$	$\langle\lvert S_3\rvert\rangle^{0.005}$	$\langle\lvert S_2\rvert\rangle^{0.005}$	$\mathrm{N}^{0.2}$ $\times 10^6$	$\langle\lvert S_3\rvert\rangle^{0.2}$	$\langle\lvert S_2\rvert\rangle^{0.2}$
165	1	1.48	> 0.999	> 0.999	4	0.85	0.65
234	2	1.35	> 0.999	> 0.999	4	0.85	0.68
311	3.5	1.15	> 0.999	> 0.999	3.9	0.85	0.68
*529	10	2.97	> 0.999	> 0.999	10	0.86	0.72
*605	13	2.67	> 0.999	> 0.999	9.5	0.86	0.71
*750	19.5	2.37	> 0.999	> 0.999	10	0.87	0.7

The polarization degree is connected to the momentum distribution of the photons, so the polarization shape appears with the propagation of the photons (see Fig. 4.7). Fig. 4.8 gives the distribution of the Stokes parameter and of the photon intensity on a screen perpendicular to the z axis at a distance R from the IP, with photons at $10\,MeV$ for linear and circular laser polarization.

Fig. 4.9 gives the photon number, the relative bandwidth and the average values of S_3 and S_2 as a function of the acceptance angle θ_{max} for the working points at 2 MeV and 10 MeV. A synthetic view of both intensity and polarization is shown in Fig. 4.10.

As predicted by the formulas in Chapter 2, the central part of the emitted beam retains the same laser polarization: the results show that, while for the cases at bandwidth 0.005 the degree of linear or circular polarization is always close to 1, the depolarization increases with the bandwidth, reaching 15% at 0.2 in the case of linear polarization and also more than 30% for circular polarization, a situation which appears to be quite critical for users requiring tight control of the polarization of the source.

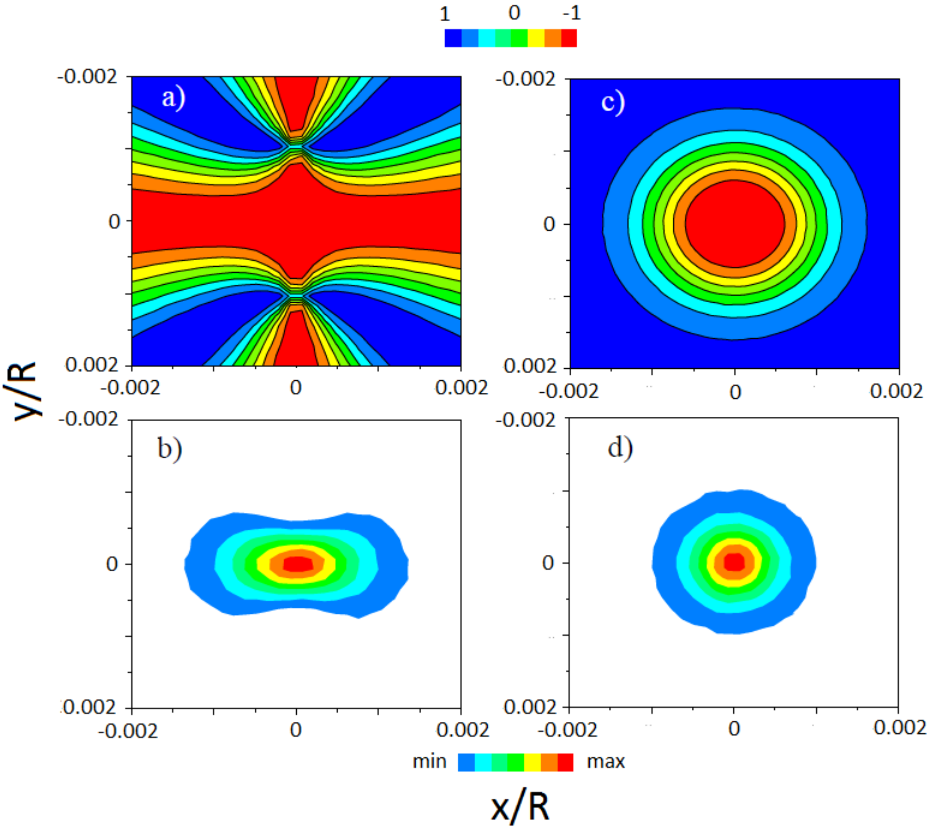

Figure 4.8: Stokes parameter S_3 a) and S_2 c) and photon distribution b) and d) for linear (left) and circular (right) laser polarization along y, with emitted photon energy 10 MeV.

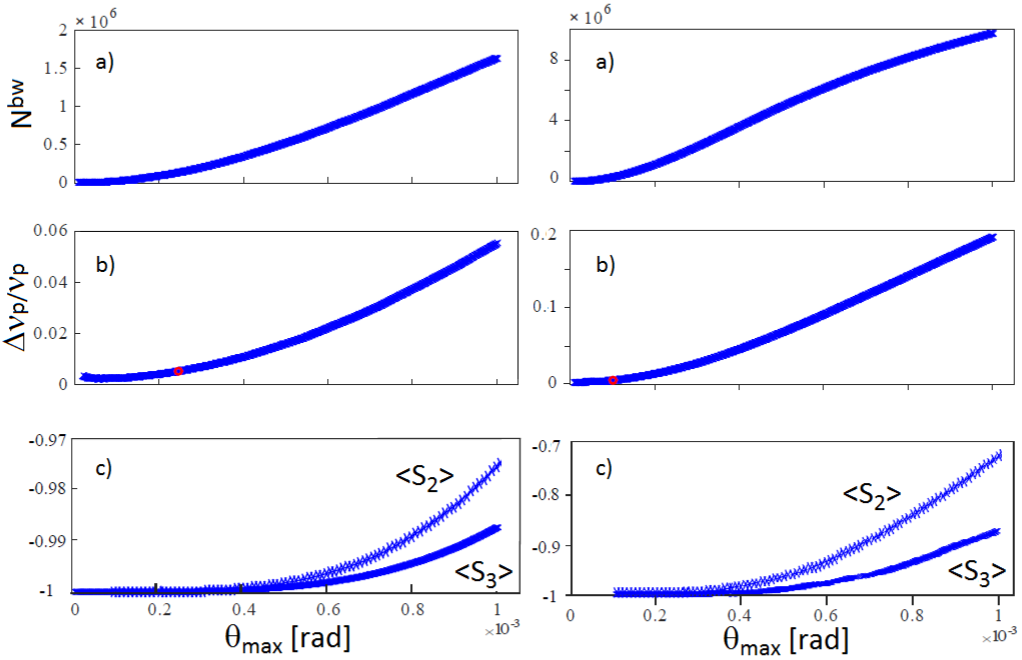

Figure 4.9: N^{bw} number of photons in θ_{max} a), relative bandwidth b) and Stokes parameters $\langle S_2 \rangle$ and $\langle S_3 \rangle$ c) for gamma rays at 2 MeV (left column) and 10 MeV (right column), linear and circular laser polarizations.

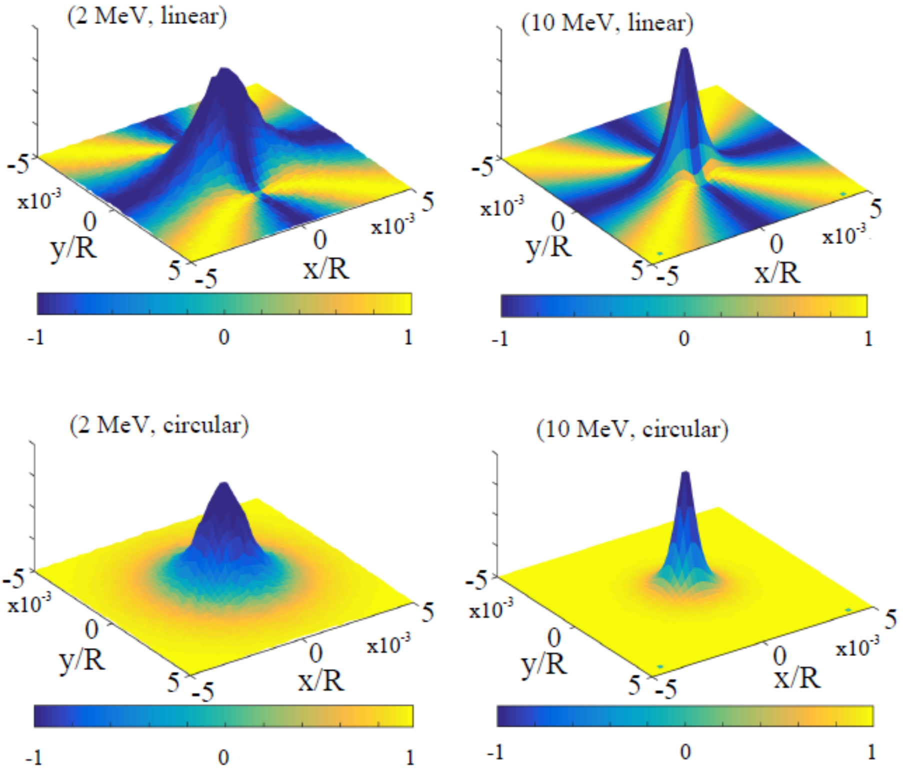

Figure 4.10: Intensity-polarization graphs for photons at 2 and 10 MeV, with linear and circular laser polarization.

4.3 Errors and jitters effects on radiation

In this section, the effects on the emitted photons of errors and jitters of both the electron and the laser beams are discussed together with the possible collimation system displacements.

4.3.1 Spatial misalignments

We start with a general simulation considering a wide range of spatial misalignments at the IP: the electron beam axis coincide with the collimator one and the laser beam is misaligned. The incoming beams features are reported in Table 4.5 and the interaction geometry is shown in Fig. 4.2. The collimation angle θ_{max} has the fixed value of 192 μrad.

Table 4.5: Electron and laser beams parameters.

Electron beam parameters	
Mean energy [MeV]	280.28
Bunch charge [pC]	250
Bunch length [μm] rms	280
Transverse emittance x,y [mm·mrad]	0.46, 0.44
Relative energy spread [%]	$8.43 \cdot 10^{-2}$
Focal spot size x,y [μm] rms	20.22, 18.5
Laser parameters	
Laser pulse energy [J]	0.2
Laser wavelength [nm]	515
Laser pulse length [ps] rms	1.5
Laser focal spot size w_0 [μm]	28
Laser parameter a_0	0.02
Laser polarization	$(0,\ 0,\ -1)$
Collision angle α [^{o}]	172

In the simulations we consider the laser spatial misalignments reported in Table 4.6.

In Figs. 4.11 and 4.13 the simulated total number of photons per shot N values are compared to the values given by the formula [76] for the estimation of N in presence of

Table 4.6: Laser pulse misalignment values Δ_x, Δ_y, Δ_z considered for the three space coordinates (in μm).

Laser misalignment values [μm]								
Δ_x	0	10	20	30	40	60	80	100
Δ_y	0	10	20	30	40	60	80	100
Δ_z	-500	-400	-300	-200	-100	-50	0	
			50	100	200	300	400	500

spatial misalignment:

$$
\begin{aligned}
N \simeq & \frac{N_e N_L \sigma_{tot} A_x A_y A_z}{2\pi\sqrt{\sigma_x^2 + \frac{w_0^2}{4} + (\sigma_{z_e}^2 + \sigma_{z_L}^2)\tan^2(\frac{\alpha_0}{2})}\sqrt{\sigma_y^2 + \frac{w_0^2}{4}}} \\
A_x &= \exp\left(-\frac{\Delta_x^2}{2(\sigma_x^2 + \frac{w_0^2}{4} + (\sigma_{z_e}^2 + \sigma_{z_L}^2)\tan^2(\frac{\alpha_0}{2}))}\right) \\
A_y &= \exp\left(-\frac{\Delta_y^2}{2(\sigma_y^2 + \frac{w_0^2}{4})}\right) \\
A_z &= \exp\left(-\frac{\Delta_z^2\tan^2(\frac{\alpha_0}{2})}{2(\sigma_x^2 + \frac{w_0^2}{4} + (\sigma_{z_e}^2 + \sigma_{z_L}^2)\tan^2(\frac{\alpha_0}{2}))}\right)
\end{aligned}
\tag{4.6}
$$

where Δ_x, Δ_y, Δ_z are the misalignment values in the three coordinates and $\alpha_0 = \pi - \alpha$. The agreement between eq. (4.6) and the simulated values is striking.

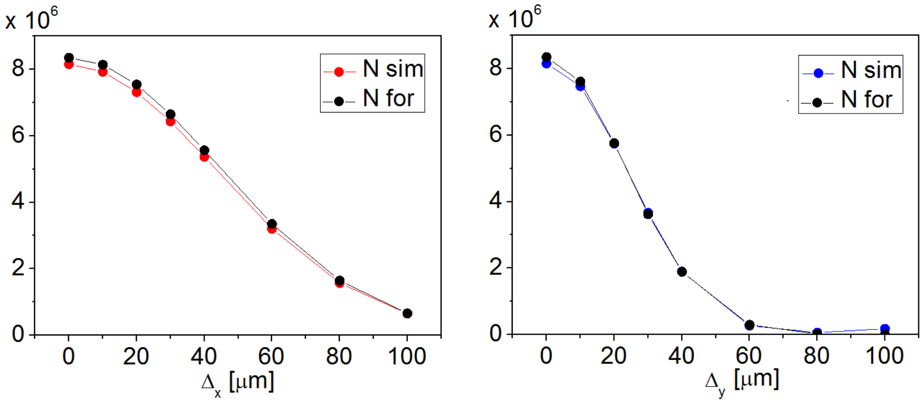

Figure 4.11: Total number of emitted photons as a function of the transverse misalignments Δ_x and Δ_y in red and blue respectively, in comparison with the value of N given by formula (4.6) represented in black.

Fig. 4.12 shows the decrease of the photon number caused by the increase of the misalignments in the x or in the y coordinates. The asymmetry in the two directions is due to the collision angle: the angle (in the $x-z$ plane) smooths the Δ_x effect. In the ELI-NP configuration, the laser recirculator causes a continuous variation of the focal plane, therefore the asymmetry is visible on the single shot but not on the flux per second. We notice that the transverse misalignments affect the flux but they have no consequences on the relative bandwidth value (the fluctuations are given by the statistics and the lower values to the low number of photons) neither on the polarization.

The longitudinal misalignment in the considered range have lower impact on the photon flux with respect to the transverse ones (see Fig. 4.13). Δ_z has no effects on the bandwidth (the small value differences in the bottom-left panel are due to the statistical fluctuations) and the polarization and it can be compensated by the synchronization.

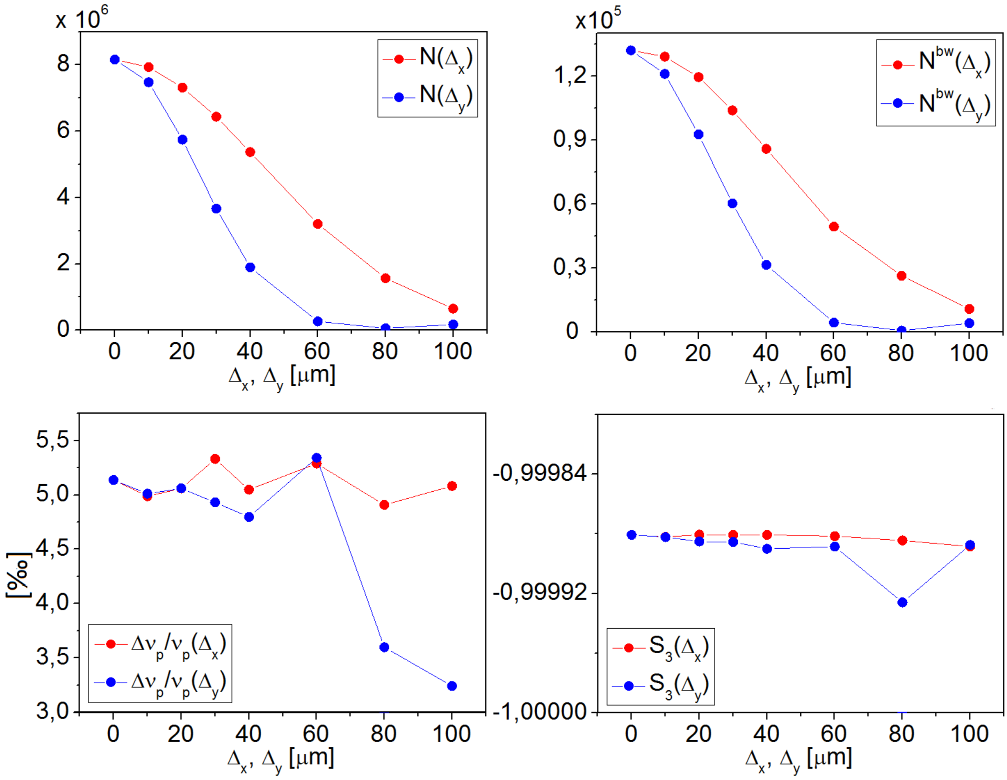

Figure 4.12: N, N^{bw}, $\Delta\nu_p/\nu_p$ [‰] and $\langle S_3\rangle$ as a function of Δ_x (red) and Δ_y (blue) [μm].

Let us now evaluate the impact of the spatial misalignments of the collimator on the emitted radiation, supposing a perfect laser and electron beam alignment. The collimator in our simulations is placed at 10 m from the IP, the collimator aperture is 1.92 mm (radius) (in order to have 0.005 bandwidth without misalignments) and the misalignments values are summarized in Table 4.7.

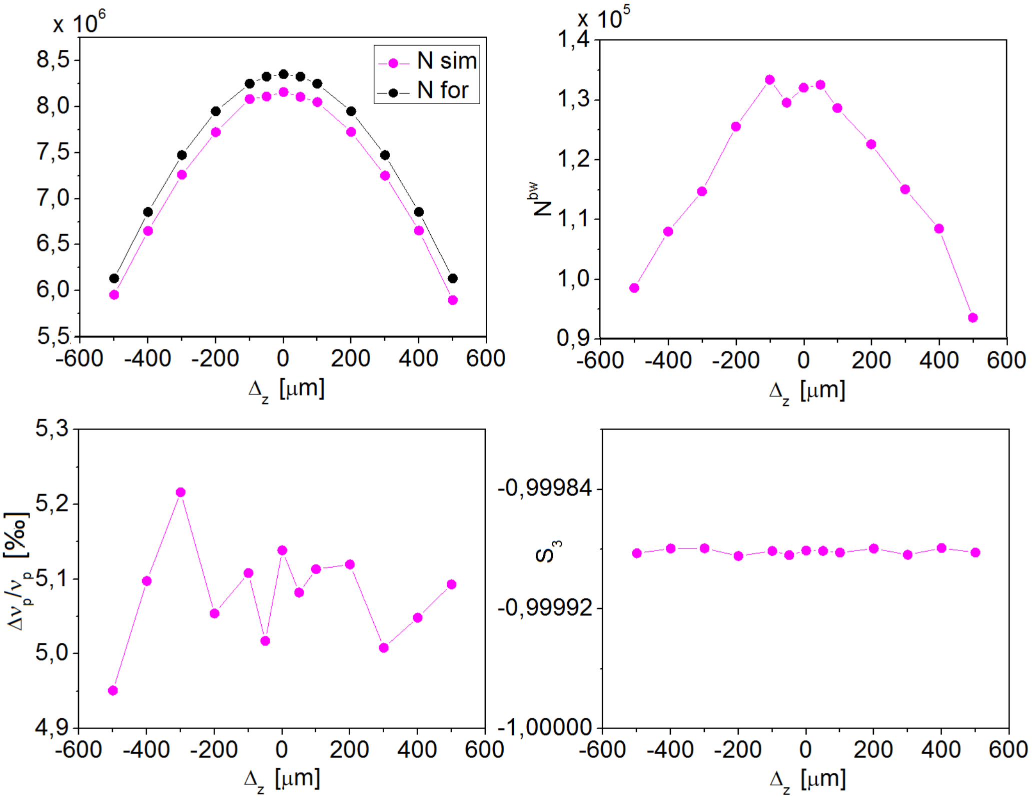

Figure 4.13: N, N^{bw}, $\Delta\nu_p/\nu_p$ [‰] and $\langle S_3 \rangle$ as a function of Δ_z (magenta) [μm]. The simulated N is compared to the values given by eq. (4.6) (black).

Table 4.7: Collimation system misalignment values C_x, C_y considered for the transverse space coordinates (in μm).

Collimator misalignment values [μm]								
C_x	0	50	100	150	200	300	500	700
C_y	0	50	100	150	200	300	500	700

Fig. 4.14 shows that even at large misalignment values ($500 - 700$ μm), the number of collimated photons remains constant (except for small numerical fluctuations). On the other hand the bandwidth value is affected by the displacements starting at 300 μm. No particular asymmetries in the two coordinates is visible at the misalignment values considered. A significant N^{bw} decrease can be noticed at C_x or C_y of some millimeters together with a x, y asymmetric behavior (see Fig. 4.15) given by the laser linear polarization.

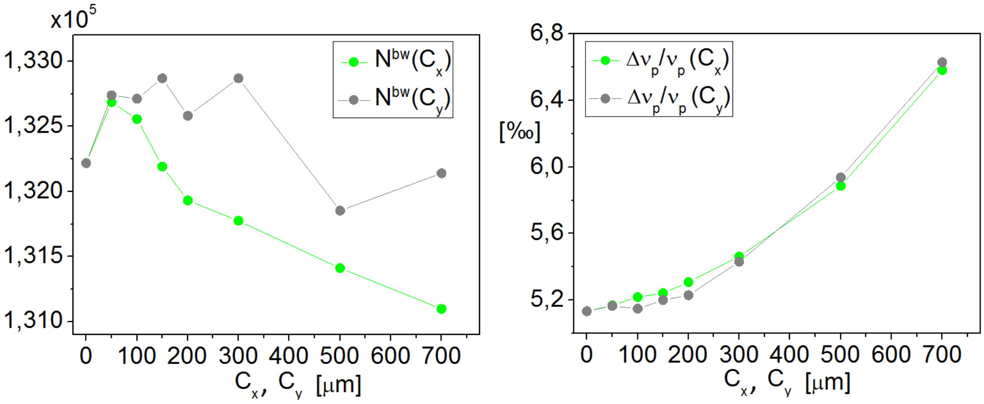

Figure 4.14: N^{bw} and $\Delta\nu_p/\nu_p$ [‰] as a function of C_x (green) and C_y (grey) [μm].

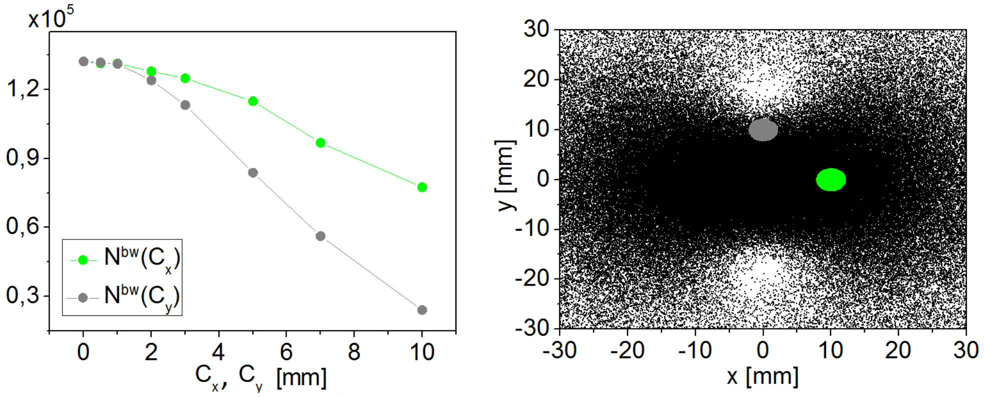

Figure 4.15: N^{bw} as a function of C_x (green) and C_y (grey) [mm] on the left. Transverse distribution of the total beam on a screen at 10 m from the IP in black, photons through the collimator for $C_x = 10$ ($C_y = 10$) mm in green (grey) on the right. The x and y coordinates are expressed in mm.

4.3.2 Errors and jitters on the electron beam line

The analysis of the photon flux and spectrum, taking into account all the possible errors and jitter of the electron beamline, is currently under study. We give here an example of simulation performed on a collection of 352 electron bunches provided by A. Bacci, A. Giribono and C. Vaccarezza [77]. The beams, constituted by 30000 macroparticles each, represent 352 machine settings affected by different random errors both on alignment and voltage of magnetic elements and accelerating structures of the beamline. The objective of our simulation is to evaluate the influence of all possible errors in the installations and in the productions of the accelerating structures and magnetic elements of the accelerator on the emitted radiation.

The errors in the position and in the operation of the magnetic elements and the accelerating structures, the misalignments and the jitters in the photoinjector system and the misalignlignments between the modules in the Linac beamline have been taken into account to produce the electron beams (see [78] for further informations). The main features of the 352 different electron beams are reported in Fig. 4.16.

The interaction simulations have been performed with the same laser parameters reported in Table 4.5 and the acceptance angle is $\theta_{max} = 192\ \mu$rad.

Fig. 4.17 shows the distribution of the 352 individual emitted photon beams characteristics: the mean energy, the relative bandwidth and the number of photons in the collimation angle.

The minimum, maximum and mean values of the above mentioned features are reported in Table 4.8. The last column, having title "opt", reports the values obtained by the simulation performed in the previous section (whose parameters are reported in Table 4.5) in the case of no misalignments.

Table 4.8: Minimum, maximum, mean and optimized (electron beam without errors and jitters reported in Table 4.5) values of mean energy $\langle h\nu_p \rangle$ [MeV], bandwidth $\Delta\nu_p$ [‰] and number of photons in the collimation angle N^{bw}.

	min	max	mean	opt
$\langle h\nu_p \rangle$ [MeV]	2.81	2.84	2.83	2.83
$\Delta\nu_p$ [‰]	5.06	6.03	5.47	5.13
N^{bw}	$9.04 \cdot 10^4$	$1.22 \cdot 10^5$	$1.05 \cdot 10^5$	$1.32 \cdot 10^5$

Fig. 4.18 represents the collimated spectrum and total photons in the collimation angle, produced by the 10560000 electrons in the 352 beams.

The direction of the 352 electron beams at the IP is parallel to the z axis, therefore in this simulation the electron beam angular displacements are not considered. We perform in the following a specific simulation to evaluate the electron beam displacement effects on the emitted radiation.

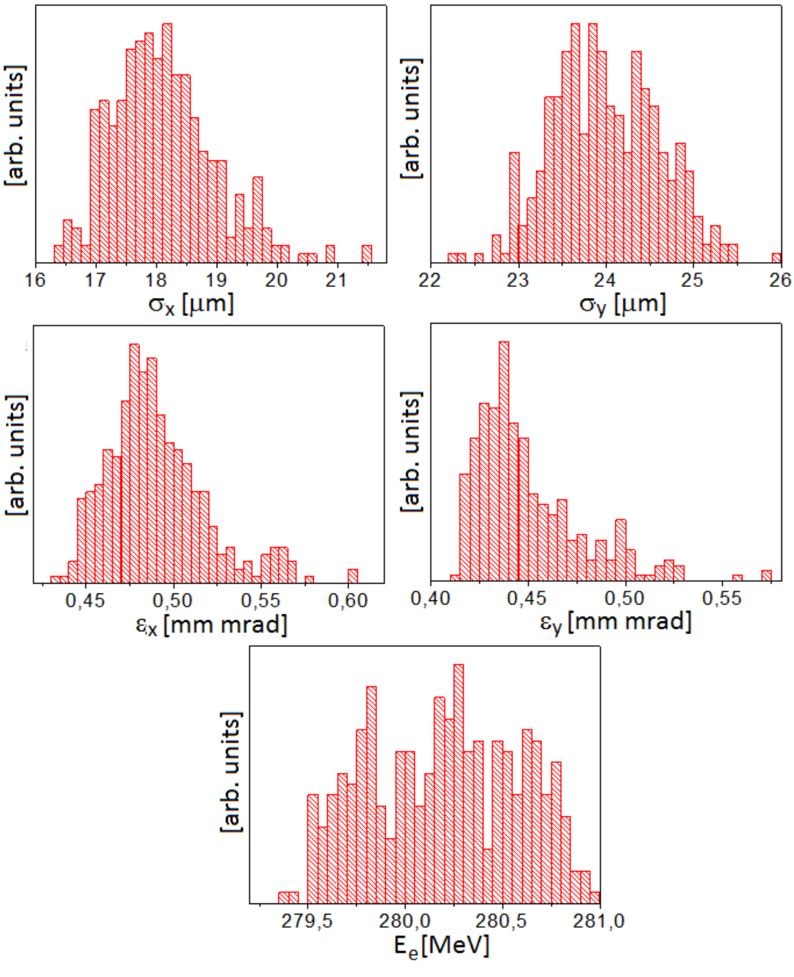

Figure 4.16: 352 electron beams characteristics: distribution of σ_x [μm], σ_y [μm], ϵ_x [mm·mrad], ϵ_y [mm·mrad] and energy E_e [MeV].

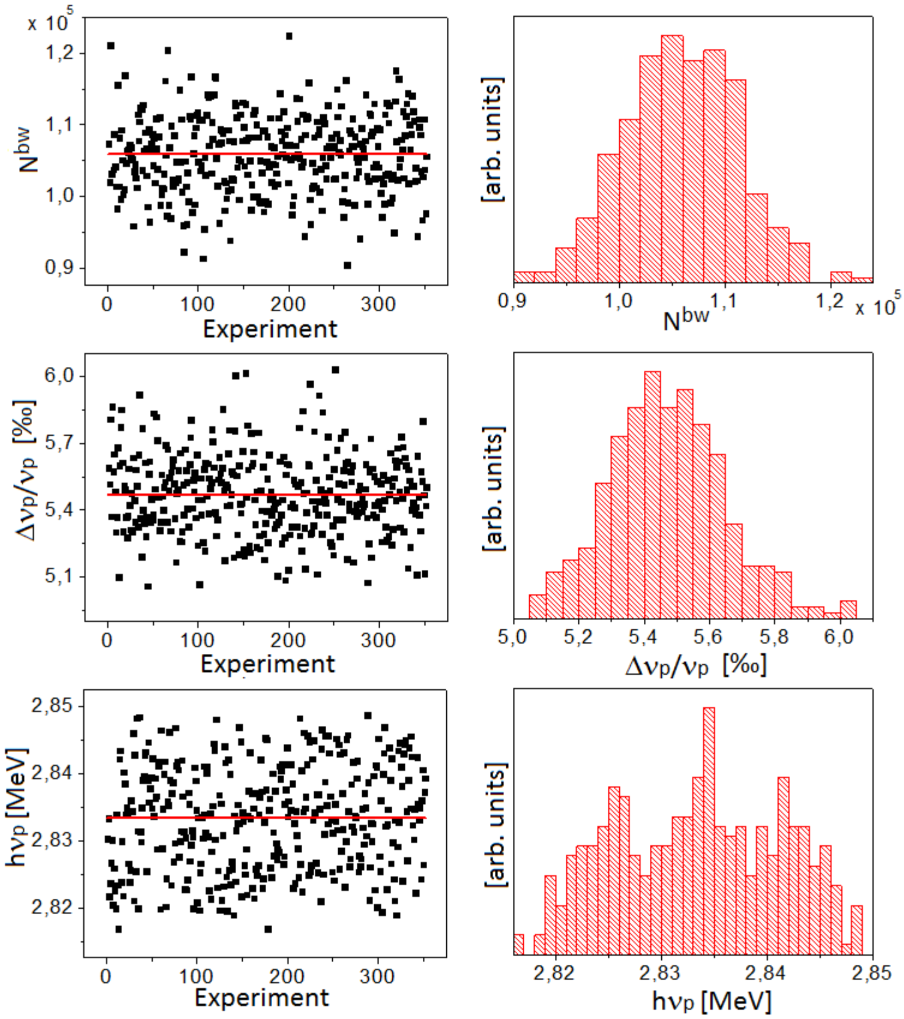

Figure 4.17: Features of the emitted photon beams for each incoming electron beam, i.e. for each experiment: value vs experiment (left column) and distribution (right column). From the top to the bottom: number of photons in the collimation angle, relative bandwidth [‰] and mean energy $\langle h\nu_p \rangle$ [MeV].

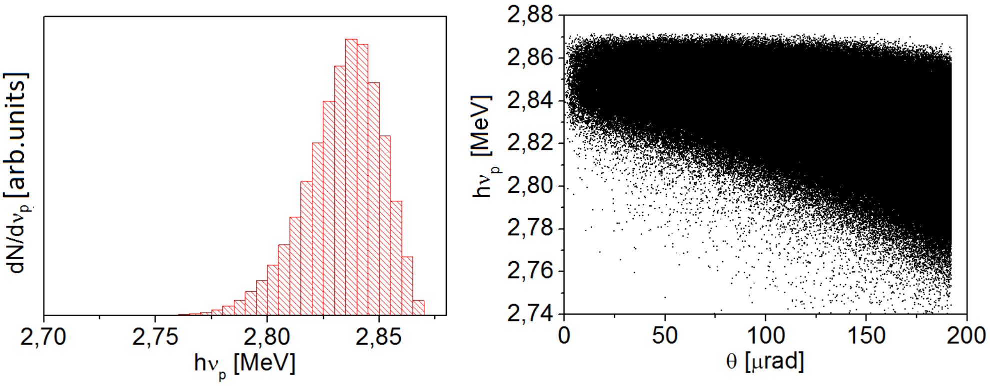

Figure 4.18: Collimated total spectrum and total photons in the collimation angle as a function of the angle θ [μrad].

We consider once again the incoming beams values in Table 4.5. The angular electron beam displacements are simulated by adding the transverse momentum values reported in Table 4.9 (there is no variation of the emittance value).

Table 4.9: Electron beam angular displacement values Δ_{p_x} and Δ_{p_y} (in keV).

El. angular displ. values [keV]							
Δ_{p_x}	0	7	14	21	28	56	70
Δ_{p_y}	0	7	14	21	28	56	70

The angular displacements, at the opposite respect to the spatial misalignments, have almost no impact on the flux but they strongly affects the bandwidth value. Fig. 4.19 shows the small fluctuations of N and N^{bw} and the steep increase of the relative bandwidth value as Δ_{p_x} or Δ_{p_y} increase. An asymmetry between the x and y coordinates is still present but it does not change significantly the results. We notice that also the polarization is slightly affected by the angular displacement. Δ_{p_x} and Δ_{p_y} have been expressed in terms of angles calculated as the ratio between the transverse momentum value and the longitudinal one.

Fig. 4.20 displays the effect of a $\Delta_{p_x} = 100$ μrad angular displacement on a screen perpendicular to z at 10 m from the IP: the center of the beam is at 2 mm (in x) from the center on of the screen.

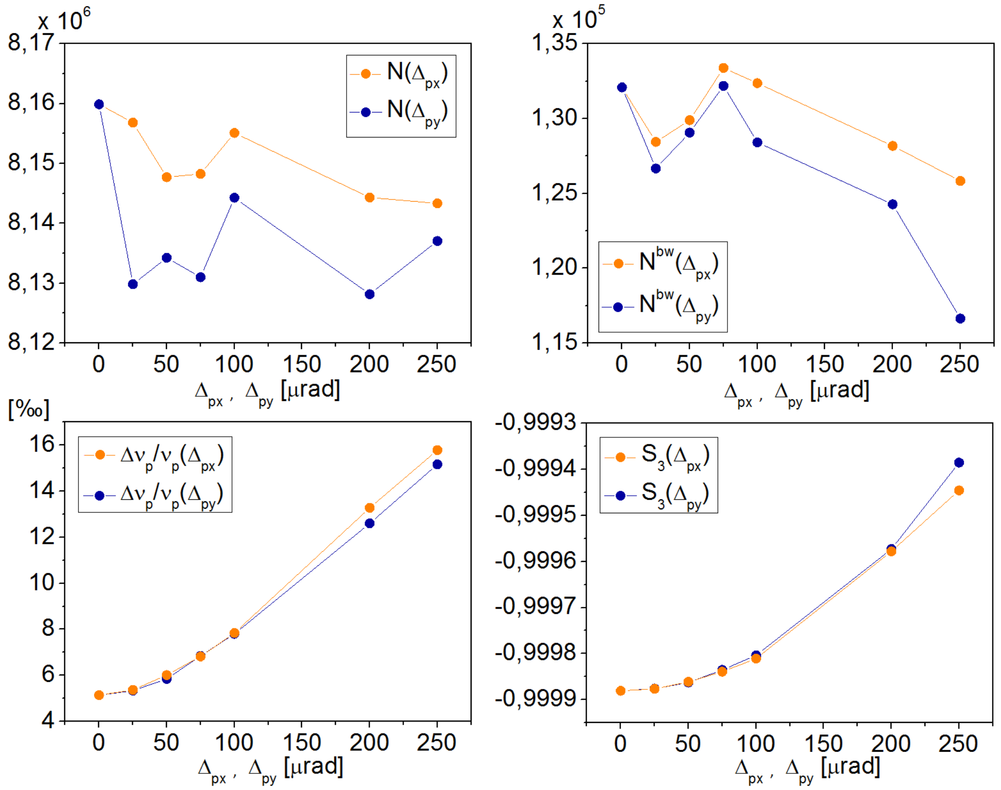

Figure 4.19: N, N^{bw}, $\Delta\nu_p/\nu_p$ [‰] and $\langle S_3\rangle$ as a function of Δ_{p_x} (orange) and Δ_{p_y} (blue) [μrad].

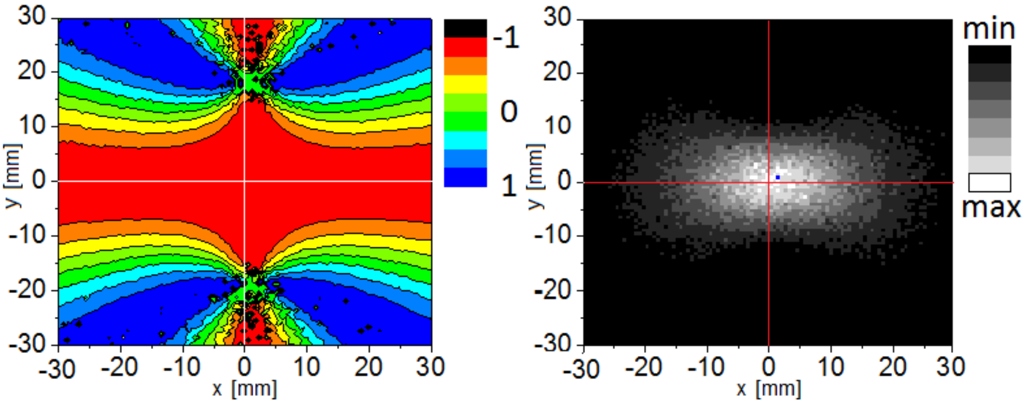

Figure 4.20: Stoke parameter mean value $\langle S_3\rangle$ (left) and space distribution (right) of the emitted photons on a screen perpendicular to the z axis at 10 m from the IP for $\Delta_{p_x} = 100$ μrad.

4.3.3 Laser position and orientation misalignments

The ELI-NP Linac will be operated in multibunch mode with a repetition rate of 100 Hz. To optimize the γ beam quality and to increase the laser beam power at IP, a passive optical recirculator has been designed [46]. The same laser pulse collides with the 32 bunches in the train. We analyze the data concerning the possible position and orientation misalignments of the laser pulse at the IP. The aim of the simulations is to evaluate the effects given by the production and installation errors of the laser on the emitted radiation. In our analysis we considered 1200 simulations, provided by K. Dupraz and F. Zomer [79], corresponding to as many experimental layouts. Each simulation produces the coordinates and the propagation direction of the laser pulse for the 32 passes at the IP.

Let us consider the interaction point for electron beam and laser pulse placed at (x, y, z) =(0, 0, 0). Fig. 4.21 presents the transverse misalignments of the laser pulse from the (x, y) = (0, 0) position for the 1200 simulated experiments.

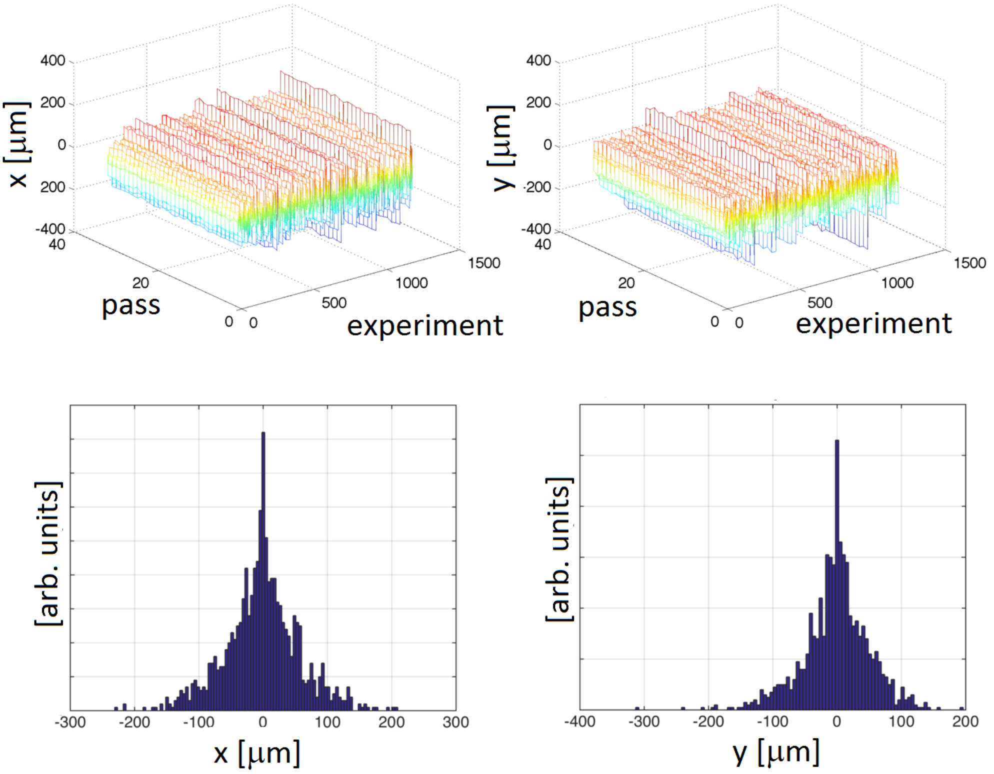

Figure 4.21: Top line: transverse displacement in x (y) on the right (left) of the laser pulse for the 1200 simulated experiments over the 32 passes at the IP. Bottom line: distribution of the mean value of x (right) and y (left) coordinate over the 32 passes for the 1200 experiments.

The mean value of the x, y coordinates is largely different for each experimental layout, and therefore the mean position distribution is spread on a wide range. However, the possible position displacements can be taken into account in the installation phase of the optical system. As we can see in Fig. 4.22, once the correction is performed by subtracting for each experiment the mean position value, the shifts of the x and y coordinates from the central point (0, 0, 0) is in the small range -10 μm $\leq \Delta_x$, $\Delta_y \leq$ 10 μm with a mean value of 5.2 μm and a 0.75 μm standard deviation as reported in Fig. 4.22.

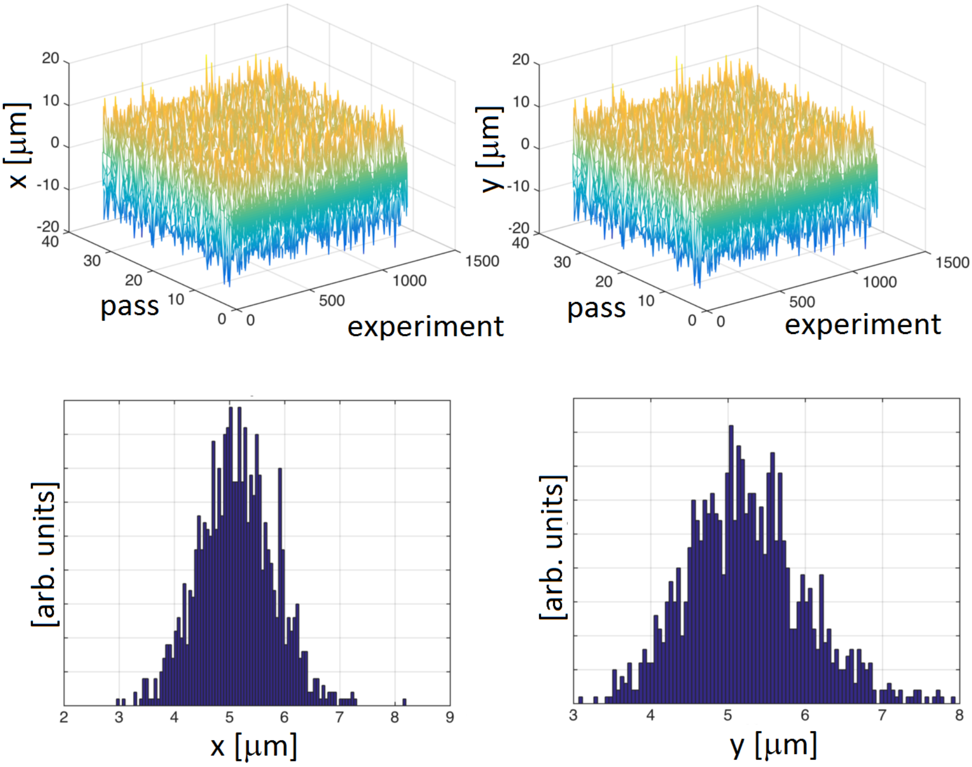

Figure 4.22: Top line: transverse displacement in x (y) on the right (left) of the laser pulse for the 1200 simulated experiments over the 32 passes at the IP after the mean value subtraction for each experiment. Bottom line: distribution of the mean value of x (right) and y (left) coordinate over the 32 passes for the 1200 experiments after the mean value subtraction for each experiment.

We chose randomly three of these corrected misalignment values and we perform the scattering simulation. The characteristics of the electron beam are: charge $Q = 250$ pC, transverse dimensions $\sigma_x = 10.4$ μm and $\sigma_y = 10.1$ μm, longitudinal dimension $\sigma_z = 0.27$ mm, energy $E_e = 720$ MeV, relative energy spread $5.60 \cdot 10^{-4}$ and emittance 0.4 mm·mrad. The laser pulse is characterized by a wavelength of $\lambda = 515$ nm, pulse energy $E_L = 0.2$ J, waist $w_0 = 28$ μm and pulse length 1.5 ps.

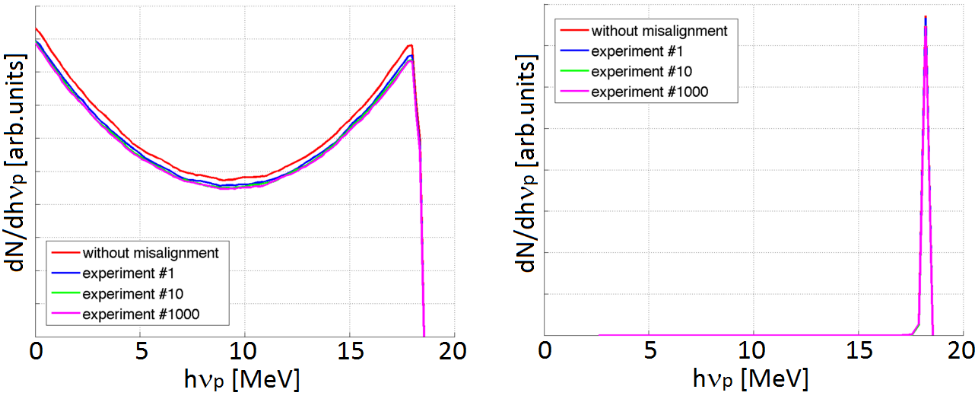

Figure 4.23: Spectrum of the emitted photons obtained by the collision of a 720 MeV electron beam and a 515 nm wavelength laser. Three space misalignments between the 1200 have been considered. Left: full solid angle. Right: spectrum in the acceptance angle 48 μrad (corresponding to a 5 ‰relative bandwidth).

The emitted photon total spectrum and the collimated spectrum within an acceptance angle of 48 μrad are shown in Fig. 4.23. As can be seen, the transverse misalignments produce a slight decrease in the photon number accounted on the whole solid angle, while on the collimated case no appreciable effects in terms of flux and bandwidth can be observed.

Concerning the angular displacements, Fig. 4.24 presents the distribution of the angle α_0 around the central value of 7.5^o obtained for all the 1200 simulations. The standard deviation of the distribution around the mean value of 7.5^o is 0.005 degrees.

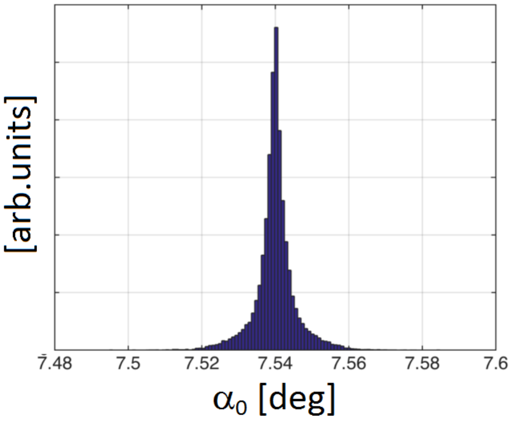

Figure 4.24: Angular displacement distribution of the 1200 simulated set up.

Another simulation with the same laser and electron beam parameters above mentioned have been performed on a set of three random chosen angular displacement values within the 1200. Fig. 4.25 shows that the considered angular displacements have no relevant effect on the flux and the bandwidth of the emitted radiation.

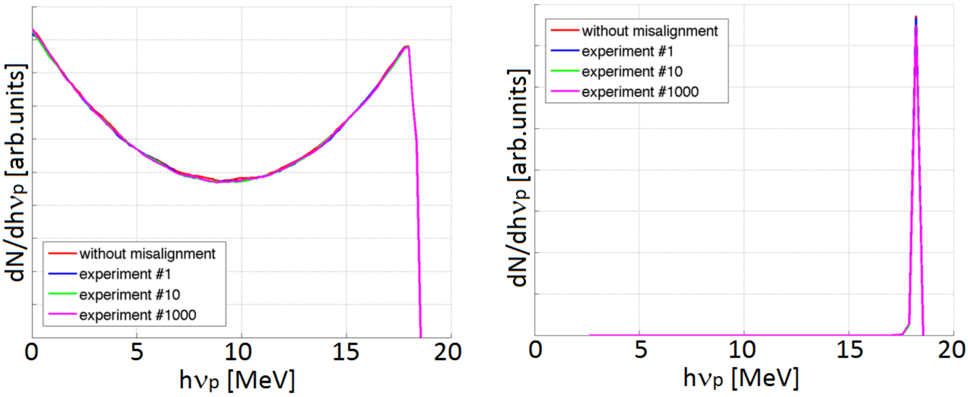

Figure 4.25: Spectrum of the emitted photons obtained by the collision of a 720 MeV electron beam and a 515 nm wavelength laser. Three angular displacements between the 1200 have been considered. Left: full solid angle. Right: spectrum in the acceptance angle 48 μrad (corresponding to a 5 ‰relative bandwidth).

In Fig. 4.26, the combined effect of transverse and angular laser misalignment is presented. The total flux decrease is about 6%, while the collimated spectrum and the bandwidth value are not affected.

After a more recent study of the laser recirculator [47], the EuroGammaS collaboration decided to set the optimal value for the α_0 angle at 8^o. The rms value of the displacements from this new value of α_0 are of the same order as the one reported in the set of simulations we just presented. From the general analysis we performed on the laser misalignments and the displacements impact on the emitted radiation, we can say that these contained values have a very slight impact on the emitted radiation properties.

At last we show the results of a simulation performed on the primary beams values reported in Table 4.5 for $\alpha_0 = 0^o$, 2^o, 4^o, 8^o and 16^o. Fig. 4.27 reports the variation of the number of photons, the bandwidth and the emitted photon beam spectrum given by different values of the collision angle. A 8^o collision angle causes a 50% loss on the number of photons. α_0 has no impact on the bandwidth value but it originates a downshift of the peak value of the emitted photons.

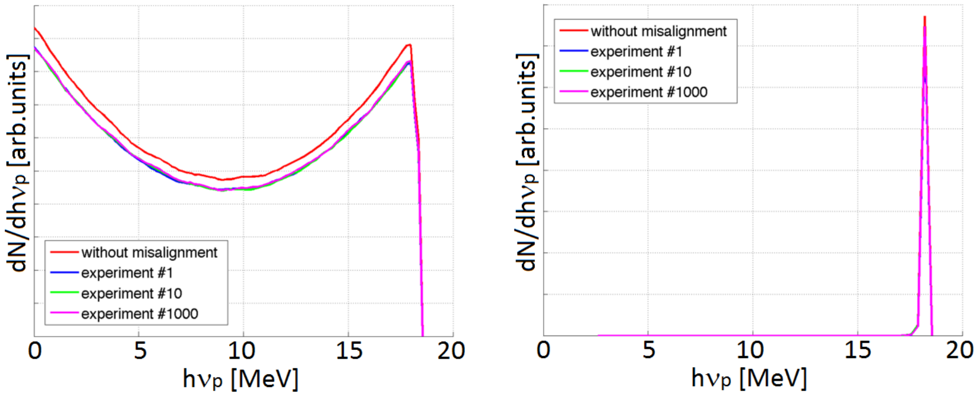

Figure 4.26: Spectrum of the emitted photons obtained by the collision of a 720 MeV electron beam and a 515 nm wavelength laser. A combination of three space misalignments and three angular displacements between the 1200 have been considered. Left: full solid angle. Right: spectrum in the acceptance angle 48 μrad (corresponding to a 5 ‰relative bandwidth).

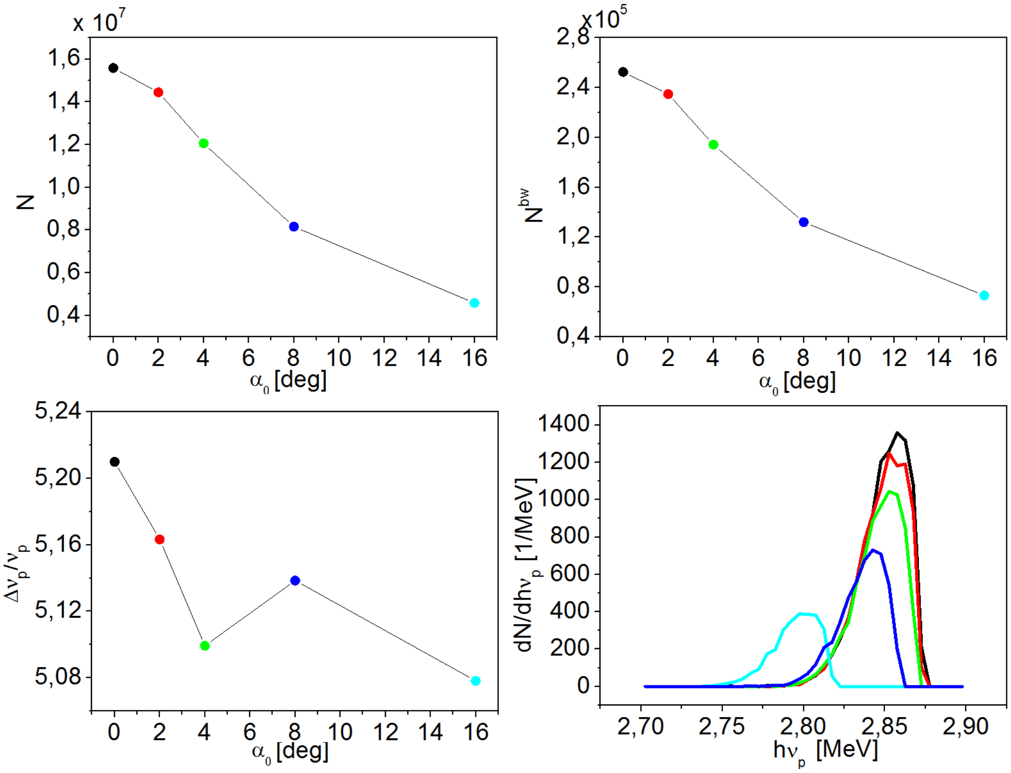

Figure 4.27: α_0 variation 0^o (black), 2^o (red), 4^o (green), 8^o (blue) and 16^o (cyan). N, N^{bw} and $\Delta\nu_p/\nu_p$ [‰] as a function of α_0 expressed in [rad].

Part II

Pion/muon low emittance beams photo-production

CHAPTER 5

Hadron-Photon Collider

Present availability of high brilliance photon beams as those produced by X-ray Free Electron Lasers in combination with intense TeV proton beams typical of the Large Hadron Collider (LHC) makes it possible to conceive the generation of pion and muon beams via photo-production in a highly relativistic Lorentz boosted frame: the main advantage is the low emittance attainable and a TeV-class energy for the generated particles, that may be an interesting option for the production of low emittance muon and neutrino beams. In the following we will describe the kinematics of all the events given by the proton-photon beams interaction: the pion photo-production, the lepton pair photo-production (electron/positron and muon pairs) and Compton scattering. Based on the phase space distributions of the pion and muon beams we will analyze the beams brightness achievable in three examples, based on advanced high efficiency high repetition rate FELs coupled to LHC or Future Circular Collider (FCC) proton beams, together with the study of a possible small scale demonstrator based on a Compton Source coupled to a Super Proton Synchrotron (SPS) proton beam.

Muon colliders, as Higgs factories, represent a promising way to achieve the highest lepton-antilepton collision energies and precision measurements of the Higgs boson and for further study of its properties. Moreover, muons are ideal sources for neutrino beams of unprecedented quality and precision through their purely leptonic decay [81,82]. One of the main challenges of present muon collider design studies is the capture and cooling stage of muons after generation by intense GeV-class proton beams impinging on solid targets: this mechanism produces pions further decaying into muons and neutrinos. As extensively analyzed in Refs. [83, 84], the large emittance of the generated pion beams, which is mapped into the muon beam, is mainly given by the mm-size beam source at the target (i.e. the proton beam focal spot size) and by Coulomb scattering of protons and pions propagating through the target itself, inducing large transverse momenta which in turns dilute the phase space area. Recently the option to use hundreds of MeVs photons to make muon pairs via photo-production in a solid target was analyzed in Ref. [85], with the aim of getting a smaller source spot size, avoiding as well the proton beam scattering effects. This scheme is promising in terms of low emittance of the muon beams at the source, but unfortunately it turns out that the low energy of the generated muons and the transport process into the high field solenoid system induces an irreversible emittance growth. Therefore the small source emittance of muons produced in the Bethe-Heitler process does not compensate its very low efficiency [86].

We propose here a different approach, still based on photon beams, enabled by the present availability of outstanding TeV-class high intensity proton beams and ultra-high brilliance X-ray photon beams obtained by advanced X-ray Free Electron Lasers: their combined capability of producing ultra-high phase space density particle beams is the base of our strategy for generating low emittance pion, muon and neutrino beams, using collisions between two counter-propagating beams of highly relativistic protons and ultra-high intensity photons. The extremely high luminosity achievable by such a collider (10^{38} $\mathrm{cm}^{-2}\mathrm{s}^{-1}$) can compensate, for example, the low efficiency of the pion photo-production which has a maximum total cross section of $\simeq 220$ μbarn, much smaller than GeV-proton based pion production ($\simeq 20$ mbarn).

There are two crucial aspects in such a collision scheme. The first is the much higher energy of the X-ray photons observed by the proton in its own rest frame: this enables pion photo-production above the threshold with maximum efficiency, despite the keV energy of the colliding photon. The second deals with the proton carrying almost the total momentum of the system, which makes it the source of highly Lorentz boosted secondary beams collimated within a narrow forward angle of the same order of the proton beam diffraction angle given by its transverse emittance (tens of mm·mrads). In this sense the mechanism for pion/muon production described in the following represents sort of a relativistic pion/muon photo-cathode. A similar approach has been proposed and discussed in Ref. [105] although based on a multi-photon production of pion and muon pairs, which is a much lower efficiency process.

We considered two examples of TeV proton beams: an upgraded LHC [87,88] beam carrying up to $2 \cdot 10^{11}$ protons per bunch at 7 TeV energy focused down to 7 μm at the interaction point with a normalized transverse emittance $\epsilon_{nx} = 1.4$ mm·mrad and an FCC [89–91] expected beam at the same bunch intensity with 50 TeV energy, a spot size of 1.6 μm and $\epsilon_{nx} = 2.2$ mm·mrad, both with a repetition rate up to 40 MHz.

Photon beams at energies ranging between 3 and 20 keV and more than 10^{13} photons per pulse at MHz repetition rate can be obtained with SuperConductive (SC) Continuous Wave (CW) Linac based XFELs, in saturation regime for the energies lower than few keV and in the tapering mode for larger energies. The brilliance of XFEL photon beams coupled to X-ray optics technology [92,93] allows focusing the FEL photon beam down to spot sizes $\simeq 10$ μm comparable to LHC proton beam at the interaction point, in order to maximize the luminosity of proton-photon collider. In Table 5.1, data taken from Ref. [94,95] show the status of art of the FEL simulations in these regimes.

Fluxes close or larger than 10^{13} photons per pulse are achieved for energies smaller

Table 5.1: FEL performance: mode (tapering or saturation), photon energy hν [keV], electron beam charge [nC], number of produced photons.

Ref.	Mode	$h\nu$ [keV]	e-beam [nC]	Photon #
[94]	Tapering	8.25	0.16	$3 \cdot 10^{13}$
[95]	Saturation	< 1.65	1	$> 10^{13}$
[95]	Tapering	< 3	> 0.1	$10^{13} \div 10^{14}$
[95]	Tapering	< 2	1	$> 10^{14}$
[95]	Tapering	20	> 0.2	$2 \cdot 10^{13}$

than 1.65 keV in the saturated mode. The tapering allows to maintain the flux value while enhancing the energy. By applying the FEL scaling laws to the data reported in Ref. [95] for the case of hundreds femtoseconds long electron bunches allows to envision the possibility of exceeding 10^{13} photons at 20 keV.

The 400 GeV beam of SPS [96] carrying $2 \cdot 10^{12}$ protons coupled with a Compton source such as SPARC-LAB [97–99] would be feasible for a demonstrator: the Compton sources are the only compact devices capable to deliver hundreds keV highly monochromatic photon beams. The maximum number of photons per pulse reachable nowadays (around 10^{8-9}) is not sufficient for a full scale experiment.

One of the main characteristics of both the FEL and the Compton sources is the tunability of the radiation wavelength, which allows an easy adjustment of the photon energy in order to optimize the collision to the desired performances.

In the next chapter we go through the details of all the processes produced by the head-on collision of the proton and the photon beams, showing the results obtained by our home made event-generator codes implemented for the pion photo-production and the further decay into muon and neutrino, the lepton pair photo-production (electron/positron and muon pairs) and the Inverse Compton scattering. The number of these events given by the total cross sections and the luminosities are commented and discussed in the dedicated chapter.

CHAPTER 6

Pion/muon photo-production in a highly Lorentz boosted frame

Let us consider the collision between a proton and a counter-propagating photon of energy respectively E_p and $h\nu$ in the laboratory frame (LAB). The energy $h\nu'$ of the colliding photon in the proton rest frame is given by (relativistic Döppler effect)

$$h\nu' = h\nu\gamma(1 - \underline{\beta} \cdot \underline{e}_k) \tag{6.1}$$

where $\underline{\beta}$ is the velocity of the proton, $\underline{e}_k$ is the direction of propagation of the photon, $\gamma = E_p/M_p$ and $M_p = 938$ MeV/c^2. For an ultra-relativistic proton colliding head-on with a photon, the formula simplifies in $h\nu' \simeq 2\gamma h\nu$. At the interaction, from the kinematic point of view we have one "particle" with 4-momentum $P = \{E_p + h\nu, \underline{p}_p + \underline{k}\}$. Since P^2 is Lorentz invariant, the energy E_{CM} (or invariant mass M) available in the center of mass CM of the proton-photon system is

$$E_{CM} = M = \sqrt{P^2} = \sqrt{2E_p h\nu - 2(\underline{p}_p \cdot \underline{k}) + M_p^2}. \tag{6.2}$$

Assuming an incident photon with energy much smaller than the proton, i.e. $h\nu << E_p$

$$\gamma_{CM} = \frac{E_{tot}^{LAB}}{E_{CM}} \simeq \frac{E_p + h\nu}{\sqrt{4E_p h\nu + M_p^2}}. \tag{6.3}$$

As an example, if $E_p = 7$ TeV and $h\nu = 20$ keV we have $h\nu' = 298$ MeV, $E_{CM} = 1199$ MeV and $\gamma_{CM} = 5834$.
Once we define the parameter representing the recoil of the proton in the collision as

$$\Delta_p \equiv \frac{4\gamma h\nu}{M_p}, \tag{6.4}$$

we can write $E_{CM} \simeq M_p\sqrt{1 + \Delta_p}$ and $\gamma_{CM} \simeq \gamma/\sqrt{1 + \Delta_p}$.

The dominant reactions when the photon energy $h\nu'$ seen by the proton is in the range $100-300$ MeV are pion photo-production, lepton pair photo-production (electron-positrons and muon pairs) and Inverse Compton scattering. We discuss here the kinematics of

this hadron-photon collider scenario using TeV protons colliding with keV photons to produce high energy low emittance pion and muon beams in a highly Lorentz boosted kinematics. The most promising process for the muon production is the pion production and its decay into muon and neutrino, but we will also consider in detail the direct muon pair production that despite the very low cross section would deliver muon and antimuon at the same time.
In this chapter we use natural units $c = \hbar = 1$ and denote with $*$ the particles' momenta and energies in their center of mass reference frame.

6.1 Muon production through pion production and decay

At first we consider the reaction is

$$p + h\nu \rightarrow \pi^+ + n.$$

Once the collision of proton and photon occurs and we have the one "particle" with mass $M = E_{CM}$, the pion and neutron momenta in CM are:

$$\begin{aligned} p^*_\pi = p^*_n = \frac{\sqrt{E^4_{CM} + (M^2_\pi - M^2_n)^2 - 2E^2_{CM}(M^2_\pi + M^2_n)}}{2E_{CM}} = \\ \frac{1}{2}\sqrt{M^2_p(1+\Delta_p) + \frac{(M^2_\pi - M^2_n)^2}{M^2_p(1+\Delta_p)} - 2(M^2_\pi + M^2_n)} \end{aligned} \tag{6.5}$$

where $M_\pi = 139.6$ MeV/c^2 and $M_n = 939.565$ MeV/c^2 are pion and neutron invariant masses. For $E_p = 7$ TeV and $h\nu = 20$ keV, $p^*_\pi = p^*_n = 195$ MeV/c.
Massive particles like pions or muons can be generated only above some threshold due to kinematics, and they always propagate along the same direction of CM in the laboratory [1], typically very collimated within narrow angles due to the high Lorentz boost imparted by the ultra-relativistic protons. The reaction threshold is set by $p^*_\pi = p^*_n = 0$, corresponding to $\Delta^{th}_p = (M_\pi + M_n)^2/M^2_p - 1 = 0.324$ (since $E^{th}_{CM} = M_p\sqrt{1+\Delta^{th}_p} = M_\pi + M_n$) and a photon minimum energy $h\nu^{th} = M_p\Delta^{th}_p/4\gamma \simeq 76$ [MeV] $/\gamma$, equivalent to $h\nu'^{th} = 152$ MeV seen by the proton (i.e. $h\nu^{th} \simeq 10$ keV for $E_p = 7$ TeV and $h\nu^{th} \simeq 1.4$ keV for $E_p = 50$ TeV).

---

[1] The angle at which the produced particles are emitted in the laboratory frame depends on the relation between the velocity of the particles in CM (β^*) and the velocity of CM in LAB (β_{CM}):

- if $\beta_{CM} > \beta^*$ the particle is emitted forwards with respect to the direction of CM in the laboratory;
- if $\beta_{CM} < \beta^*$ the particle can be emitted at any angle in the laboratory.

In the scenarios we are going to analyze in the following, the massive particles (pions, neutrons, muons) are characterized by β^* always lower than the β_{CM}, while for the lighter particles (electrons, positrons, neutrinos) and the photons we may have $\beta_{CM} < \beta^*$. Therefore, in the latter case some of the emitted particles (usually few of them) have a negative longitudinal momentum in LAB.

If the proton is directed along the z axis and the photon is perfectly counter-propagating, the momentum components of the pion in LAB are

$$\begin{cases} p_{\pi_x} &= p_\pi^* \sin\theta^* \cos\phi^* \\ p_{\pi_y} &= p_\pi^* \sin\theta^* \sin\phi^* \\ p_{\pi_z} &= \gamma_{CM}\left(\beta_{CM} E_\pi^* + p_\pi^* \cos\theta^*\right) \end{cases} \tag{6.6}$$

where $\beta_{CM} = \sqrt{1 - \frac{1}{\gamma_{CM}^2}}$, $E_\pi^* = \sqrt{p_\pi^{*2} + M_\pi^2}$ and θ^* and ϕ^* are the angles in CM with respect to $\underline{\beta}_{CM}$ which in this case is $\underline{\beta}_{CM} = \beta_{CM}\underline{e}_z$.

The angle θ_π of the pion in the LAB frame with respect to the z axis is

$$\theta_\pi = \arctan\left(\frac{\sqrt{p_{\pi_x}^2 + p_{\pi_y}^2}}{p_{\pi_z}}\right) = \arctan\left(\frac{\sin\theta^*}{\gamma_{CM}\left(\frac{\beta_{CM}}{\beta^*} + \cos\theta^*\right)}\right) \tag{6.7}$$

where $\beta^* = p_\pi^*/E_\pi^*$ is the velocity of the pion in CM and

$$\gamma_\pi = \frac{\sqrt{p_{\pi_x}^2 + p_{\pi_y}^2 + p_{\pi_z}^2 + M_\pi^2}}{M_\pi}. \tag{6.8}$$

The other reaction product, the neutron, is treated with the same approach as the pion and it is characterized by $E_n^* = \sqrt{p_n^{*2} + M_n^2}$.
For example Fig. 6.1 shows the x and z momentum components of a pion and a neutron emitted in the collision of a proton at $E_p = 7$ TeV and $h\nu = 20$ keV perfectly counter-propagation along z. In CM (left window) the two particles are emitted in opposite directions while the pure longitudinal Lorentz boost transforms the momentum components in the passage to the LAB frame (window on the right): we notice that the transverse components are invariant while the longitudinal ones are greatly enhanced (the scale changes from MeV/c to TeV/c).

In order to evaluate the emittance of the generated pion and neutron beams it is useful to evaluate the first order behavior of the momentum in the CM frame just above threshold, i.e.

$$p_\pi^{*\,th} = p_n^{*\,th} \simeq \frac{M_p}{2}\sqrt{1 - \frac{(M_\pi^2 - M_n^2)^2}{(M_\pi^2 + M_n^2)^4}}\sqrt{\Delta_p - \Delta_p^{th}} \simeq 315\ [\text{MeV}]\ \sqrt{\Delta_p - \Delta_p^{th}}.$$

As mentioned above the transverse momenta are invariant to Lorentz transformations along the perpendicular direction from CM to LAB frames, therefore the normalized transverse emittance of the pion beam at the interaction point is given by

$$\epsilon_n^{\pi_x} = \frac{\sigma_0}{\sqrt{2}}\sqrt{\langle \overline{p}_{\pi_x}^2 \rangle} \tag{6.9}$$

where we use the dimensionless transverse momentum defined as $\overline{p}_{\pi_x} \equiv p_{\pi_x}/M_\pi$, the average is performed over the phase space distribution area and σ_0 is the proton beam

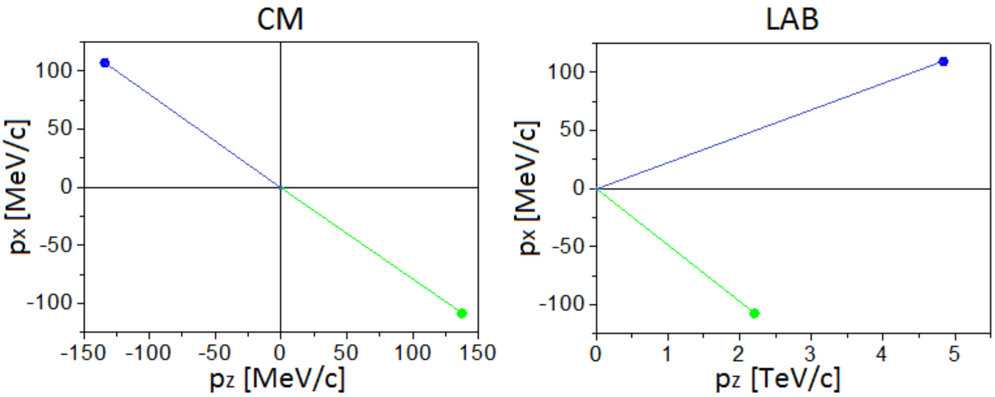

Figure 6.1: Example of a simulated pion-neutron emission: pion (in green) and neutron (in blue) momentum components in CM (left) and the transformation to the LAB (right) in the case of a pure longitudinal boost for $E_p = 7$ TeV and $h\nu = 20$ keV.

spot size at the interaction point. The factor $1/\sqrt{2}$ represents the emitted beams rms spot size decrease (see discussion in Chapter 4): in this case we assumed a perfect overlap of the two Gaussian colliding beams with the same spot size σ_0. We can derive the thermal normalized emittance of the pion beam, due to the collision transverse temperature, as

$$\epsilon_{n-cath}^{\pi x} = \frac{2.25}{\sqrt{3}} \frac{\sigma_0}{\sqrt{2}} \sqrt{\Delta_p - 0.324} \tag{6.10}$$

assuming a uniform distribution of momenta in the transverse phase space of the pion beam.

Let us recall that the peak in the total cross section for pion photo-production is reached when the incident photon energy in the laboratory (with protons at rest) is about 300 MeV [107,111]: in our case $h\nu' = 300$ MeV corresponds to about $\Delta_p = 0.64$, which implies a thermal emittance for the pion beam of about $\epsilon_{n-cath}^{\pi x} = 0.49 \cdot \sigma_0$. We will see further on that the total pion beam emittance $\epsilon_n^{\pi x}$ is given by the contribution of the proton beam emittance $\epsilon_n^{p_x}$ and of the thermal emittance $\epsilon_{n-cath}^{\pi x}$ generated by the equivalent pion photo-cathode effective temperature. Approaching the pion production threshold ($h\nu' \simeq 150$ MeV), the total cross section decreases drastically, but if we consider a photon energy $h\nu' \simeq 180$ MeV the value of Σ_π is around 80 μbarn and for $h\nu' \simeq 200$ MeV $\Sigma_\pi \simeq 100$ μbarn (almost half of the peak value) as shown in Fig. 6.2.

Using the expression for CM momentum close to threshold, p_π^{*th}, and evaluating the difference between the maximum pion momentum in the laboratory $p_{\pi_z}(\theta^* = 0)$ and the minimum one $p_{\pi_z}(\theta^* = \pi)$, we derive the rms energy spread of the pion beam as

$$\left.\frac{\Delta\gamma}{\gamma}\right._{\pi} = f\sqrt{\Delta_p - 0.324} \tag{6.11}$$

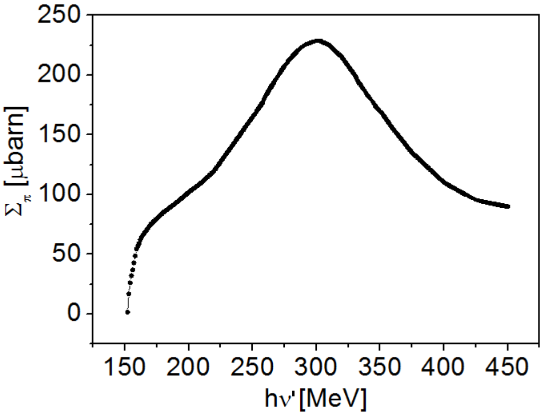

Figure 6.2: Total cross section [μbarn] for pion photo-production as a function of the incoming photon energy [MeV] for a proton at rest. Data from Ref. [107].

with

$$f = \frac{M_p}{2\sqrt{3}M_\pi}\sqrt{1 - \frac{(M_\pi^2 - M_n^2)^2}{(M_\pi^2 + M_n^2)^4}} = 1.3 \tag{6.12}$$

if a uniform longitudinal momentum distribution in phase space is assumed. It is interesting to notice that at the threshold both pions and neutrons travel at the same speed as the center of mass along the proton propagation axis, in fact $p_{\pi_z}^{th} = M_\pi\sqrt{\gamma_{CM}^2 - 1}$ and $E_\pi^{th} = M_\pi\gamma_{CM}$, while $\gamma_\pi = \gamma_n = \gamma_{CM} = \gamma/\sqrt{1 + 0.324} = 0.87 \cdot \gamma$ ($E_\pi^{th} = 6.5$ TeV at $E_p = 50$ TeV).

For a pion at rest in the laboratory frame the mean life-time is $\tau_\pi = 2.6 \cdot 10^{-8}$ s to decay into a muon and a neutrino according to the following reaction:

$$\pi^+ \to \mu^+ + \nu_\mu.$$

In our case the pion mean life-time is $\gamma_\pi \cdot \tau_\pi$, which implies pions propagating over long distances (hundred meters to several kms). In the following we will populate the phase space volumes of the generated pion and muon beams neglecting effects coming from this long range pion propagation: the reason for this assumption is to focus the present analysis on the secondary beam generation process and leaving to a future work the study about matching the generated beams into a further storage/acceleration stage.

The muon momentum in its center of mass CM (the pion) is

$$p_\mu^* = \frac{M_\pi^2 - M_\mu^2}{2M_\pi} \tag{6.13}$$

where $M_\mu = 105.65$ MeV/c^2. The energy of the muon in CM is $E_\mu^* = \sqrt{p_\mu^{*2} + M_\mu^2}$ and the momentum is $\underline{p}_\mu^* = (p_{\mu_x}^*, p_{\mu_y}^*, p_{\mu_z}^*) = (p_\mu^* \sin\theta^* \cos\phi^*, p_\mu^* \sin\theta^* \sin\phi^*, p_\mu^* \cos\theta^*)$ with

θ^* and ϕ^* angles in CM with respect to $\underline{\beta}_\pi$. Since the pion decays while moving in the direction given by the components of its momentum, in order to define the components of the muon momentum in the laboratory frame, we use the Lorentz transformations for a boost in a generic direction with $\gamma_{CM} = \gamma_\pi$ as follows:

$$\begin{cases} p_{\mu_x} = \dfrac{E^*_\mu p_{\pi_x}}{M_\pi} + p^*_{\mu_x}\left(1 + \dfrac{p^2_{\pi_x}}{(\gamma_\pi + 1)M^2_\pi}\right) + p^*_{\mu_y}\left(\dfrac{p_{\pi_x}p_{\pi_y}}{(\gamma_\pi + 1)M^2_\pi}\right) + p^*_{\mu_z}\left(\dfrac{p_{\pi_x}p_{\pi_z}}{(\gamma_\pi + 1)M^2_\pi}\right) \\ p_{\mu_y} = \dfrac{E^*_\mu p_{\pi_y}}{M_\pi} + p^*_{\mu_x}\left(\dfrac{p_{\pi_x}p_{\pi_y}}{(\gamma_\pi + 1)M^2_\pi}\right) + p^*_{\mu_y}\left(1 + \dfrac{p^2_{\pi_y}}{(\gamma_\pi + 1)M^2_\pi}\right) + p^*_{\mu_z}\left(\dfrac{p_{\pi_y}p_{\pi_z}}{(\gamma_\pi + 1)M^2_\pi}\right) \\ p_{\mu_z} = \dfrac{E^*_\mu p_{\pi_z}}{M_\pi} + p^*_{\mu_x}\left(\dfrac{p_{\pi_x}p_{\pi_z}}{(\gamma_\pi + 1)M^2_\pi}\right) + p^*_{\mu_y}\left(\dfrac{p_{\pi_y}p_{\pi_z}}{(\gamma_\pi + 1)M^2_\pi}\right) + p^*_{\mu_z}\left(1 + \dfrac{p^2_{\pi_z}}{(\gamma_\pi + 1)M^2_\pi}\right). \end{cases} \tag{6.14}$$

In the case of a pure longitudinal boost, p^*_π as given in eq. (6.5) represents the maximum value of the pion transverse momentum also in the laboratory frame because of the invariance of transverse momenta under Lorentz transformations. By applying once again the example mentioned above and considering the proton beam without emittance (we will refer to it as parallel || beam), we find $p_{\pi_x} \leq 195$ MeV/c. The muon is then emitted and the boost from CM to LAB is along $\underline{\beta}_\pi$, therefore a kind of balance occurs: $(p_{\mu_x})_{rms} \simeq (p_{\pi_x})_{rms}$. This is very relevant in order to generate a low emittance secondary beam: for proton beam spot size at IP $\sigma_0 \leq 10$ μm we can generate pion and muon beams with normalized emittances of a few mm·mrads, as discussed below. As already mentioned the challenge of preserve such a low emittance in the decay of a pion to generate the muon beam is a matter of a future work.

While the emittance is preserved in the decay, the longitudinal component can be strongly altered. In the easiest scenario in which the pion travels along z, considering $\beta_\pi \simeq 1$ and therefore $\gamma_\pi \simeq p_{\pi_z}/M_\pi$ we can write

$$p_{\mu_z} \simeq p_{\pi_z}\frac{E^*_\mu}{M_\pi}\left(1 + \frac{p^*_\mu}{E^*_\mu}\cos\theta^*\right). \tag{6.15}$$

Since from eq. (6.13) we get $p^*_\mu = 29.82$ MeV/c and $E^*_\mu = 109.77$ MeV, the value of the emitted muon longitudinal momentum ranges between $0.572 \cdot p_{\pi_z}$ and p_{π_z}.

One of the advantages of this pion photo-cathode scheme lays in the production of highly relativistic muons that are long lived, in excess of tens of milliseconds, allowing to conceive a complex and multistaged beam manipulation scheme, aimed at preserving the emittance and more in general the $6D$ phase space volume.

We create an event-generator code to simulate the proton-photon beams interaction and we illustrate in the following the results obtained by the $p + h\nu \to \pi^+ + n$ and $\pi^+ \to \mu^+ + \nu_\mu$ reactions for different parameters: $E_p = 7$ TeV and $h\nu = 20$ keV (case LHC), $E_p = 50$ TeV and $h\nu = 3$ keV (case FCC) and $E_p = 400$ GeV and $h\nu = 350$ keV (case SPS).

The photon energy $h\nu$ is chosen in order to maximize the Lorentz invariant total cross section for pion photo-production on protons (as mentioned above $\simeq 220$ μbarn corresponding to $h\nu' = 300$ MeV).

In our simulations the protons are distributed in a circle of 10 μm radius ($\sigma_0 = 7$ μm) and the scattering angle θ in LAB is taken with respect to the mean direction of the proton beam propagation. The FEL photon beam diffraction has been disregarded and we supposed an optimal space-time overlap between the two colliding beams at the IP, i.e. $\sigma_0 = \sigma_{h\nu_x}$.
The minimum and maximum value of the longitudinal momentum, the maximum value of p_x and of θ are reported in Tables 6.1, 6.2 and 6.3 for all the kind of particles involved in the reaction.

Table 6.1: Particles properties (case LHC). Values of momenta in [GeV/c], angles in [μrad].

Particle	p_z^{min} [GeV/c]	p_z^{max} [GeV/c]	p_x^{rms} [GeV/c]	θ^{rms} [μrad]
Proton	$\simeq 7000$	7000	0.187	27
Photon	20 keV	20 keV	0	0
Pion	260	2540	0.38	145
Neutron	4450	6740	0.38	27
Muon	149	2500	0.38	147
Neutrino	0	1080	0.16	≤ 500

Table 6.2: Particles properties (case FCC). Values of momenta in [GeV/c], angles in [μrad].

Particle	p_z^{min} [GeV/c]	p_z^{max} [GeV/c]	p_x^{rms} [GeV/c]	θ^{rms} [μrad]
Proton	$\simeq 50000$	50000	$\parallel beam$	$\parallel beam$
Photon	3 keV	3 keV	0	0
Pion	1722	19108	0.21	11
Neutron	30891	48277	0.21	1.45
Muon	986	19108	0.22	11.5
Neutrino	0	8162	0.1	≤ 500

In graph $a)$ of Fig. 6.3 and 6.7 the angular dependence of the longitudinal component of the pion momentum is shown. The more energetic branch comes from pions co-propagating with the protons in CM (emitted forwards with respect to $\underline{\beta}_{CM}$), the other one from the counter-propagating pions.

The probability of a pion being produced at a certain angle in CM is proportional to the differential cross section [2] corresponding to the values of the incoming proton and

---

[2] See Appendix D for detailed calculations involving differential cross sections.

Table 6.3: Particles properties (case SPS). Values of momenta in [GeV/c], angles in [μrad].

Particle	p_z^{min} [GeV/c]	p_z^{max} [GeV/c]	p_x^{rms} [GeV/c]	θ^{rms} [μrad]
Proton	$\simeq 400$	400	$\parallel$ *beam*	$\parallel$ *beam*
Photon	350 keV	350 keV	0	0
Pion	14.9	145	0.195	1200
Neutron	254	385	0.195	166
Muon	8.5	145	0.2	1300
Neutrino	0	62	0.093	9 mrad

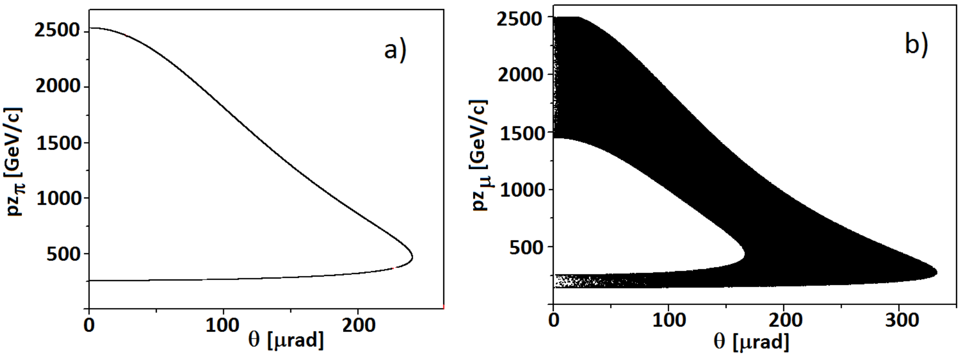

Figure 6.3: Pions and muons longitudinal momentum [GeV/c] as a function of θ [μrad], without transverse emittance of the incoming proton beam (case LHC).

photon. In order to simulate the pion emission angle in CM, the code compares a random number $r \in [0,1)$ with the value of the differential cross section σ (normalized to 1) evaluated in $\tilde{\theta}^* \in [0,\pi)$ (randomly chosen). If $r < \sigma(\tilde{\theta}^*)$ the pion is emitted at $\tilde{\theta}^*$ otherwise the selection is repeated.

The transformation of the angle θ^* in CM to the θ_π in LAB is given by eq. (6.7). If we consider the LHC parameters, we have $\beta^*_\pi = 195.5/240.3 = 0.813$ and $\beta_{CM} = 0.9999999853$: since $\beta_{CM} > \beta^*_\pi$, the denominator of (6.7) is positive for each θ^* ($0 \leq \theta^* \leq \pi$) and consequently $0 \leq \theta_\pi \leq \pi/2$, i.e. the pion in LAB is emitted always forward with respect to the CM direction of propagation. Moreover, since $\theta_\pi = 0$ for both $\theta^* = 0$ and $\theta^* = \pi$, the maximum angle in the LAB corresponds to $\overline{\theta}^*$ such that $d\theta_\pi(\overline{\theta}^*)/d\theta^* = 0$, which is $\overline{\theta}^* = \arccos(-\beta^*/\beta_{CM})$. The dependence of the angle in LAB as a function of the one in CM in the LHC case without and with emittance is plotted in Fig. 6.4.

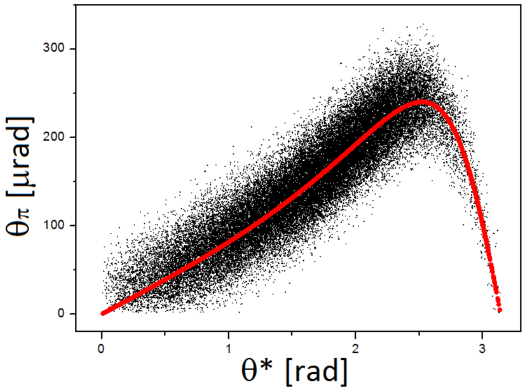

Figure 6.4: Angle in LAB θ_π [μrad] as a function of the angle in CM θ^* [rad], without (red) and with (black) transverse emittance of the incoming proton beam (case LHC).

In the LHC case we also take into account the effect of the proton beam transverse emittance, which spreads the protons transverse momentum in phase space according to equation $\sigma_{p_{p_x}} \equiv M_p\sqrt{\langle \overline{p}^2_{p_x}\rangle} = M_p\epsilon^{p_x}_n/\sigma_0$, where $\sigma_{p_{p_x}}$ is the rms proton beam transverse momentum. The result of this operation is shown for all of the particles in Fig. 6.5: the presence of the proton beam transverse emittance causes an enlargement of the angular spread and a dispersion in momentum both for primary and secondary particles.

Considering $\epsilon^{p_x}_n = 1.4$ mm·mrad as a typical value of LHC proton beams and $\sigma_0 = 7$ μm we find $\sigma_{p_{p_x}} = 187$ MeV/c ($\sigma_{p_{x'}} = 27$ μrad). In Fig. 6.6 is presented the same example as in Fig. 6.1 of the transformation between CM and LAB of the momentum components of a pion and neutron, but this time we take into account the transverse momenta of the incoming proton: the right window shows that p_x is not invariant (the same holds for p_y).

In order to better understand the behavior of the emitted particles we consider some additional examples of colliding beams energies. The data of the simulation of $E_p = 7$

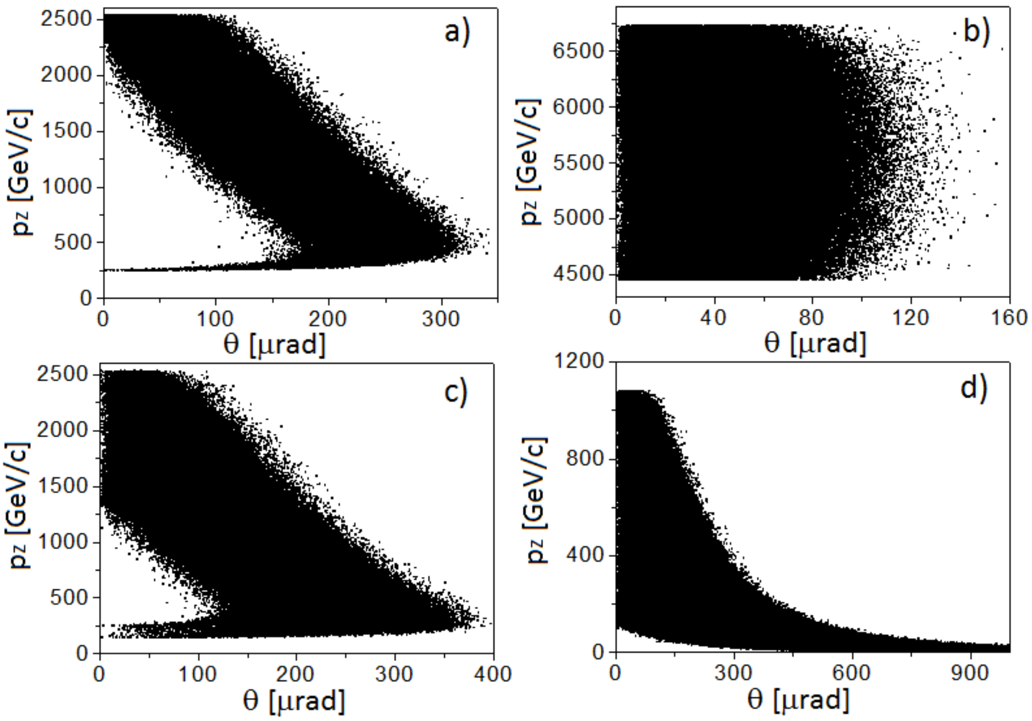

Figure 6.5: Pions a), neutrons b), muons c) and neutrinos d) longitudinal momentum [GeV/c] as a function of θ [μrad] (case LHC).

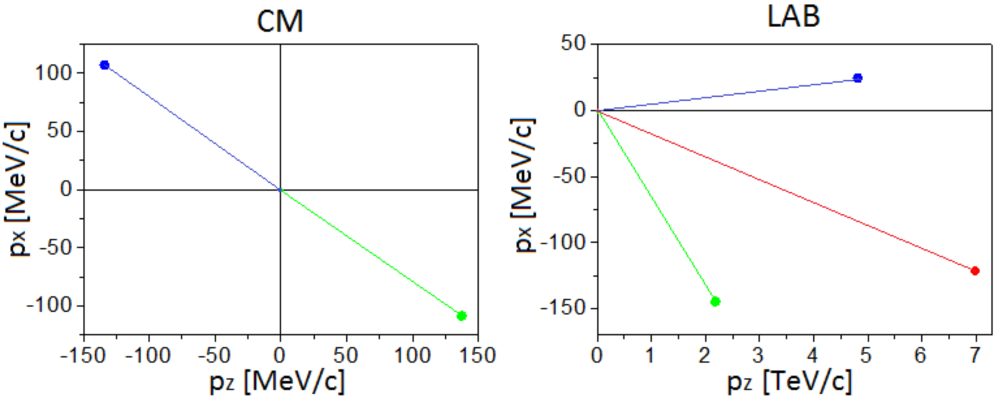

Figure 6.6: Example of a simulated pion-neutron emission: pion (in green) and neutron (in blue) momentum components in CM (left) and transformation to the LAB (right) in the case of $E_p = 7$ TeV with emittance and $h\nu = 20$ keV. The direction of CM is reported in red.

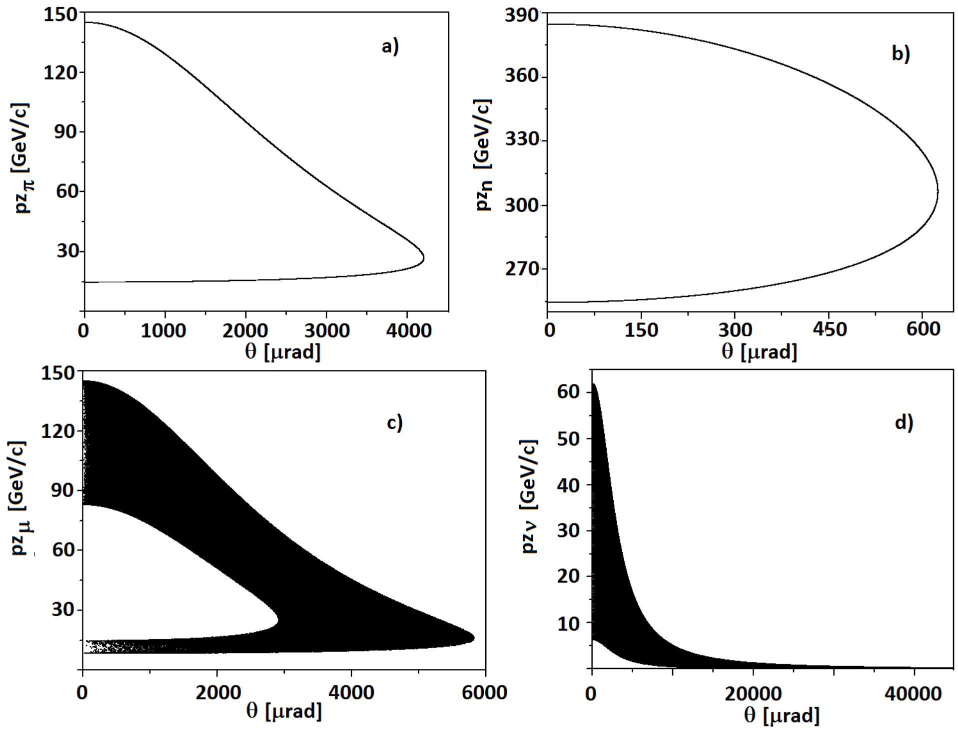

Figure 6.7: Pion, neutron, muon and neutrino longitudinal momentum [GeV/c] as a function of θ [μrad] (case SPS).

TeV and $E_p = 50$ TeV colliding with photons at $h\nu = 12$ keV are reported in Tables 6.4 and 6.5. We can notice that the decrease of $h\nu'$ at constant proton energy leads to an increase of the minimum and to a decrease of the maximum value of p_z for all the particles involved (compare Table 7.2 to 6.4 and 6.2 to 6.5); the minimum and maximum values of p_z coincide at the threshold value of the reaction which is $h\nu' \simeq 150$ MeV. Therefore at threshold we would produce two quasi-monochromatic beams of pions and neutrons, although with a quite low efficiency.

Table 6.4: Particles properties. Values of momenta in [GeV/c], angles in [μrad].

Particle	p_z^{min} [GeV/c]	p_z^{max} [GeV/c]	p_x^{rms} [GeV/c]	θ^{rms} [μrad]
Proton	$\simeq 7000$	7000	$\parallel$ *beam*	$\parallel$ *beam*
Photon	12 keV	12 keV	0	0
Pion	520	1509	0.077	26
Neutron	5490	6479	0.077	3.5
Muon	298	1509	0.095	31
Neutrino	0	644	0.05	≤ 500

Table 6.5: Particles properties. Values of momenta in [GeV/c], angles in [μrad].

Particle	p_z^{min} [GeV/c]	p_z^{max} [GeV/c]	p_x^{rms} [GeV/c]	θ^{rms} [μrad]
Proton	$\simeq 50000$	50000	$\parallel$ *beam*	$\parallel$ *beam*
Photon	12 keV	12 keV	0	0
Pion	407	36431	0.652	36
Neutron	13568	49593	0.652	6.7
Muon	233	36431	0.655	37.6
Neutrino	0	15561	0.281	≤ 500

As a further example we move close to the threshold and we show the transverse phase spaces and the longitudinal momenta as a function of the emission angle of the pions produced by the collision of protons at $E_p = 50$ TeV and photons with $h\nu^{th} = 1.43$ keV respectively without (Fig. 6.8) and with (Fig. 6.9) taking into account the proton beam transverse emittance. In the simulations the photon diffraction is not considered, the proton beam normalized rms transverse momentum is $\sigma_{p_{p_x}} = 1289.75$ MeV/c and the proton rms spot size is $\sigma_0 = 1.6$ μm to give a normalized transverse emittance of $\epsilon_n^{p_x} = \sigma_{p_{p_x}}\sigma_0/M_p = 2.2$ mm·mrad. In both cases the relative energy spread is around 5.3%, the mean value of the longitudinal momentum is 6.49 TeV and the rms is 345 GeV. The transverse emittance values of the pion beams are 0.075 and 1.92 mm·mrad respectively.

As we see in Fig. 6.3, 6.5 and 6.7 at the same angle in the laboratory frame we can find

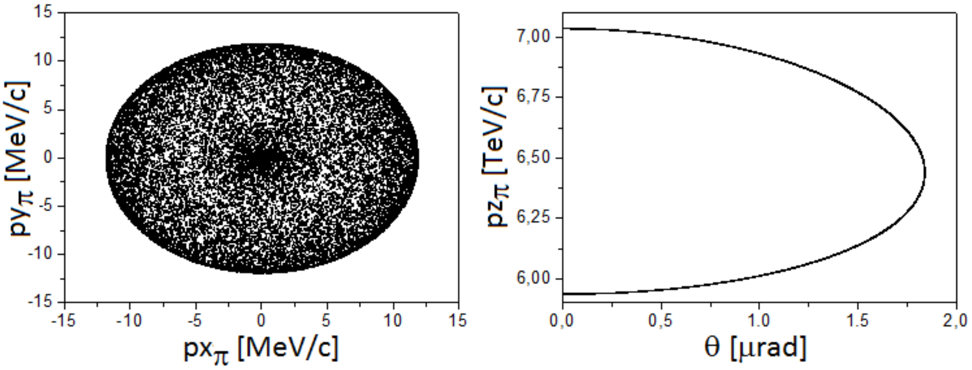

Figure 6.8: Pion beam properties at $E_p = 50$ TeV and $h\nu = 1.43$ keV, without considering the emittance of the incoming proton beam.

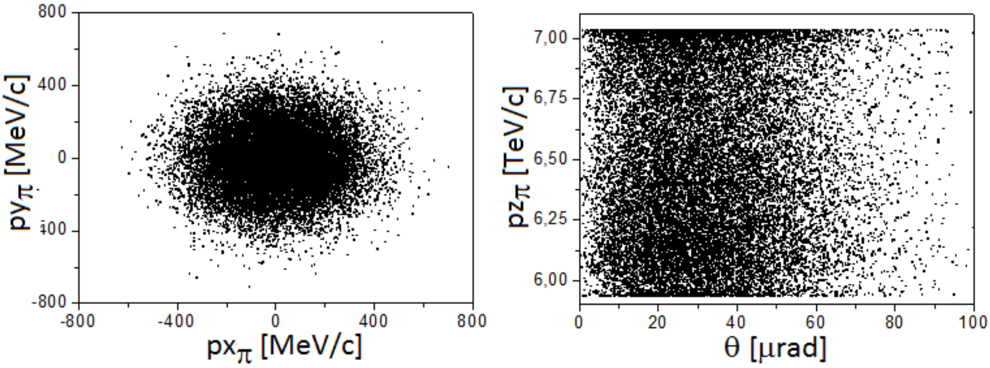

Figure 6.9: Pion beam properties at $E_p = 50$ TeV and $h\nu = 1.43$ keV, considering the emittance of the incoming proton beam.

the same kind of particle at very different energies, therefore if a selection of the particles is needed, it has to be performed in the terms of energy. Up to now we considered the situation in which all the pions decay into muons. In this ideal situation the decay provides some special bands of longitudinal momentum of pions and muons which are almost overlapped, or restricted within a common narrow bandwidth: as shown in Fig. 6.10 those bands turn out to be the less and the more energetic ones, where the mean value of pions and muons longitudinal momentum is almost coincident.

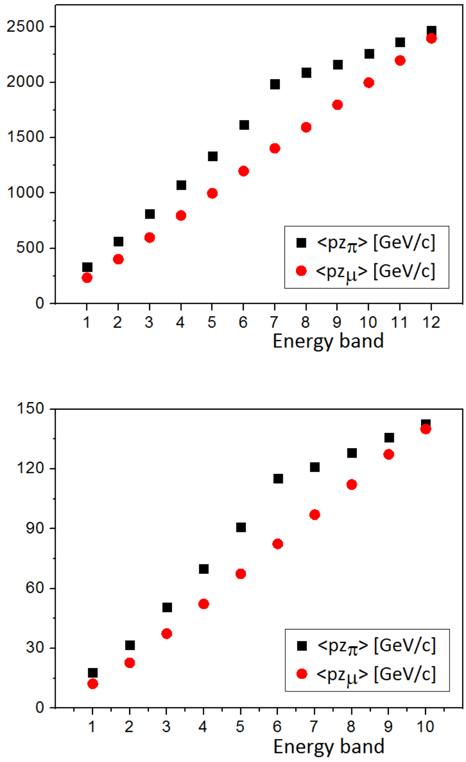

Figure 6.10: Mean value of the longitudinal momentum [GeV/c] of pions (black squares) and muons (red circles) as a function of the muon energy bands for LHC (top) and SPS (bottom) parameters. The energy bands range from the minimum to the maximum value of the muon longitudinal momentum, with a 200 (top) and 15 (bottom) [GeV/c] binning.

In a more realistic scenario, the produced pions have to run in a storage ring for a time sufficient to their decay into muons and in the mean time the produced muons have to remain in the ring, i.e. only the muons produced within the energy acceptance of the ring survive: this turns out to be a very inefficient operation. For example, let us consider the pions produced by the collision of $E_p = 50$ TeV and $h\nu = 2.251$ keV and a ring with the 2% energy spread acceptance. If we divide the pion beam into energy bands such that the energy spread of each one is of 2%, we see (Fig. 6.11 graph a)) that the muon beams obtained by the decay of the pions in the corresponding energy band have a much higher energy spread: many of the muons would get lost. Graph b) shows that the efficiency of the process in terms of muons is at maximum around 1%.

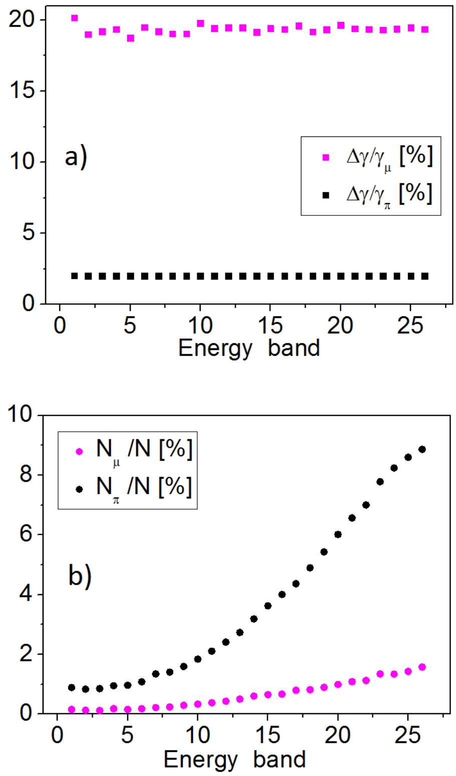

Figure 6.11: Graph a): energy spread [%] of the pions (black) and corresponding muons (magenta) in each energy band. Graph b): percentage of pions (black) and corresponding muons (magenta) within the 2% energy spread for each energy band on the total number of pion produced by the interaction of $E_p = 50$ TeV and $h\nu = 2.251$ keV.

6.2 Direct muon pair production

Let us now consider the direct muon pair production via

$$p + h\nu \to p' + \mu^-\mu^+.$$

As any three body decay, the momentum of the particles is not completely determined by the 4-momentum conservation [3] since we have more variables than equations, i.e. in CM

$$\begin{cases} E_{CM} = E^*_{p'} + E^*_{\mu^-} + E^*_{\mu^+} \\ 0 = \underline{p}^*_{p'} + \underline{p}^*_{\mu^-} + \underline{p}^*_{\mu^+} \end{cases} \tag{6.16}$$

where E_{CM} is the invariant mass of the proton-photon system. This more complicated situation can be studied referring to the two body decay considering the pair as a single particle with invariant mass

$$M_{pair} = \sqrt{(E^*_{\mu^-} + E^*_{\mu^+})^2 - (\underline{p}^*_{\mu^-} + \underline{p}^*_{\mu^+})^2} \tag{6.17}$$

which is not constant but it varies within the limits imposed by the 4-momentum conservation. The energy of the emitted proton in the CM is given by

$$E^*_{p'} = \frac{E^2_{CM} + M^2_p - M^2_{pair}}{2E_{CM}} \tag{6.18}$$

with M_{pair} in the range

$$2M_\mu \leq M_{pair} \leq E_{CM} - M_p \tag{6.19}$$

whose limits correspond to the minimum (proton at rest) and the maximum energy of the emitted proton. The event generator we coded chooses randomly the value M_{pair} in its range (consequently also the emitted proton momentum). The energy available in CM is shared by the emitted proton and the pair, now we have to divide the pair energy into μ^- and μ^+. To this aim we have to define the muons' angles θ^- and θ^+ in CM: one of them is chosen randomly in $[0, \pi)$ and the other is set by the momentum conservation

$$\begin{cases} p^*_{\mu^-} \cos\theta^- + p^*_{\mu^+} \cos\theta^+ = p^*_{p'} \\ p^*_{\mu^-} \sin\theta^- = p^*_{\mu^+} \sin\theta^+ \end{cases} \tag{6.20}$$

and the energy conservation. All of the particles' momenta are defined with respect to each other in CM. By applying a rotation we break the cylindrical symmetry around the z axis given by the generation model and we have in CM a generic output of the reaction, i.e. $(p^*_{p'},\ p^*_{\mu^-},\ p^*_{\mu^+})$. In the ideal case of no emittance proton beam, the transformation to

---

[3] It is monoenergetic only if μ^+ and μ^- have the same energy and therefore the same θ^* with respect to the emitted proton direction in CM (once θ^* is chosen, $p^*_{\mu^+} = p^*_{\mu^-} = p^*_\mu$ is such that $E_{CM} = 2E^*_\mu + E^*_{p'}$ with $\underline{p}^*_{p'} = -2\underline{p}^*_\mu \cos\theta^*$), but in general the output is composed by three particles with different energies.

the laboratory frame is given by

$$\begin{cases} p_{\mu_x^-} = p^*_{\mu_x^-} \\ p_{\mu_y^-} = p^*_{\mu_y^-} \\ p_{\mu_z^-} = \gamma_{CM}\left(\beta_{CM} E^*_{\mu^-} + p^*_{\mu_z^-}\right). \end{cases} \tag{6.21}$$

An example of Lorentz transformation of the momenta of the product particles with boost along the z axis between CM and the laboratory frame is reported in Fig. 6.12. If the emittance of the incident protons is considered, it is necessary to use the Lorentz transformation in the generic direction set by

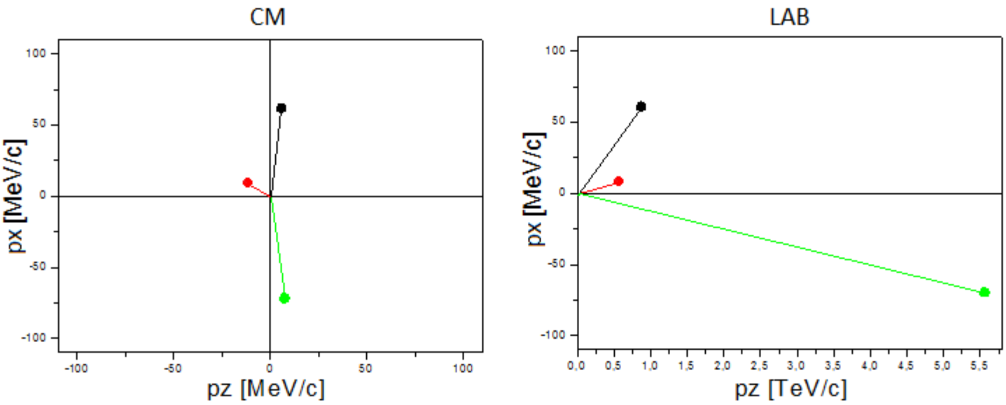

Figure 6.12: Example of a simulated muon pair emission: μ^- (in black), μ^+ (in red) and p' (in green) momentum components in CM (left) and pure longitudinal Lorentz transformation to the LAB (right) in the case of $E_p = 7$ TeV and $h\nu = 20$ keV.

$$\underline{\beta}_{CM} = \left(\frac{p_{p_x}}{E_p + h\nu}, \frac{p_{p_y}}{E_p + h\nu}, \frac{p_{p_z} - h\nu}{E_p + h\nu}\right)$$

where $\underline{p}_p = (p_{px}, p_{py}, p_{pz})$ is the momentum of the incoming proton (see Fig. 6.13) and we do not consider the photon beam diffraction.

The normalized transverse emittance at the interaction point of the μ^- beam is given by $\epsilon^n_{\mu_x^-} = \sigma_0\sqrt{\langle \overline{p}^2_{\mu_x^-}\rangle}/\sqrt{2}$ where σ_0 is the proton beam rms spot size at the interaction point and $\overline{p}_{\mu_x^-} \equiv p_{\mu_x^-}/M_\mu$ is the dimensionless transverse momentum.

We will consider the condition of maximum energy in the CM for the muon pair, corresponding to a steady proton in the CM after collision: this is equivalent to the well known condition of photon energy completely transferred to the muon pair. We are interested in this condition since it will generate an upper limit to the transverse temperature (momentum) of the muon pair beams generated in the collision, therefore allowing

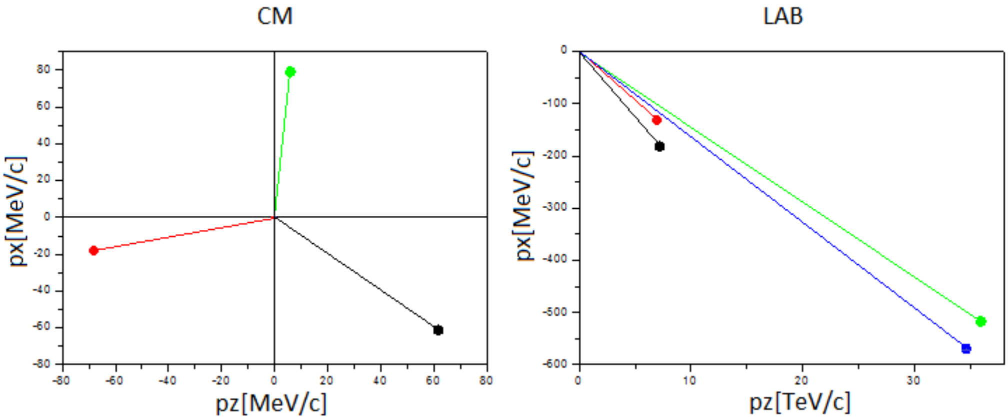

Figure 6.13: Example of a simulated muon pair emission: μ^- (in black), μ^+ (in red) and p' (in green) momentum components in CM (left) and Lorentz transformation to the LAB (right) in the case of $E_p = 50$ TeV with emittance and $h\nu = 5$ keV. The direction of CM is reported in blue.

us to set up an upper limit to the thermal emittance of the muon beams [4].
For a steady proton in the CM after collision we have:

$$\begin{cases} M_\mu \gamma^*_{\mu^-} + M_\mu \gamma^*_{\mu^+} + M_p = E_{CM} \\ \underline{p}^*_{\mu^-} + \underline{p}^*_{\mu^+} = 0 \end{cases} \tag{6.24}$$

so $\gamma^*_{\mu^-} = \gamma^*_{\mu^+} = \gamma^*_\mu$ and $p^*_{\mu^-} = p^*_{\mu^+} = p^*_\mu$, therefore $\gamma^*_\mu = \frac{E_{CM}-M_p}{2M_\mu} = \frac{M_p}{2M_\mu}\left(\sqrt{1+\Delta_p}-1\right)$, which implies

$$p^*_\mu = M_\mu \sqrt{\left[\frac{M_p}{2M_\mu}\left(\sqrt{1+\Delta_p}-1\right)\right]^2 - 1}. \tag{6.25}$$

At threshold, defined by $p^*_\mu = 0$ (steady muon pair), we have $\Delta_p^{th} = \frac{4M_\mu}{M_p}\left(1+\frac{M_\mu}{M_p}\right) = 0.497$ for the minimum proton recoil factor ($E^{th}_{CM} = M_p\sqrt{1+\Delta^{th}_p} = M_p + 2M_\mu$) and

---

[4] In case we consider one muon steady in the CM frame, the CM energy is shared by the other muon in the pair and the proton, such that the conditions hold:

$$\begin{cases} M_\mu \gamma^*_{\mu^+} + M_\mu + M_p \gamma^* = E_{CM} \\ \underline{p}^*_{\mu^+} + \underline{p}^*_p = 0 \end{cases} \tag{6.22}$$

implying $p^*_{\mu^+} = p^*_p$, therefore

$$\gamma^*_{\mu^+} = \frac{\left(M_p\sqrt{1+\Delta_p} - M_\mu\right)^2 + M_p^2 - M_\mu^2}{2M_p\left(M_p\sqrt{1+\Delta_p} - M_\mu\right)} \simeq \frac{1+\frac{\Delta_p}{2}}{\sqrt{1+\Delta_p}} - 0.02 \tag{6.23}$$

which is always smaller at any value of Δ_p than the other case considered above of steady proton, where $\gamma^*_{\mu^-} = \gamma^*_{\mu^+} = \frac{M_p}{2M_\mu}\left(\sqrt{1+\Delta_p}-1\right)$ and γ^*_p =1. Thus confirming that the maximum muon beam emittance (i.e. CM momentum p^*_μ) is given by the case of steady proton in the CM frame, as stated above. When the proton is steady in the CM, the muon pair absorbs the maximum CM energy/momentum, that is converted to maximum emittance and energy spread in the laboratory transverse and longitudinal phase space distributions.

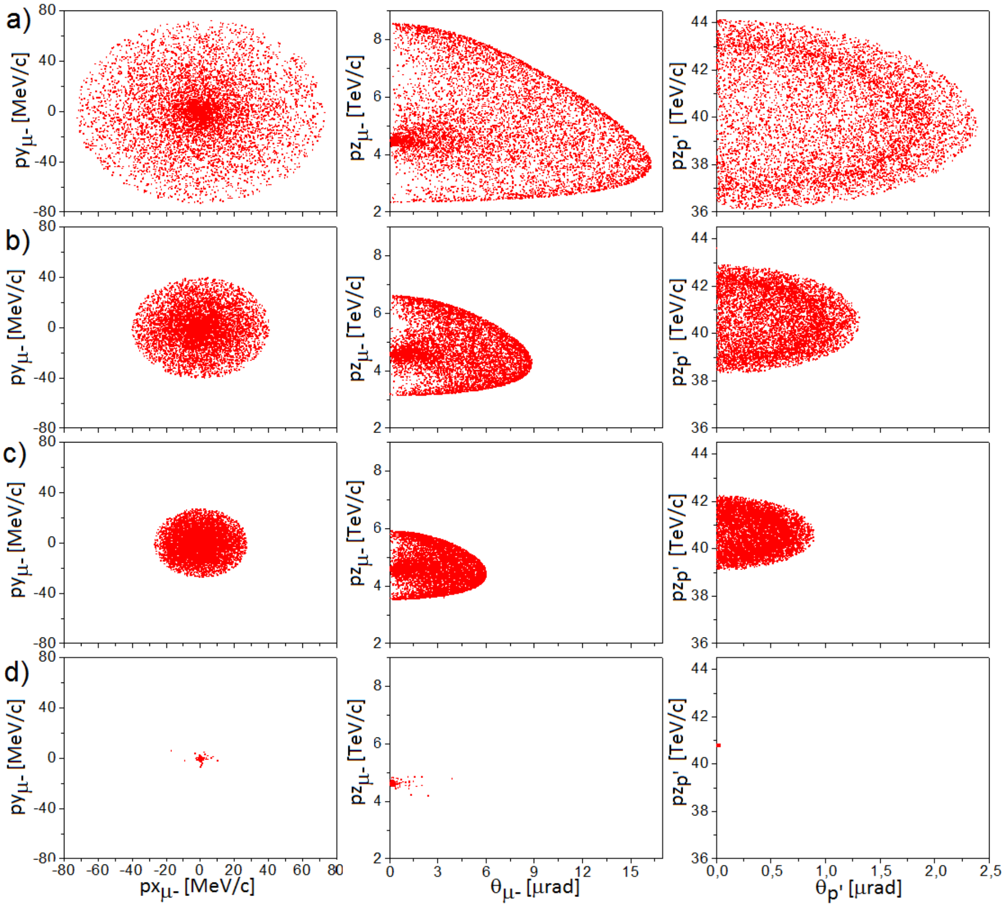

Figure 6.14: Features of the $\mu-$ beam and of the scattered protons p' at different values of the incoming photon energy $h\nu = 2.5$ a), 2.3 b), 2.25 c), 2.2053 d) keV, without considering the emittance of the incoming proton beam at $E_p = 50$ TeV.

$h\nu^{th} = \frac{M_p \Delta_p^{th}}{4\gamma} \simeq 117$ [MeV] $/\gamma$ for the minimum photon energy, equivalent to $h\nu'^{th} =$ 234 MeV seen by the proton (i.e. $h\nu^{th} = 16$ keV for $E_p = 7$ TeV and $h\nu^{th} = 2.2$ keV for $E_p = 50$ TeV). The features of the $\mu-$ beam and of the scattered protons p' at different values of the incoming photon energy $h\nu = 2.5, 2.3, 2.25, 2.2053$ keV, without considering the emittance of the incoming proton beam at $E_p = 50$ TeV are shown in Figs. 6.14 and 6.15.

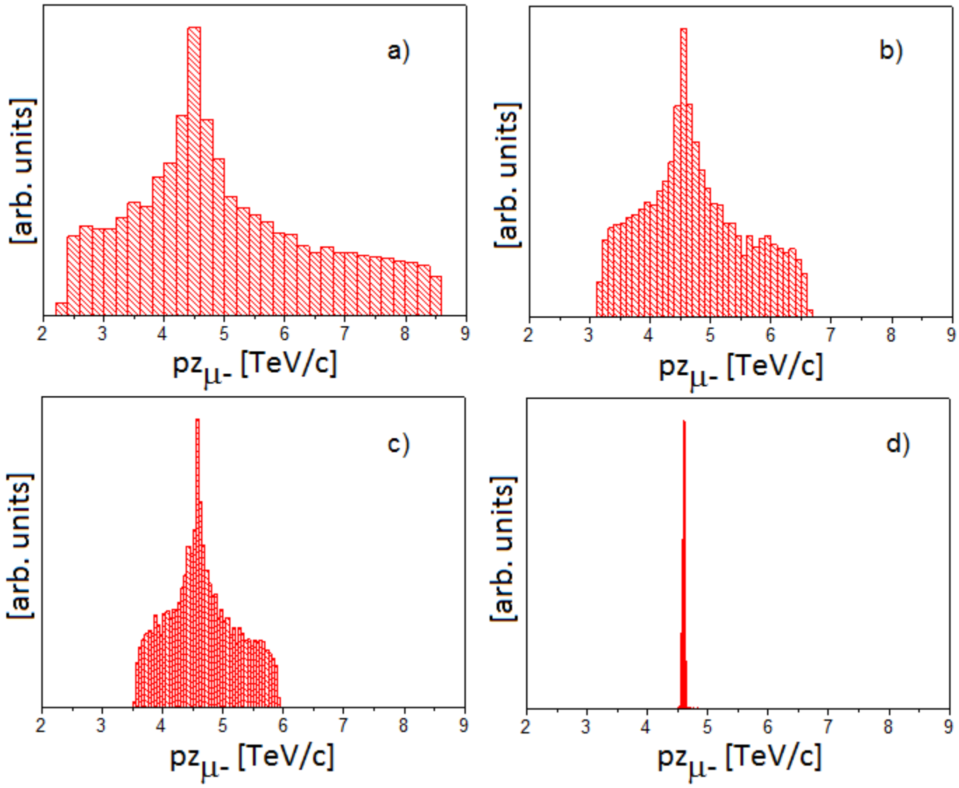

Figure 6.15: Spectra of $\mu-$ at different values of the incoming photon energy $h\nu = 2.5$ a), 2.3 b), 2.25 c), 2.2053 d) keV, without considering the emittance of the incoming proton beam at $E_p = 50$ TeV.

Recalling the evaluation performed above for the case of pion beams, we can derive the thermal normalized emittance of the muon beams, due to the collision transverse temperature (or the excess energy available in the CM above threshold that is converted into stochastic transverse momentum of the muons), as

$$\epsilon^{\mu}_{n-cath} \leq \frac{1}{\sqrt{3}} \frac{\sigma_0}{\sqrt{2}} \sqrt{\frac{M_p^2}{4M_\mu^2}\left(\sqrt{1+\Delta_p}-1\right)^2 - 1} \tag{6.26}$$

where σ_0 is the proton beam spot size at the interaction point (assuming a uniform distribution of momenta in the transverse phase space of the muon beams). At twice the threshold photon energy, i.e. at $\Delta_p = 1$ or $h\nu' = 468$ MeV, we find $\epsilon^{\mu}_{n-cath} = 0.63 \cdot \sigma_0$. As for the pion beam, the total muon beam emittance ϵ^{μ}_{n} is given by the contribution of both the proton beam emittance ϵ^{p}_{n} and the thermal emittance ϵ^{μ}_{n-cath} generated by the equivalent muon photo-cathode effective temperature.

The values of the normalized transverse emittance for the same photon and proton energies reported in Fig. 6.14 are plotted in Fig. 6.16: the emittance in this cases is purely thermal (no proton beam emittance), the value of it approaches zero at the muon threshold production energy and shows a square root growth. The simulated values (magenta dots) are compared to the ones given by Formula (6.26) (black squares): the agreement is very good especially close to the threshold.

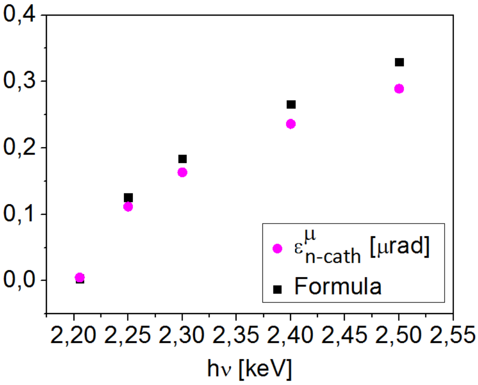

Figure 6.16: Emittance of the μ^- beam ϵ^{μ}_{n-cath} (magenta) and Formula (6.26) (black) in μrad as a function of $h\nu$ in keV, $\sigma_0 = 1.6$ μm and no emittance of the incoming protons.

In Fig. 6.17 the proton beam emittance has been considered. The total transverse normalized emittance (magenta dots) grows instead linearly starting from the emitted proton beam emittance value which is lower than the incoming proton beam one: the very low diffraction considered for the incoming photon beam (we set it null in the simulations) induces a cooling of the proton beam (see Fig. 6.18). Fig. 6.17 shows that $\epsilon_2 < \epsilon^{\mu}_{n-cath} < \epsilon_1$ where $\epsilon_1 = \sqrt{(\epsilon^{\mu}_{n-cath})^2 + (\epsilon^{p'}_{n})^2}$ and $\epsilon_2 = \epsilon^{\mu}_{n-cath} + \epsilon^{p'}_{n}$: the linear sum of the proton and the thermal emittances gives an upper limit, while the quadratic sum sets a lower limit to the total muon beam emittance value.

By transforming the momenta values from the center of mass to the laboratory frame we find a maximum and minimum value for the muon longitudinal momentum given by:

$$\begin{cases} p^{max}_{\mu_z} = \gamma_{CM} \left(\beta_{CM} E^*_{\mu} + p^*_{\mu}\right) \\ p^{min}_{\mu_z} = \gamma_{CM} \left(\beta_{CM} E^*_{\mu} - p^*_{\mu}\right) . \end{cases} \tag{6.27}$$

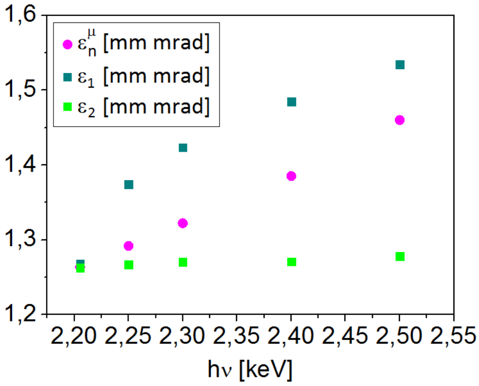

Figure 6.17: Simulated emittance of the μ^- beam as a function of $h\nu$ [keV] in magenta, considering the emittance of the incoming proton beam. $\epsilon_1 = \epsilon^{\mu}_{n-cath} + \epsilon^{p'}_{n}$ (dark cyan) in mm·mrad and $\epsilon_2 = \sqrt{(\epsilon^{\mu}_{n-cath})^2 + (\epsilon^{p'}_{n})^2}$ (green) in mm·mrad vs $h\nu$ [keV].

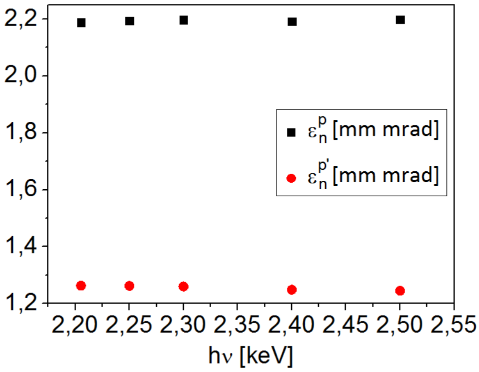

Figure 6.18: Emittance of incoming (black) and scattered (red) proton beams in mm·mrad as a function of $h\nu$ in keV.

At threshold ($p^*_\mu = 0$) $p^{max}_{\mu_z} = p^{min}_{\mu_z} = \gamma_{CM} M_\mu$, therefore $\gamma_{p'} = \gamma_\mu = \gamma_{CM} = \gamma/\sqrt{1+0.497} = 0.82 \cdot \gamma$ ($E^{th}_\mu = 640$ GeV at $E_p = 7$ TeV and $E^{th}_\mu = 4.6$ TeV at $E_p = 50$ TeV). We can evaluate the rms energy spread of the muon beams following the procedure above for pions: we find

$$\frac{\Delta p_{\mu_z}}{\langle p_{\mu_z}\rangle} = \frac{p^{max}_{\mu_z} - p^{min}_{\mu_z}}{2\sqrt{3}\langle p_{\mu_z}\rangle} = \frac{\gamma_{CM} p^*_\mu}{\sqrt{3}\langle p_{\mu_z}\rangle} \tag{6.28}$$

therefore yielding

$$\frac{\Delta\gamma}{\gamma}_\mu = \frac{1}{\sqrt{3}}\sqrt{\frac{M_p^2}{4M_\mu^2}\left(\sqrt{1+\Delta_p}-1\right)^2 - 1}. \tag{6.29}$$

While $\frac{\Delta\gamma}{\gamma}_\mu$ clearly tends to zero at the threshold, it reaches a value $\frac{\Delta\gamma}{\gamma}_\mu = 5\%$ at $\Delta_p = 1.02 \cdot \Delta_p^{th\mu} = 0.51$. The simulated values of the relative energy spread of the $\mu-$ beam are reported in Fig. 6.19 (blue dots) in comparison to the values of the analytical espression (6.29) (black squares).

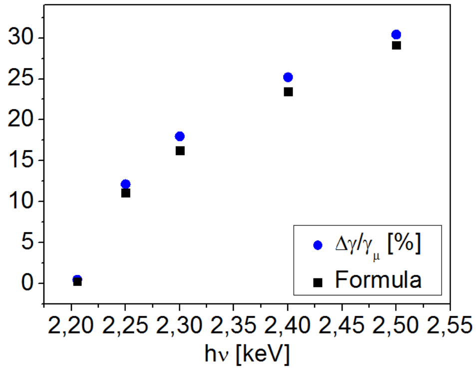

Figure 6.19: Relative energy spread of the $\mu-$ beam [%] (blue) and Formula 6.29 (black) vs photon energy [keV].

The total cross section for the muon pair production is given by the Racah formula [114]: if $k = h\nu'/M_\mu$ is such that $k - 2 \lesssim 1$, i.e. close to muon pair production threshold,

$$\sigma \simeq \alpha Z^2 r_0^2 \frac{2\pi}{3}\left(\frac{k-2}{k}\right)^3\left(1+\frac{\epsilon}{2}\right) \tag{6.30}$$

where $\epsilon = (k-2)/(k+2)$, r_0 is the muon radius calculated as $r_e(M_e/M_\mu) = 2.82 \cdot 10^{-15}(0.511/105.65)$ m, $\alpha = 1/137$ and $Z = 1$. In Fig. 6.20 we plot the value of the total cross section as a function of the incoming photon energy in the case of $E_p = 50$ TeV: even though the characteristics of the emitted muon beam are outstanding especially close to the production threshold, the process is very inefficient [86].

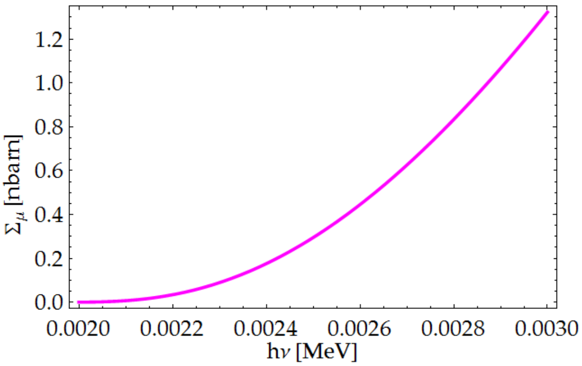

Figure 6.20: Total cross section [nbarn] for the muon pair production as a function of the incoming photon energy [MeV] for $E_p = 50$ TeV.

6.3 Electron-positron pair production

The kinematics of the electron-positron pairs production can be derived by substituting M_μ with M_e in the relationships written above for muon pairs. We find $\Delta_p^{e\ th} = 4M_e/M_p = 0.022$, so that the minimum proton recoil factor at threshold is very small, allowing to make useful approximations at threshold, i.e. $h\nu^{th} \simeq 0.511$ [MeV] $/\gamma$ ($h\nu^{th} = 68$ eV for $E_p = 7$ TeV and $h\nu^{th} = 9.6$ eV for $E_p = 50$ TeV) and $\gamma_{p'} = \gamma_e = \gamma_{CM} = \gamma$. However, in order to generate the muon and anti-muon beams, the hadron-photon collider must be run close and slightly above the muon production threshold, i.e. at $\Delta_p > \Delta_p^{\mu\ th} = 0.497$, which implies a large value for the electron-positron momentum in the CM if $\Delta_p >> \Delta_p^{e\ th}$, that is

$$p_e^* = M_e\sqrt{\left[\frac{M_p}{2M_e}\left(\sqrt{1+\Delta_p}-1\right)\right]^2 - 1} \simeq \frac{M_p}{2}\left(\sqrt{1+\Delta_p}-1\right) \qquad (6.31)$$

giving $p_e^* = \sqrt{M_\mu^2 - M_e^2} \simeq M_\mu$ at the muon production threshold. By transforming to the laboratory we find a maximum longitudinal momentum for the electron or positron in the pair (at energies around the muon production threshold) given by

$$\begin{cases} p_{e_z}^{max} = \dfrac{2\gamma M_\mu}{\sqrt{1+\Delta_p}} \\ p_{e_z}^{min} = -\dfrac{M_\mu\sqrt{1+\Delta_p}}{2\gamma}. \end{cases} \qquad (6.32)$$

The negative sign for the minimum longitudinal momentum means that the electron or the positron in the pair is traveling backward along the propagation axis of the incident photon (see footnote 1), i.e. $p_{e_z}^{min} = -8.7$ keV at $E_p = 7$ TeV and $p_{e_z}^{min} = -1.2$ eV at $E_p = 50$ TeV. Fig. 6.21 shows the transverse phase space and the longitudinal momentum of the emitted electrons at the muon production threshold ($E_p = 50$ TeV and

$h\nu = 2.2053$ keV), the energy spread is almost 100% and the mean p_z is around 4 TeV.

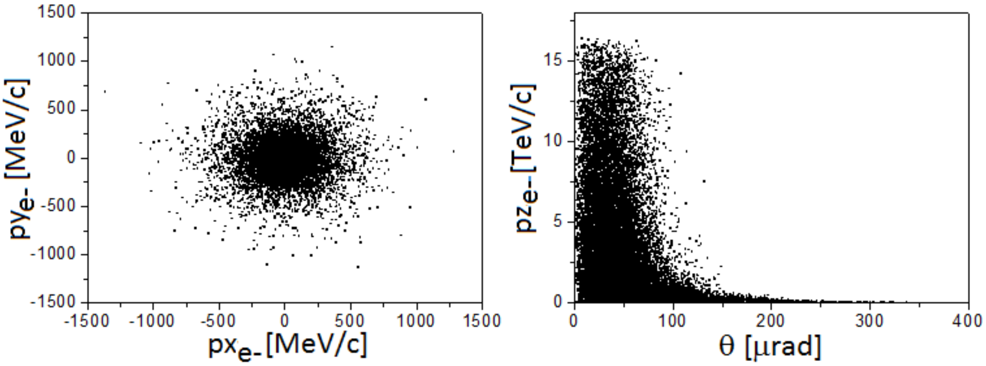

Figure 6.21: Electron-positron pairs properties at $E_p = 50$ TeV and $h\nu = 2.2053$ keV, considering the emittance of the incoming proton beam.

In this case the total cross section is given by the Heitler-Sauter formula

$$\sigma = \alpha Z^2 r_e^2 \left[\frac{28}{9} ln(2k) - \frac{218}{27} \right] \tag{6.33}$$

where $k = h\nu'/M_e$. Fig. 6.22 shows a value around 16 mbarn at the muon pair production threshold where the pion production cross section is around a factor 100 lower and the muon pair cross section is less than a nbarn.

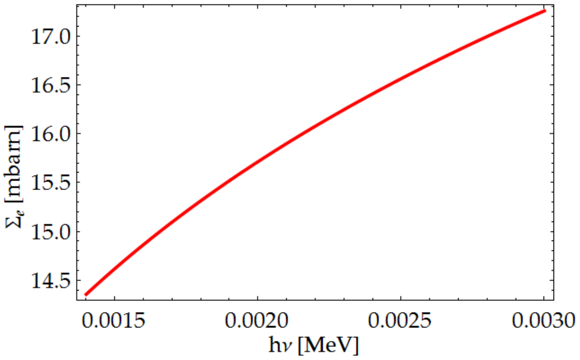

Figure 6.22: Total cross section [mbarn] for the electron-positron pair production as a function of the incoming photon energy [MeV] for $E_p = 50$ TeV.

In order to complete the analysis close to muon pair production threshold we show in Fig. 6.23 and Fig. 6.24 the data concerning the pion production respectively without and with the proton beam emittance. The energy spread is 44%, the mean energy is 8.7 TeV and the transverse emittance 0.89 and 2.95 mm·mrad respectively.

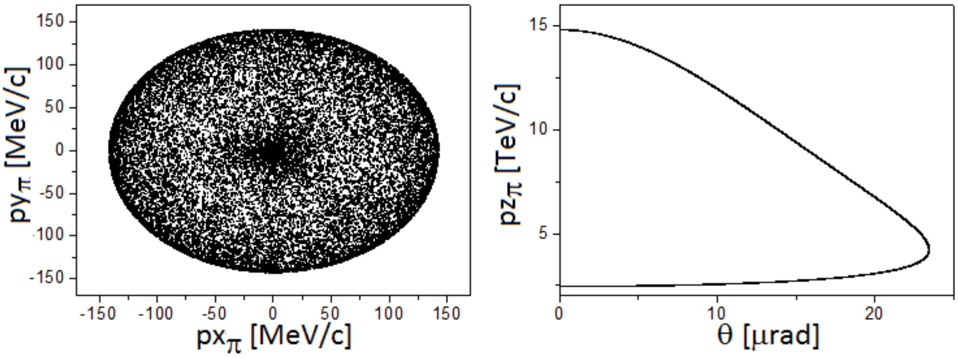

Figure 6.23: π beam properties at $E_p = 50$ TeV and $h\nu = 2.2053$ keV, without considering the emittance of the incoming proton beam.

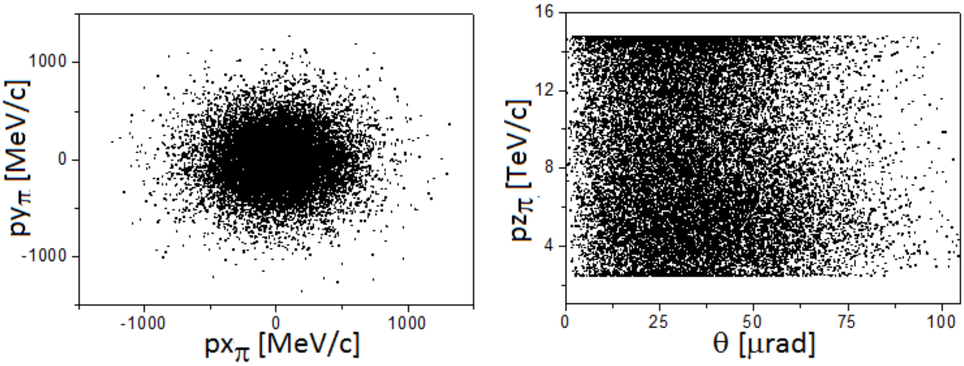

Figure 6.24: π beam properties at $E_p = 50$ TeV and $h\nu = 2.2053$ keV, considering the emittance of the incoming proton beam.

6.4 Inverse Compton scattering off protons

The Inverse Compton scattering of photons by protons is analogous to the one involving photons and electrons (widely treated in Part I of this dissertation) except for the total cross section Σ_p value, which in the proton case is much lower than the Thomson one ($\Sigma_T = 0.67$ barn): $\Sigma_p = \Sigma_T (M_e/M_p)^2$ [63].

In the center of mass frame CM the modulus of the momentum of proton and back-scattered photon, in case of Compton scattering, are:

$$p_p^* = h\nu^* = \frac{E_{CM}^2 - M_p^2}{2E_{CM}} = \frac{\Delta_p M_p}{2\sqrt{1+\Delta_p}} \tag{6.34}$$

showing that there is no threshold for this reaction (as expected, it is a scattering) so that the proton recoil can be arbitrarily small. A Lorentz transformation to the laboratory gives the longitudinal momentum of the scattered photon as a function of the CM scattering angle θ^*:

$$k_z = h\nu^* \gamma_{CM} \left(\beta_{CM} + \cos\theta^*\right) \tag{6.35}$$

which exhibits

$$\begin{cases} k_z^{max} = k_z(\theta^* = 0) = \dfrac{4\gamma^2 h\nu}{1+\Delta_p} \\ k_z^{min} = k_z(\theta^* = \pi) = -h\nu. \end{cases} \tag{6.36}$$

Incidentally, at very small angles in the CM, the corresponding laboratory angle is $\theta = \theta^* \sqrt{1+\Delta_p}/2\gamma$, and the photon momentum at small angles around the proton propagation axis (back-scattering close to the Compton edge) is given by

$$k_z = \frac{4\gamma^2 h\nu}{1+\Delta_p} \left(1 - \frac{\gamma^2\theta^2}{1+\Delta_p}\right) \tag{6.37}$$

as well known from the description of the collimated spectral characteristics of Compton sources, that are typically operated with relativistic electrons in very small recoil regime as specified by $\Delta_{e^-} \equiv 4\gamma_{e^-} h\nu / M_{e^-} << 1$.

At the reaction threshold for pion production, the Compton back-scattered photons have maximum energy $E_\gamma^C = h\nu_z^{max} = \gamma M_p \Delta_p^{th}/(1+\Delta_p^{th}) = 0.24 \cdot E_p$ (i.e. $E_\gamma^C = 1.68$ TeV for $E_p = 7$ TeV and $E_\gamma^C = 12$ TeV for $E_p = 50$ TeV).

CHAPTER 7

Luminosity and flux considerations

At each collision, the number of a certain kind of particle produced can be calculated as

$$\mathcal{N} = \mathcal{L} \cdot \Sigma \tag{7.1}$$

where Σ is the total cross section for the considered reaction and $\mathcal{L}$ is the proton-photon collider luminosity given by

$$\mathcal{L} = \frac{N_p N_{ph} r}{4\pi\sigma_0^2} \tag{7.2}$$

where N_p is the number of colliding protons in the bunch, N_{ph} is the number of photons carried by the radiation pulse, r the repetition rate of the collisions and σ_0 the effective spot size at the IP. Since the interaction does not produce beam-beam effects, due to the nature of the photon pulse and since the collective effect due to the electromagnetic field of the XFEL photon beam are very small (the equivalent laser parameter representing the dimensionless value of its electromagnetic vector potential as seen by the proton $a_0 \propto 10^{-4}(M_e/M_p)\lambda_{FEL}[\text{Å}]\sqrt{P[TW]}/\sigma_{h\nu_x}[\mu m]$ is much smaller than 1), we can assume that the geometrical luminosity considered in eq. (7.2) is a good assumption as far as the hour-glass effects are negligible. This is certainly the case for an optimized LHC or FCC beam at the IP (with a minimum beta function of about 0.1 m, matched to the proton bunch length to mitigate the hour-glass effect), and it is even more valid for the XFEL beam, since its geometrical emittance is much smaller than the proton beam one ($\epsilon^{p_x} = \epsilon_n^{p_x}/\gamma = 2 \cdot 10^{-10}$ mrad for the proton beam at 7 TeV and $\epsilon^{h\nu_x} = \lambda_{FEL}/4\pi = 8 \cdot 10^{-12}$ mrad for the XFEL photon beam). We should also remark that the FEL photon pulse is extremely short ($\simeq$ 200 fs) compared to the proton bunch, with a diffraction Rayleigh range $Z_R = \pi w_0^2/\lambda_{FEL}$ longer the 1 m: hour-glass effects are therefore depending only on the proton beam diffraction at IP.

Concerning the maximum repetition rate achievable in collisions, LHC can be operated up to 40 MHz and FCC is expected to match it, while XFEL based on SC CW Linacs are aimed at achieving 1 MHz (LCLS-II [103]), but the upgrade to 10 MHz is considered feasible by adopting Energy Recovery Linacs (ERL) schemes, which are definitely much more expensive and challenging but performant in terms of electron beam average current (for our case we would need an average current of about 0.2 nC $\times$ 10 MHz $= 2$ mA, which is certainly in the range of capability of an ERL).

Eventually, considering ultimate performances for either LHC/FCC beams and XFELs beams, we adopt the values reported in Table 7.1 and $r = 10$ MHz for the evaluation of fluxes and proton beam life-time due to event production.

Table 7.1: Collider performances in various scenarios.

PR source	E_p	N_{pr}	σ_0	PH source	$h\nu$	N_{ph}
LHC	7 TeV	$2 \cdot 10^{11}$	7 μm	LCLS-XFEL	20 keV	10^{13}
FCC	50 TeV	10^{11}	1.6 μm	LCLS-II	3 keV	10^{14}
SPS	400 GeV	$2 \cdot 10^{12}$	18 μm	SPARC-LAB	350 keV	10^{8-9}

So, for example, if we consider the FCC parameters we obtain $\mathcal{L} = 3.1 \cdot 10^{38}$ cm^{-2}s^{-1}. Therefore the total number of pions $\mathcal{N}_\pi$ produced per bunch crossing is about $6.5 \cdot 10^3$ assuming a maximum of the total cross section Σ_π of about 220 μbarn ($6.5 \cdot 10^{10}$ pions per second average flux).

There are small differences in the total cross section for the following reactions:

$$p + h\nu \rightarrow \pi^+ + n \qquad p + h\nu \rightarrow \pi^0 + p \tag{7.3}$$

so we should expect an almost equivalent production of charged and neutral pions. These latter are not of interest for a muon collider application since they decay very rapidly (mean life-time $8.4 \cdot 10^{-17}$ s) into a pair of high energy γ photons.
Clearly for a muon-antimuon collider one needs to find other reactions to produce negative pions π^- (e. g. $p + h\nu \rightarrow p' + \pi^+ + \pi^-$).

Under the assumption of preservation of the outstanding pion beam emittance, and considering the long life-times of muons at the TeV level (in excess of tens of milliseconds), one can conceive a storage ring accumulating muons, in order to go from the small number of pions produced at each bunch crossing (about 10^4) up to the requested muons per bunch typical of a muon collider. Assuming this latter value and a life-time of 20 ms for the muons (see Fig. 7.1 and 7.2) we would accumulate 10^9 muons during half of their life-time, which in turns is enough to achieve an effective muon collider luminosity of about 10^{31} s^{-1}cm^{-2} at a few μm IP spot size, interleaving in time accumulation and collision of the muon bunches at each muon half life-time. As shown in Fig. 7.1 and 7.2 the concentration of muons has a maximum at low energy and a secondary peak at a mean energy in both LHC and SPS cases.

There are other reactions possible in the collision between the XFEL photons and the relativistic proton beam, namely the Compton back-scattering of the photons by the proton, the electron/positron pair production in the nuclear field of the proton and the direct muon pair photo-production (so called Bethe-Heitler lepton-pair production process, $p + h\nu \rightarrow p' + e^+e^-$, $p + h\nu \rightarrow p' + \mu^+\mu^-$).

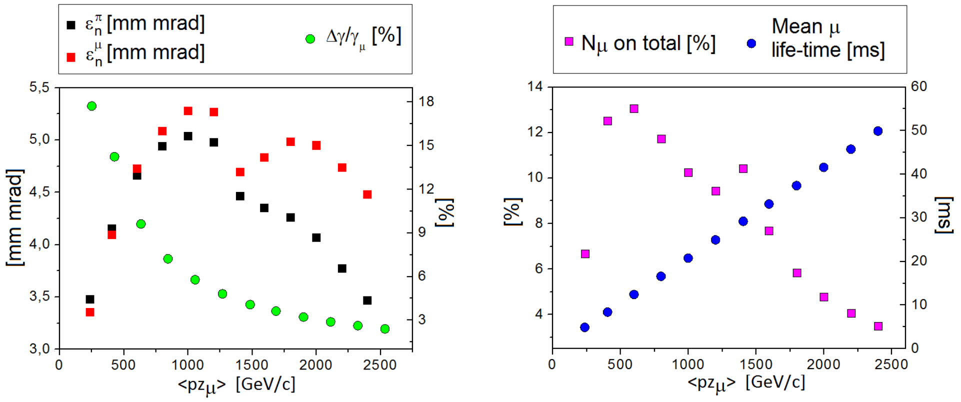

Figure 7.1: Muons properties (case LHC): muon normalized emittance [mm·mrad] in red, pion normalized emittance [mm·mrad] in black, relative longitudinal momentum spread [%] in green, relative number of muon on total [%] in magenta and muon mean life-time [ms] in blue as a function of the mean longitudinal momentum of the muons [GeV/c].

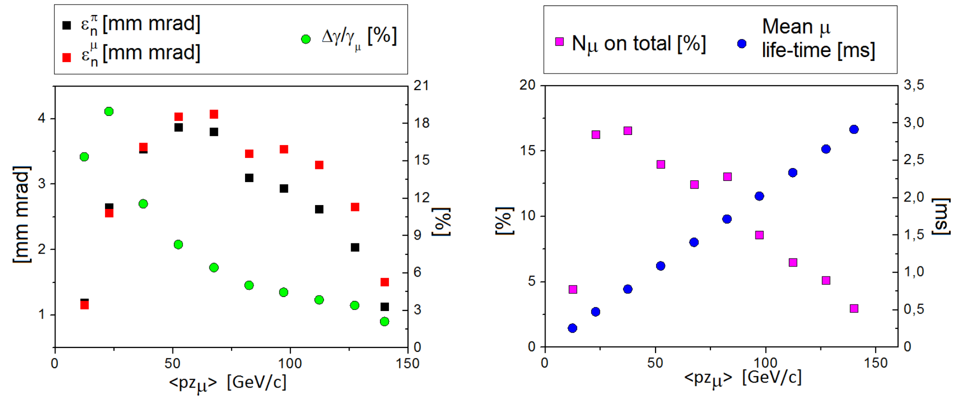

Figure 7.2: Muons properties (case SPS): muon normalized emittance [mm·mrad] in red, pion normalized emittance [mm·mrad] in black, relative longitudinal momentum spread [%] in green, relative number of muon on total [%] in magenta and muon mean life-time [ms] in blue as a function of the mean longitudinal momentum of the muons [GeV/c].

The Compton back-scattering is characterized by a total cross section scaling like $\Sigma_T (M_e/M_p)^2$, so it lays in the range of a fraction of μbarn, quite negligible both for secondary beam generation and for the budget of events setting the life-time of the proton beam (Σ_T is the Thomson cross section, about 0.67 barn [63]).

The electron/positron pair production in the field of the nucleon is instead the dominant process in the collision proton-photon, since its total cross section $\Sigma_{e^+e^-}$ in the range of a few hundreds MeV photons (in the rest frame of the nucleon) is about 15 mbarn (see [112, 114]). So we expect a number of electron/positron pair created at any bunch crossing of the order of 10^6. As discussed in the previous chapter, these pairs are propagating as an intense collimated secondary beam along with the pion beam.

The direct photo-production of muon pairs in the nucleon field by the FEL photon is on the other side characterized by a very small total cross section, which indeed scales like $\Sigma_{e^+e^-} (M_e/M_\mu)^2$, so it is smaller than a μbarn [86], therefore yielding about 10^5 muon pairs per second at 10 MHz repetition rate.

Considering the FCC luminosity $\mathcal{L} = 3.1 \cdot 10^{38}$ cm^{-2}s^{-1} and taking into account the total cross sections given in [107] for the pions and in formulas (6.30) and (6.33) for μ^-/μ^+ and e^-/e^+ pairs, we find the number of events per second specified in Table 7.2.

Table 7.2: Number of particles [s^{-1}] at $E_p = 50$ TeV and $h\nu$ [keV] values reported in table.

E_p [TeV]	$h\nu$ [keV]	$\mathcal{N}_\pi$ [s^{-1}]	$\mathcal{N}_{\mu^-/\mu^+}$ [s^{-1}]	$\mathcal{N}_{e^-/e^+}$ [s^{-1}]
50	$1.43\ (\pi^{th})$	$1.86 \cdot 10^{10}$	0	$4.5 \cdot 10^{12}$
50	$2.2053\ (\mu^-/\mu^{+^{th}})$	$3.72 \cdot 10^{10}$	$1.25 \cdot 10^4$	$5 \cdot 10^{12}$
50	2.5	$4.65 \cdot 10^{10}$	$9.3 \cdot 10^4$	$5.1 \cdot 10^{12}$
50	3	$6.5 \cdot 10^{10}$	$4 \cdot 10^5$	$5.4 \cdot 10^{12}$

The proton beam life-time can be evaluated just rescaling LHC data (beam life-time of about 40 hours) for $p-p$ events, which are characterized by a total cross section of about 110 mbarn and a luminosity (present operation) of 10^{34} s^{-1}cm^{-2}: running the proton-photon collider at a luminosity of 10^{38} s^{-1}cm^{-2} we would get, at a dominant cross section of 15 mbarn, a beam life-time of the order of a second, which sets up a serious challenge to the injection chain of the main ring.

We did not evaluate the cascaded interaction of the electron/positron pair with the counter-propagating FEL colliding photon beam and we did not carried out the generation of its corresponding phase space distributions. This cascaded interaction is indeed possible due to the highly collimated behavior of secondary beams in this highly Lorentz boosted interaction, unlike $p-p$ interactions at LHC IP which occur with a steady CM reference frame. Since part of the $5 \cdot 10^5$ electron/positron pairs will propagate after being generated along with the surviving proton beam, they may collide with a fraction of the incoming 10^{14} FEL photons giving rise to muon pair production via the reactions

$$e^- + h\nu \to e^- + \mu^+\mu^- \qquad e^+ + h\nu \to e^+ + \mu^+\mu^- \tag{7.4}$$

As a rough evaluation of the total number of muon pairs produced per bunch crossing we take as an example 2 TeV electrons or positrons created in the proton-photon collision ($\simeq 5 \cdot 10^5$ per bunch crossing), and we consider their cascaded collision with FEL photons at 12 keV. The energy available in the center of mass is about 309 MeV, well above the threshold of $2M_\mu$. Following Ref. [114] we use a total cross section for the muon pair photo-production of about 1.3 nbarn, which gives an upper limit for the muon pairs produced of about 2 per second (although collimated within an incredibly small forward angle of about 0.3 μrad). Just as a side comment we notice that the direct muon pair photo-production in our primary proton-photon collision via Bethe-Heitler process can give a flux of about a few 10^5 muon pairs per second as discussed above in this section.

Conclusions

Part I

The ELI-NP Gamma Beam System aims at delivering γ beams with unprecedented characteristics in terms of energy tunability, monochromaticity, spectral density, brilliance and polarization. The energy of the emitted beams, ranging between 0.2 and 19.5 MeV, will enable advanced experiments in nuclear physics and nuclear photonics, in material science and many other fields.

The ELI-NP-GBS operates at the transition between the classical and the quantum regimes: since the required bandwidth is very narrow the quantum effects cannot be neglected. In the dissertation we recall the quantum theory of inverse Compton scattering following the approach [60] used also by the developer [61] of the Monte Carlo code CAIN [62]. Mainly through this code we simulate the emitted photon beams' characteristics. The other codes are briefly mentioned together with the theoretical underlying approaches [58,59]. We can have a very precise picture of the emitted photon beam qualities and we are able to compare the results obtained with different methods.

We run the code CAIN in the linear regime since, as described in [66,71], in the ELI-NP parameters range the non-linear effects do not affect the bandwidth value of the collimated beam and the energy peak red-shift value due to this effect can be neglected.

The polarization of the emitted photons has been studied in details (see also [64]). In the ELI-NP case, the collimated beam retains the laser polarization (even with unpolarized electron beam), therefore the linear polarization is higher than 98%.

The impact of the possible jitters and errors of the machine on the γ beam quality is presently under study (some examples are reported in Chapter 4). In particular, the safety region for the spatial misalignments has been determined: the transverse space misalignment bewteen the electron and laser beams at IP cannot exceed 20 μm while the longitudinal one 500 μm; the collimation system transverse space misalignment value has to be lower than 200 μm for the low energy line and 100 μm for the high energy one. The sensitivity on the angular displacement of the electron beam is much higher than the one on the laser pulse: a 50 μrad displacement of the electrons is critical while even tens of mrad angular error of the laser can be accepted.
Other errors and jitters have to be considered on sets of simulated electron and laser beams: this step will be very important in the installation and optimization phase of the Linac [48], the laser [46,47] and the collimation [45] systems.

The ELI-NP-GBS is under construction: the bunker and the infrastructures are about to be completed and the machine installation will start in 2016. The full operation is foreseen by the end of 2018.

Part II

The combination of two most advanced accelerators, the Large Hadron Collider and the X-ray Free Electron Laser, although not easy nor inexpensive to be implemented in reality, offers the great opportunity of conceiving a hybrid Hadron-Photon Collider (HPC), at an unprecedented luminosity exceeding 10^{38} $\mathrm{s}^{-1}\mathrm{cm}^{-2}$. The HPC is actually aimed not at producing events to study, but to generate secondary beams of unique characteristics, via a highly boosted Lorentz frame corresponding to a very relativistic moving center of mass reference frame. The opportunity may become quite strategic in the frame of a new machine under design and being proposed like Future Circular Collider, since the higher energy foreseen (100 TeV) greatly simplifies the type of X-ray FEL machine that should be coupled for implementing a HPC: in fact at FCC the optimal FEL photon energy is about 3 keV ($\lambda_{FEL} = 0.4$ nm), easily achievable by a CW SC GeV-class Linac driving the FEL radiator.

As shown in Chapter 7, the phase space distributions of the secondary beam generated, in particular pions, have outstanding properties of low transverse emittance (in the range $3 - 5.5$ mm·mrad) and are collimated within very narrow forward angles (less than 150 μrad for a 7 TeV colliding proton beam as for LHC and less 10 μrad for a 50 TeV proton beam as for FCC) with energies attaining 2.5 TeV and 19.1 TeV respectively for the two cases (LHC and FCC).

The opportunity consists in conceiving a beam manipulation of charged pions of both signs, generated in the HPC, capable to let them decay into muons and neutrino beams of similar characteristics in the phase space: the challenge is the large energy spread of the pion beams (an energy selection will have to be implemented first) and the long range distance travelled by them before decay, at this energy. The potentialities in terms of muon and neutrino beams obtainable are impressive: although the number of muons and neutrinos per bunch would be low (a few thousands) their phase space distributions would be extremely high quality thanks to the large Lorentz boost of the primary proton-photon collision, giving rise to very small divergence angles for these beams (tens of μrads for muons and hundreds of μrads for neutrinos).
Another possible way to obtain muon beams is the direct muon pair production: despite the very low cross section value, the critical steps represented by the production of charged pions of both signs and the storage and selection of the pions would be overcome. Moreover, a possibility to partially compensate for the low efficiency of the process would be to collide lead ions. The kinematics is the same as the direct muon pair production on protons and the cross section would increase by a factor $Z^2 = 82^2$. Considering that the lead ion intensity is foreseen to be ~ 10 times lower than for protons, there would be a factor ~ 670 gain on the number of produced muons, around 10^8 muon pairs per second.

In both scenarios, the long life of the high energy generated muons (in excess of 10 ms) may offer the opportunity to accumulate them in a storage ring so to achieve muon collider requested bunch intensities.

Appendices

APPENDIX A

Inverse Compton cross section revisited

We present a rigorous method to obtain the inverse Compton cross section in the general case of not null initial momentum of the electrons from a pure QED calculation, avoiding the usual approaches based on the derivation of this cross section either from the Klein and Nishina formula and the Lorentz transformations or through Dyson-Feynman diagrams and Mandelstam invariants.

A.1 Preliminary definitions

We recall here some preliminary definitions and notations usefull in the following calculation, for a more detailed treatise see Ref. [69].
Concerning the electrons we introduce the field operator

$$\hat{\Psi}_\sigma(x) = \sqrt{m_e c}\sum_{r=1}^{2}\int \frac{d^3p}{p^0}\left(\frac{e^{-\frac{i}{\hbar}p\cdot x}}{(2\pi\hbar)^{\frac{3}{2}}}v^r_\sigma(\vec{p})\hat{b}^r(\vec{p}) + \frac{e^{\frac{i}{\hbar}p\cdot x}}{(2\pi\hbar)^{\frac{3}{2}}}w^r_\sigma(\vec{p})\hat{d}^{r\dagger}(\vec{p})\right) \tag{A.1.1}$$

where $\hat{b}^r(\vec{p})$ and $\hat{d}^{r\dagger}(\vec{p})$ are respectively the annihilation operator for particles and the creation operator for the antiparticles [1], satisfying the Dirac equations

$$\left(i\sum_\mu \gamma^\mu \frac{\partial}{\partial x^\mu} - \frac{m_e c}{\hbar}\right)\hat{\Psi}_\sigma(x) = 0 \Leftrightarrow p\cdot p = m_e^2c^2 \tag{A.1.2}$$

$$\frac{1}{2}(\gamma^\nu\gamma^\mu + \gamma^\mu\gamma^\nu) = g^{\mu\nu}I \qquad \text{where} \qquad \gamma^0 = \begin{pmatrix} I & 0 \\ 0 & -I \end{pmatrix} \qquad\qquad \gamma^i = \begin{pmatrix} 0 & \sigma^i \\ -\sigma^i & 0 \end{pmatrix}$$

and the adjoint field operator $\hat{\overline{\Psi}}_\sigma(x) = \hat{\Psi}^\dagger(x)\gamma^0$. The operator acting on the photons is the potential vector

$$\hat{A}^\mu(x) = \hbar\frac{\sqrt{c}}{\sqrt{2}}\int \frac{d^3p}{p^0}\left(\frac{e^{-\frac{i}{\hbar}p\cdot x}}{(2\pi\hbar)^{\frac{3}{2}}}\sum_{\lambda=0}^{3}e^\mu_\lambda(\vec{p})g^{\lambda\nu}\hat{c}_\nu(\vec{p}) + \frac{e^{\frac{i}{\hbar}p\cdot x}}{(2\pi\hbar)^{\frac{3}{2}}}\sum_{\lambda=0}^{3}e^\mu_\lambda(\vec{p})g^{\lambda\nu}\hat{c}^\dagger_\nu(\vec{p})\right) \tag{A.1.3}$$

---

[1] For these operators anticommutators are null for all cases except

$$\left[\hat{b}^r(\vec{p}), \hat{b}^{r'\dagger}(\vec{p'})\right]_+ = p^0\delta_{rr'}\delta_3(\vec{p}-\vec{p'}) \qquad\qquad \left[\hat{d}^r(\vec{p}), \hat{d}^{r'\dagger}(\vec{p'})\right]_+ = p^0\delta_{rr'}\delta_3(\vec{p}-\vec{p'})$$

with $\hat{c}_\nu(\vec{p})$ and $\hat{c}^\dagger_\nu(\vec{p})$ the annihilation and the creation operator respectively [2] and $g^{\mu\nu}\frac{\partial^2}{\partial x^\mu \partial x^\nu}\hat{A}^\mu(x) = 0$. The physical states are characterized by photons having $\lambda = 1, 2$, the one with transverse polarization, i.e. the states $|f\rangle$ and $|g\rangle$ solutions of

$$\langle g|\frac{\partial \hat{A}^\mu(x)}{\partial x^\mu}|f\rangle = 0.$$

Quantum Electrodynamics describes the time evolution of the system constituted by an electron and a photon colliding at a certain instant non exactly localized in a macroscopic time interval $[t_1, t_2]$:

$$|\Psi^{inter}_{t_2}\rangle = \hat{U}^{inter}(t_2, t_1)|\Psi^{inter}_{t_1}\rangle \tag{A.1.4}$$

where

$$\hat{U}^{inter}(t_2, t_1) = e^{\frac{i}{\hbar}\hat{H}_0 t_2} e^{-\frac{i}{\hbar}\hat{H}(t_2 - t_1)} e^{-\frac{i}{\hbar}\hat{H}_0 t_1}. \tag{A.1.5}$$

The Hamiltonian is

$$\hat{H} = \hat{H}_0 + \hat{H}^{inter}_1 \qquad \text{with} \qquad \hat{H}^{inter}_1 = e\int d^3x : \hat{\overline{\Psi}}(x)\gamma^\mu\hat{\Psi}(x)\hat{A}_\mu(x) : \tag{A.1.6}$$

and, being T the chronological ordering operator, the interaction operator has the form

$$\hat{U}^{inter}(t, t_1) = T\left(e^{-\frac{i}{\hbar}\int_{t_1}^{t} dt' \int_{\mathbb{R}^3} d^3x' e : \hat{\overline{\Psi}}(x')\gamma^\mu\hat{\Psi}(x')\hat{A}_\mu(x') :}\right). \tag{A.1.7}$$

A.2 Calculation

The electron-photon system is described by an appropriate mixture of the initial states

$$|\Psi_{t_1}\rangle = \iint \frac{d^3q'}{q'^0}\frac{d^3k'}{k'^0} e^{\frac{i}{\hbar}(q'^0 + k'^0)ct_1} \sum_{r'\lambda'=1}^{2} \Psi_{1e}(q', r')\Psi_{1\gamma}(k', \lambda')\hat{b}^{r'\dagger}(q')\hat{c}^{\lambda'\dagger}(k')|0\rangle \tag{A.2.1}$$

with the wave functions peaked respectively at ($\vec{q_i}$ and $\vec{k_i}$) and displaced inside the beams. We are interested in the transition from $(\vec{q_i}, \vec{k_i})$ at t_1 to $(\vec{q_f}, \vec{k_f})$ at the final time t_2 such that $\Psi_{1e}(q_f, r) = 0$, $\Psi_{1\gamma}(k_f, \lambda) = 0$, i.e. not belonging to the initial state. The statistics of these events is obtained by using

$$\hat{E}^{r\lambda}(M) = \iint_M \frac{d^3q}{q^0}\frac{d^3k}{k^0}\hat{b}^{r\dagger}(\vec{q})\hat{c}^\dagger_\lambda(\vec{k})|0\rangle\langle 0|\hat{c}_\lambda(\vec{k})\hat{b}^r(\vec{q}) \tag{A.2.2}$$

normalized in the sense that

$$\sum_{r\lambda}\hat{E}^{r\lambda}(\mathbb{R}^6) = \hat{P}_{e,\gamma} \tag{A.2.3}$$

---

[2] For these operators commutators are null for all cases except

$$\left[\hat{c}_0(\vec{p}), \hat{c}^\dagger_0(\vec{p'})\right]_- = -p^0\delta_3(\vec{p} - \vec{p'}) \qquad \left[\hat{c}_l(\vec{p}), \hat{c}^\dagger_{l'}(\vec{p'})\right]_- = p^0\delta_{ll'}\delta_3(\vec{p} - \vec{p'}) \qquad \text{for l=1,2,3}$$

with $\hat{P}_{e,\gamma}$ projector on the Fock space of one electron and one photon.
In order to calculate the probability $||\hat{E}^{r\lambda}(M)\hat{U}^{inter}(t_2,t_1)\Psi_{t_1}||^2$ we consider

$$\Pi^{r\lambda}(\vec{q},\vec{k};t_2,t_1) = |\langle\Phi_{t_2}|T\Big(e^{-\frac{ie}{\hbar c}\int_{ct_1}^{ct_2} dx^0 \int_{\mathbb{R}^3} d^3x\, :\hat{\bar{\Psi}}(x)\gamma^\mu\hat{\Psi}(x)\hat{A}_\mu(x):}\Big)|\Psi_{t_1}\rangle|^2 \frac{1}{k^0q^0} \tag{A.2.4}$$

choosing

$$|\Phi_{t_2}\rangle = \hat{b}^{r_f\dagger}(\vec{q_f})\hat{c}^\dagger_{\lambda_f}(\vec{k_f})|0\rangle.$$

From a second order perturbative approach expansion of the time evolution operator we obtain

$$\begin{aligned}\langle\Phi_{t_2}| -i\left(\frac{e}{\hbar c}\right)^2 \iint_{ct_1}^{ct_2} dx_1^0 dx_2^0 \iint_{\mathbb{R}^3} d^3x_1 d^3x_2 \hat{\bar{\Psi}}^{(-)}(x_2)\gamma^{\mu_2}\Big(\hat{A}^{(-)}_{\mu_2}(x_2)S_F(x_2-x_1)\hat{A}^{(+)}_{\mu_1}(x_1)\\ +\hat{A}^{(-)}_{\mu_1}(x_1)S_F(x_2-x_1)\hat{A}^{(+)}_{\mu_2}(x_2)\Big)\gamma^{\mu_1}\hat{\Psi}^{(+)}(x_1)|\Psi_{t_1}\rangle\end{aligned} \tag{A.2.5}$$

where $(+)$ e $(-)$ are respectively the annihilation and creation part of the operators and S_F describes the normal order.
To proceed with the calculation of this expression, the most important steps are the following:

- To put in evidence the energy conservation we consider the long time behavior of the system evolution.

- Since
$$S_F(x) = \lim_{\epsilon\to 0^+}\int dk^0 d^3k \frac{e^{-ikx}}{(2\pi)^4}\frac{k\gamma + \frac{m_e c}{\hbar}I}{k^2 - \frac{m_e^2c^2}{\hbar^2} + i\epsilon} \tag{A.2.6}$$
we integrate on k and develop the calculation of the integral on k^0 by using the complex analysis methods.

- We take into account that the initial wave function are peaked around initial momentum $\vec{q_i}$ for the electron and $\vec{k_i}$ for the photon, so that the initial momentum of the particles is in good approximation $\vec{q_i}$ and $\vec{k_i}$.

- The wave function of a single particle describes the momentum of the particle through its modulus and is related to the position through the phase. The position of the photon is hardly determined, so it is necessary to take an average over the infinite possible choices of $\vec{x}_0$ in a macroscopic space region ω with volume V, inside the bunch, symmetric around the origin, where the density of the photons is constant.

A.3 Differential cross section

The calculation provides the transition probability, defined as the probability that a photon characterized by initial polarization and momentum $\lambda_i, \vec{k}_i$, after the scattering has polarization and momentum $\lambda_f, \vec{k_f}$:

$$
\begin{aligned}
P(\lambda_i, \lambda_f, \vec{k_f} \in d\Omega) = {} & \frac{d\Omega(t_2 - t_1)e^4 m_e^2 c}{V(4\pi\hbar)^2} \frac{1}{|\vec{k}_i|} \frac{1}{\sqrt{m_e^2 c^2 + |\vec{q}_i|^2}} \\
& \frac{1}{\sqrt{m_e^2 c^2 + |\vec{q}_i + \vec{k}_i - \vec{k_f}|^2}} \frac{|\vec{k}_f| \left(\sqrt{m_e^2 c^2 + |\vec{q}_i|^2} + |\vec{k}_i| - |\vec{k}_f| \right)}{\sqrt{m_e^2 c^2 + |\vec{q}_i|^2} + k_i - |\vec{q}_i + \vec{k}_i| \cos\theta} \\
& \cdot Tr_{\mathbb{C}^4} \left\{ \left[\left(\not{e}_{\lambda_f}(\vec{k_f}) \not{k}_i \not{e}_{\lambda_i}(\vec{k}_i) + \not{e}_{\lambda_f}(\vec{k_f}) q_i \cdot e_{\lambda_i}(\vec{k}_i) \right) \frac{\hbar}{2 q_i \cdot k_i} \right. \right. \\
& + \left. \left(\not{e}_{\lambda_i}(\vec{k}_i)(-\not{k}_f) \not{e}_{\lambda_f}(\vec{k_f}) + \not{e}_{\lambda_i}(\vec{k}_i) q_i \cdot e_{\lambda_f}(\vec{k_f}) \right) \frac{\hbar}{-2 q_i \cdot k_f} \right] \left(\frac{m_e c I + \not{q}_i}{4 m_e c} \right) \\
& \cdot \left[\left(\not{e}_{\lambda_i}(\vec{k}_i) \not{k}_i \not{e}_{\lambda_f}(\vec{k}_f) + \not{e}_{\lambda_f}(\vec{k_f}) q_i \cdot e_{\lambda_i}(\vec{k}_i) \right) \frac{\hbar}{q_i \cdot k_i} \right. \\
& \left. \left. - \left(\not{e}_{\lambda_f}(\vec{k_f})(-\not{k}_f) \not{e}_{\lambda_i}(\vec{k}_i) + \not{e}_{\lambda_i}(\vec{k}_i) q_i \cdot e_{\lambda_f}(\vec{k_f}) \right) \frac{\hbar}{q_i \cdot k_f} \right] \frac{m_e c I + \not{q}_i + \not{k}_i - \not{k}_f}{4 m_e c} \right\}
\end{aligned}
\tag{A.3.1}
$$

where $\not{a} = a \cdot \gamma$, $d\Omega = d\Omega(\theta, \phi)$ is the solid angle and θ is the angle between the directions of the incoming electron and the emitted photon.
From the transition probability we can extract the geometrical quantity called differential cross section:

$$
\sigma_{\lambda_i, \lambda_f}(\theta, \phi) = \frac{P(\lambda_f, \lambda_i, \vec{k_f} \in d\Omega(\theta, \phi))V}{d\Omega(t_2 - t_1)}
\tag{A.3.2}
$$

In the usual Compton scattering the electron at the initial state is considered at rest, $\vec{q}_i = 0$. In this case, we get the Klein and Nishina formula:

$$
\begin{aligned}
(\sigma_{\lambda_i, \lambda_f}(\theta, \phi))_{\vec{q}_i = 0} = {} & \frac{1}{4} \left(\frac{e^2}{4\pi m_e c^2} \right)^2 \left(\frac{m_e c}{m_e c + |\vec{k}_i|(1 - \cos\theta)} \right)^2 \\
& \cdot \left[4(\vec{e}_{\lambda_f} \cdot \vec{e}_{\lambda_i})^2 + \frac{|\vec{k}_i|^2 (1 - \cos\theta)^2}{m_e c(m_e c + |\vec{k}_i|(1 - \cos\theta))} \right]
\end{aligned}
\tag{A.3.3}
$$

Since $|\vec{k}_i| \ll m_e c$, for not polarized photon beam and not observed polarization of the scattered photons

$$
(\sigma_{\lambda_i, \lambda_f}(\theta, \phi))_{\vec{q}_i = 0} = \left(\frac{e^2}{4\pi m_e c^2} \right)^2 \frac{1}{2}(1 + \cos^2\theta) = r_0^2 \frac{(1 + \cos^2\theta)}{2}
\tag{A.3.4}
$$

which is the classical Thomson cross section.
Considering the inverse Compton scattering we have to analyze the general case of $\vec{q}_i \neq$

0 and the result is:

$$\sigma_{\lambda_i,\lambda_f}(\theta,\phi) = A \cdot B \tag{A.3.5}$$

where

$$\begin{aligned}A = \left(\frac{e^2}{4\pi m_e c^2}\right)^2 & \frac{m_e c}{\sqrt{m_e^2 c^2 + |\vec{q}_i|^2}} \frac{m_e c}{\sqrt{m_e^2 c^2 + |\vec{q}_i + \vec{k}_i - \vec{k}_f(\theta,\phi)|^2}} \\ & \cdot \frac{|\vec{k}_f(\theta)| \left(\sqrt{m_e^2 c^2 + |\vec{q}_i|^2} + |\vec{k}_i| - |\vec{k}_f(\theta)|\right)}{\sqrt{m_e^2 c^2 + |\vec{q}_i|^2} + |\vec{k}_i| - |\vec{q}_i + \vec{k}_i| \cos\theta}\end{aligned} \tag{A.3.6}$$

and

$$\begin{aligned}B = \frac{1}{2}\Bigg\{ & k_i \cdot k_f \left[\frac{\vec{q}_i \cdot \vec{e}_{\lambda_f} \vec{e}_{\lambda_f} \cdot \vec{k}_i - \vec{q}_i \cdot \vec{e}_{\lambda_i} \vec{e}_{\lambda_i} \cdot \vec{k}_f}{q_i \cdot k_i q_i \cdot k_f} + \frac{1}{2}\left(\frac{1}{q_i \cdot k_f} - \frac{1}{q_i \cdot k_i}\right)\right. \\ & \left. \cdot \left(1 + \frac{(\vec{q}_i \cdot \vec{e}_{\lambda_i})^2}{q_i \cdot k_i} - \frac{(\vec{q}_i \cdot \vec{e}_{\lambda_f})^2}{q_i \cdot k_f}\right)\right] + \frac{1}{2} \frac{(\vec{q}_i \cdot \vec{e}_{\lambda_i})^2 (\vec{q}_i \cdot \vec{e}_{\lambda_f})^2 (q_i \cdot k_i - q_i \cdot k_f)^2}{(q_i \cdot k_i)^2 (q_i \cdot k_f)^2} \\ & + 2(\vec{e}_{\lambda_i} \cdot \vec{e}_{\lambda_f})^2 + \frac{(\vec{q}_i \cdot \vec{k}_f \vec{q}_i \cdot \vec{e}_{\lambda_i} \vec{e}_{\lambda_f} \cdot \vec{k}_i + \vec{q}_i \cdot \vec{k}_i \vec{q}_i \cdot \vec{e}_{\lambda_f} \vec{e}_{\lambda_i} \cdot \vec{k}_f)^2}{(q_i \cdot k_i)^2 (q_i \cdot k_f)^2} \\ & + \frac{1}{2}\left(\vec{q}_i \cdot \vec{e}_{\lambda_f} \vec{e}_{\lambda_f} \cdot \vec{k}_i - \vec{q}_i \cdot \vec{e}_{\lambda_i} \vec{e}_{\lambda_i} \cdot \vec{k}_f + 5\vec{q}_i \cdot \vec{e}_{\lambda_i} \vec{q}_i \cdot \vec{e}_{\lambda_f} \vec{e}_{\lambda_i} \cdot \vec{e}_{\lambda_f}\right)\left(\frac{1}{q_i \cdot k_i} - \frac{1}{q_i \cdot k_f}\right) \\ & + \frac{3}{2}\left[(\vec{q}_i \cdot \vec{e}_{\lambda_i})^2 \vec{q}_i \cdot \vec{e}_{\lambda_f} \vec{e}_{\lambda_f} \cdot \vec{k}_i \left(\frac{1}{(q_i \cdot k_i)^2} - \frac{1}{q_i \cdot k_i q_i \cdot k_f}\right)\right. \\ & \left. + \vec{q}_i \cdot \vec{e}_{\lambda_i} (\vec{q}_i \cdot \vec{e}_{\lambda_f})^2 \vec{e}_{\lambda_i} \cdot \vec{k}_f \left(\frac{1}{q_i \cdot k_i q_i \cdot k_f} - \frac{1}{(q_i \cdot k_f)^2}\right)\right] \\ & + 3\vec{e}_{\lambda_i} \cdot \vec{e}_{\lambda_f} \left(\frac{\vec{q}_i \cdot \vec{e}_{\lambda_i} \vec{e}_{\lambda_f} \cdot \vec{k}_i}{q_i \cdot k_i} + \frac{\vec{q}_i \cdot \vec{e}_{\lambda_f} \vec{e}_{\lambda_i} \cdot \vec{k}_f}{q_i \cdot k_f}\right) \\ & + \frac{1}{4}\left(\frac{(\vec{q}_i \cdot \vec{e}_{\lambda_i})^2}{(q_i \cdot k_i)^2} + \frac{(\vec{q}_i \cdot \vec{e}_{\lambda_f})^2}{(q_i \cdot k_f)^2}\right)(q_i \cdot k_i - q_i \cdot k_f) \Bigg\}\end{aligned} \tag{A.3.7}$$

This formula keeps into account all the possible polarization of the emitted photons and it could be useful for the implementation of an ICS simulation code working in the laboratory frame.

APPENDIX B

Quantum model for ICS and polarization: alternative calculation

The differential cross section (2.17) can be obtained by applying the Lorentz transformations to the electric field instead that to the vector potential, avoiding the necessity of a gauge transformation as in [59].

The cross section in the electron rest frame can be written as

$$\left[\frac{d\sigma}{d\Omega}\right]' = \frac{r_e^2}{4}\left(\frac{\nu'_p}{\nu'_0}\right)^2\left[\frac{\nu'_p}{\nu'_0}+\frac{\nu'_0}{\nu'_p}-2+4(\underline{\epsilon}'_0\cdot\underline{\epsilon}'_p)^2\right]$$

where

$$\underline{\epsilon}'_0 = \frac{\underline{E}'_{x_0}}{|\underline{E}'_{x_0}|}\underline{e}_x+\frac{\underline{E}'_{y_0}}{|\underline{E}'_{y_0}|}\underline{e}_y+\frac{\underline{E}'_{z_0}}{|\underline{E}'_{z_0}|}\underline{e}_z$$

is polarization vector of the electric field.
In the laboratory frame, instead, we have:

$$\frac{d\sigma}{d\Omega} = \frac{r_0^2}{4\gamma_i^2(1-\underline{\beta}_i\cdot\underline{e}_k)^2}\left(\frac{\nu'_p}{\nu'_0}\right)^2 X$$

where the function X is

$$X = \frac{\nu'_0}{\nu'_p}\frac{1-\underline{\beta}_i\cdot\underline{e}_k}{1-\underline{\beta}_i\cdot\underline{n}}+\frac{\nu'_p}{\nu'_0}\frac{1-\underline{\beta}_i\cdot\underline{n}}{1-\underline{\beta}_i\cdot\underline{e}_k}-2+4(\underline{\epsilon}_0\cdot\underline{\epsilon}_p)^2. \tag{B.0.1}$$

In general we have

$$\underline{E}_0 = \gamma_i(\underline{E}'_0+\underline{\beta}_i\times\underline{B}'_0)-\frac{\gamma_i}{\gamma_i+1}\underline{\beta}_i(\underline{\beta}_i\cdot\underline{E}'_0)$$

Under the hypothesis that the electromagnetic radiation can be model by transverse plane waves, $\underline{k}_i \cdot \underline{E}'_0 = 0$. Then $\underline{B}'_0 = \underline{e}_k \times \underline{E}'_0$ and therefore

$$\begin{aligned}\underline{E}_0 =&\gamma_i(\underline{E}'_0 + \underline{\beta}_i \times (\underline{e}_k \times \underline{E}'_0)) - \frac{\gamma_i}{\gamma_i + 1}\underline{\beta}_i(\underline{\beta}_i \cdot \underline{E}'_0)\\ =&\gamma_i(\underline{E}'_0 + (\underline{\beta}_i \cdot \underline{E}'_0)\underline{e}_k - (\underline{\beta}_i \cdot \underline{e}_k)\underline{E}'_0 - \frac{\gamma_i}{\gamma_i + 1}\underline{\beta}_i(\underline{\beta}_i \cdot \underline{E}'_0))\\ =&\gamma_i(\underline{E}'_0(1 - \underline{\beta}_i \cdot \underline{e}_k) + (\underline{\beta}_i \cdot \underline{E}'_0)(\underline{e}_k - \frac{\gamma_i}{\gamma_i + 1}\underline{\beta}_i)).\end{aligned} \tag{B.0.2}$$

$$\begin{aligned}\frac{|\underline{E}_0|^2}{\gamma_i^2} =&|\underline{E}'_0|^2(1 - \underline{\beta}_i \cdot \underline{e}_k)^2 + (\underline{\beta}_i \cdot \underline{E}'_0)^2(1 + \frac{\gamma_i^2}{(\gamma_i + 1)^2}\beta_i^2 - 2\frac{\gamma_i}{\gamma_i + 1}\underline{\beta}_i \cdot \underline{e}_k)\\ &+ 2(1 - \underline{\beta}_i \cdot \underline{e}_k)\underline{\beta}_i \cdot \underline{E}'_0(\underline{E}'_0 \cdot \underline{e}_k - \frac{\gamma_i}{\gamma_i + 1}\underline{E}'_0 \cdot \underline{\beta}_i) = |\underline{E}'_0|^2(1 - \underline{\beta}_i \cdot \underline{e}_k)^2\end{aligned}$$

where in the last equality we used $\underline{E}'_0 \cdot \underline{e}_k = 0$. Then

$$\underline{\epsilon}_0 = \frac{\underline{E}'_0(1 - \underline{\beta}_i \cdot \underline{e}_k) + (\underline{\beta}_i \cdot \underline{E}'_0)(\underline{e}_k - \frac{\gamma_i}{\gamma_i+1}\underline{\beta}_i)}{|\underline{E}'_0|(1 - \underline{\beta}_i \cdot \underline{e}_k)} = \underline{\epsilon}'_0 + \frac{\underline{\beta}_i \cdot \underline{\epsilon}'_0(\underline{e}_k - \frac{\gamma_i}{\gamma_i+1}\underline{\beta}_i)}{1 - \underline{\beta}_i \cdot \underline{e}_k} \tag{B.0.3}$$

and similarly

$$\underline{\epsilon}_p = \underline{\epsilon}'_p + \frac{\underline{\beta}_i \cdot \underline{\epsilon}'_p}{1 - \underline{\beta}_i \cdot \underline{n}}(\underline{n} - \frac{\gamma_i}{\gamma_i + 1}\underline{\beta}_i) \tag{B.0.4}$$

If we set

$$d_1 = 1 - \underline{\beta}_i \cdot \underline{e}_k \qquad d_2 = 1 - \underline{\beta}_i \cdot \underline{n} \qquad d_3 = \underline{e}_k \cdot \underline{n} - 1,$$

by using the Compton relation

$$\nu_p = \nu_0 \frac{d_1}{d_2 - \frac{h\nu_0}{\gamma_i m_e c^2} d_3} \tag{B.0.5}$$

we finally obtain

$$\begin{aligned}\underline{\epsilon}_0 \cdot \underline{\epsilon}_p =&\underline{\epsilon}'_0 \cdot \underline{\epsilon}'_p + \frac{\underline{\beta}_i \cdot \underline{\epsilon}'_0}{1 - \underline{\beta}_i \cdot \underline{e}_k}\Big(\underline{\epsilon}'_p \cdot \underline{e}_k - \frac{\gamma_i}{\gamma_i + 1}\underline{\epsilon}'_p \cdot \underline{\beta}_i\Big)\\ &+ \frac{\underline{\beta}_i \cdot \underline{\epsilon}'_p}{1 - \underline{\beta}_i \cdot \underline{n}}\Big(\underline{\epsilon}'_0 \cdot \underline{n} - \frac{\gamma_i}{\gamma_i + 1}\underline{\epsilon}'_0 \cdot \underline{\beta}_i\Big) + \frac{\underline{\beta}_i \cdot \underline{\epsilon}'_0}{1 - \underline{\beta}_i \cdot \underline{e}_k}\frac{\underline{\beta}_i \cdot \underline{\epsilon}'_p}{1 - \underline{\beta}_i \cdot \underline{n}}\\ &\cdot \Big[\underline{e}_k \cdot \underline{n} - \frac{\gamma_i}{\gamma_i + 1}\underline{\beta}_i(\underline{e}_k + \underline{n}) + \frac{\beta_0^2\gamma_i^2}{(\gamma_i + 1)^2}\Big]\\ =&\underline{\epsilon}'_0 \cdot \underline{\epsilon}'_p + \frac{\underline{\beta}_i \cdot \underline{\epsilon}'_0}{d_1}\Big[\underline{\epsilon}'_p \cdot (\underline{e}_k + \frac{m_e c^2 \gamma_i}{h\nu_i})\Big] + \frac{\underline{\beta}_i \cdot \underline{\epsilon}'_p}{d_2}\Big[\underline{\epsilon}'_0 \cdot (\underline{n} - \frac{m_e c^2 \gamma_i}{h\nu_f})\Big].\end{aligned} \tag{B.0.6}$$

The first three terms of Eq. B.0.1 are not depending on polarization, while the last one depends on both laser and radiation polarization.

By expressing the radiation polarization versor $\underline{\epsilon'}_p$ through two versors perpendicular to $\underline{n}$, $\underline{\epsilon'}_{p1} = -sin\phi\underline{e}_x + cos\phi\underline{e}_y$, and $\underline{\epsilon'}_{p2} = cos\phi cos\theta\underline{e}_x + sin\phi cos\theta\underline{e}_y - sin\theta\underline{e}_z$, the Stokes parameter S_3 is defined as:

$$S_3 = \frac{(\underline{\epsilon}_0 \cdot \underline{\epsilon}_p)^2_{\underline{\epsilon'}_p = \underline{\epsilon'}_{p1}} - (\underline{\epsilon}_0 \cdot \underline{\epsilon}_p)^2_{\underline{\epsilon'}_p = \underline{\epsilon'}_{p2}}}{(\underline{\epsilon}_0 \cdot \underline{\epsilon}_p)^2_{\underline{\epsilon'}_p = \underline{\epsilon'}_{p1}} + (\underline{\epsilon}_0 \cdot \underline{\epsilon}_p)^2_{\underline{\epsilon'}_p = \underline{\epsilon'}_{p2}} + \frac{\nu_0}{2\nu_p}\frac{1-\underline{\beta}_i \cdot \underline{e}_k}{1-\underline{\beta}_i \cdot \underline{n}} + \frac{\nu_p}{2\nu_0}\frac{1-\underline{\beta}_i \cdot \underline{n}}{1-\underline{\beta}_i \cdot \underline{e}_k} - 1}. \tag{B.0.7}$$

Supposing that, as before, $\underline{\beta}_i = \beta_z\underline{e}_z$, $\underline{\epsilon'}_0 = \underline{e}_y$, $\underline{e}_k = -\underline{e}_z$, and that the last three terms in the denominator are negligible, the direct calculation of the Stokes parameter lead to :

$$S_3 = \frac{-\frac{1}{\gamma_i^4} - \frac{2}{\gamma_i^2}sin^2\theta cos2\phi - sin^4\theta cos4\phi}{\frac{1}{\gamma_i^4} + \frac{2}{\gamma_i^2}sin^2\theta cos2\phi + sin^4\theta} \tag{B.0.8}$$

expression that is analogous to Eq. 2.38.

APPENDIX C

Compton Monte Carlo Code (CMCC)

In this code the particle-particle interaction is performed in center of mass (CM) reference frame of the electron-photon system.
To symplify the notations we set in this section $\hbar = c = 1$ and we denote with $*$ the particles' momenta and energies in CM.

If the electron and laser photon energies in LAB are respectively E_i and ν_0, the CM of the electron-photon system is characterized by

$$\gamma_{CM} = \frac{E_{TOT}}{E_{CM}} = \frac{E_i + \nu_0}{\sqrt{2E_i\nu_0 - 2\underline{p}_i \cdot \underline{k}_0 + M_e^2}} \tag{C.0.1}$$

where $M_e = 0.511$ MeV/c^2 and E_{CM} (or $\sqrt{s}$ using the Mandelstam notation) is the invariant mass of the electron-photon system. In case of a relativistic electron colliding nearly head on with the photon, $E_{CM} \simeq \sqrt{4E_i\nu_0 + M_e^2}$. The velocity of the CM is given by

$$\underline{\beta}_{CM} = \frac{\underline{p}_i + \underline{k}_0}{p_i + k_0}. \tag{C.0.2}$$

The momentum modulus of the scattered electron and photon in CM is

$$p^* = k^* = \frac{E_{CM}^2 - M_e^2}{2E_{CM}}. \tag{C.0.3}$$

This equation shows that there is no threshold for this reaction (as expected, it is a scattering) so that the electron recoil can be arbitrarily small.

$$\underline{k}^* = (k_x^*,\ k_y^*,\ k_z^*) = (k^* \sin\theta^* \cos\phi^*,\ k^* \sin\theta^* \sin\phi^*,\ k^* \cos\theta^*) \tag{C.0.4}$$

with θ^* and ϕ^* angles in CM with respect to $\underline{\beta}_{CM}$ direction. The scattered electron and the emitted photon in CM have opposite directions and they are distributed on a sphere of radius $p^* = k^*$. The energy of the electron the photon in CM are $E^* = \sqrt{{p^*}^2 + M_e^2}$ and $\nu^* = k^*$ respectively.

The differential cross section (2.27) for the scattering process is a function of the invariant quantities X and Y, therefore is valid also in the CM frame. In this frame

$$X = \frac{2\nu^*(E^* + \nu^*)}{M_e^2} \qquad \text{and} \qquad Y = \frac{2\nu^*(E^* + \nu^* \cos\theta^*)}{M_e^2}. \tag{C.0.5}$$

To obtain the momentum components of the emitted particles in the laboratory frame we have to apply the Lorentz transformations to the momenta values in CM:

$$\begin{cases} \nu = \gamma_{CM}(k^* + k_x^*\beta_x + k_y^*\beta_y + k_z^*\beta_z) \\ k_x = k^*\beta_x\gamma_{CM} + k_x^*\dfrac{1+\gamma_{CM}^2\beta_x^2}{1+\gamma_{CM}} + k_y^*\dfrac{\gamma_{CM}^2\beta_x\beta_y}{1+\gamma_{CM}} + k_z^*\dfrac{\gamma_{CM}^2\beta_x\beta_z}{1+\gamma_{CM}} \\ k_y = k^*\beta_y\gamma_{CM} + k_x^*\dfrac{\gamma_{CM}^2\beta_x\beta_y}{1+\gamma_{CM}} + k_y^*\dfrac{1+\gamma_{CM}^2\beta_y^2}{1+\gamma_{CM}} + k_z^*\dfrac{\gamma_{CM}^2\beta_y\beta_z}{1+\gamma_{CM}} \\ k_z = k^*\beta_z\gamma_{CM} + k_x^*\dfrac{\gamma_{CM}^2\beta_x\beta_z}{1+\gamma_{CM}} + k_y^*\dfrac{\gamma_{CM}^2\beta_y\beta_z}{1+\gamma_{CM}} + k_z^*\dfrac{1+\gamma_{CM}^2\beta_z^2}{1+\gamma_{CM}} \end{cases} \tag{C.0.6}$$

where $\underline{\beta}_{CM} = (\beta_x,\ \beta_y,\ \beta_z)$. If the scattering is head-on along the z axis, the above transformations simplify in

$$\begin{cases} \nu = k^*\gamma_{CM}\left(1 + \beta_{CM}\cos\theta^*\right) \\ k_x = k^*\sin\theta^*\cos\phi^* \\ k_y = k^*\sin\theta^*\sin\phi^* \\ k_z = k^*\gamma_{CM}\left(\beta_{CM} + \cos\theta^*\right). \end{cases} \tag{C.0.7}$$

Event generator algorithm:

- The electron beam is red from an external file. Each electron collides with a photon with a fixed energy given in input which propagates along the negative z direction.
- The code computes γ_{CM}, β_{CM} and $p^* = k^*$ using eqs. (C.0.1), (C.0.2) and (C.0.3).
- $\overline{\theta^*}$ is chosen randomly in $[0, \pi)$ and plugged in eq. (2.27) integrated over ϕ and normalized:

  $$f(\theta^*) = \frac{8\sin\theta^*}{X^2}\left(\frac{\nu^*}{M_e}\right)^2 \left\{\left[\left(\frac{1}{X} - \frac{1}{Y}\right)^2 + \frac{1}{X} - \frac{1}{Y}\right] + \frac{1}{4}\left(\frac{X}{Y} + \frac{Y}{X}\right)\right\}. \tag{C.0.8}$$

  A random number $r_1 \in [0, 1)$ is compared with $f(\overline{\theta^*})$: if $r_1 \geq f(\overline{\theta^*})$ the photon is not generated and the code moves to the next electron. Otherwise $\overline{\theta^*}$ is set.
- $\overline{\phi^*}$ is selected in $[0, 2\pi)$ and eq. (2.27) is evaluated in $(\overline{\theta^*}, \overline{\phi^*})$. This value $g(\overline{\theta^*}, \overline{\phi^*})$ is compared to another random number $r_2 \in [0, 1)$. If $r_2 \geq g(\overline{\theta^*}, \overline{\phi^*})$ the azimuthal angle is selected again, otherwise both angles are set.
- The momentum components of the emitted photon (and electron) are calculated as in (C.0.4) and transformed to the LAB using eq. (C.0.6).

- Once the θ_{max} corresponding to a certain bandwidth $\Delta\nu_p/\nu_p$ is defined, the number of photons in that bandwidth can be deduced by

$$N^{bw} = N \frac{\text{photons generated in } \theta_{max}}{\text{total generated photons}} \tag{C.0.9}$$

  where N is defined in eq. (3.2).

- The polarization of the emitted photon is calculated as described in (Approach 1).

Remark. *This code is not tracking the particles, it is not considering the laser intensity variations and it does not take into account the multiple scattering.*

Remark. *In Fig. C.1 the differential cross section (2.27) for unpolarized beams in CM is shown for different values of the recoil parameter Δ. By comparing this graph with the one in Fig. 2.8, we notice that the shape of the differential cross section in ERF and CM are very similar at low Δ values, while they strongly differ in the ultrarelativistic regime.*

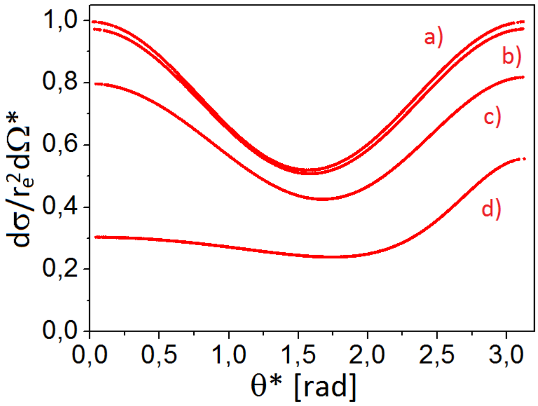

Figure C.1: Differential Compton cross section $d\sigma/d\Omega^*$ for unpolarized beams in CM normalized by r_e^2 as a function of θ^* [rad] for different values of Δ: $7.37 \cdot 10^{-4}$ a), $7.37 \cdot 10^{-3}$ b), $7.37 \cdot 10^{-2}$ c), 0.737 d).

We repeat with CMCC the same simulations performed by means of CAIN in Chapter 3: the electron beams features are reported in Table 3.1. The values of the relative bandwidth value and the number of photons in the collimation angle $\theta_{max} = 160\ \mu$rad are reported in Table C.1.

Fig. C.2 shows the collimated spectra: the spectra obtained by beams A and B are perfectly superimposed and the same happens for beams D and E. In those two cases the difference between the emitted beams is given by the number of photons, which is calculated through the formula (C.0.9).

Table C.1: Results of the simulations: relative bandwidth value [‰] and number of photons in the collimation angle.

Beam	$\Delta\nu_p/\nu_p$ [‰]	N^{bw}
A	4.42	$1.93 \cdot 10^6$
B	4.42	$7.27 \cdot 10^5$
C	4.70	$7.28 \cdot 10^5$
D	6.99	$1.91 \cdot 10^6$
E	6.99	$7.19 \cdot 10^5$

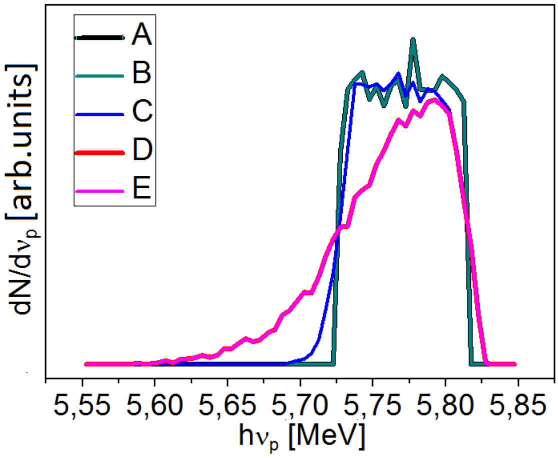

Figure C.2: Spectrum of the emitted photons dN/dhν_p [arb. units] in the collimation angle as a function of energy hν_p [MeV] obtained by the interaction of the electron beams reported in Table 3.1. The spectra colors are related to the electron beam as follows: A black, B dark cyan, C blue, D red, E magenta.

In Fig. C.3 the resulting photons of bema E collision are presented: the spectrum and the transverse distribution of the full and collimated beams are shown in black and red respectively. The results obtained with CMCC are in perfect agreement with the ones given by CAIN, especially if only the first generation of photons simulated by CAIN is taken into account.

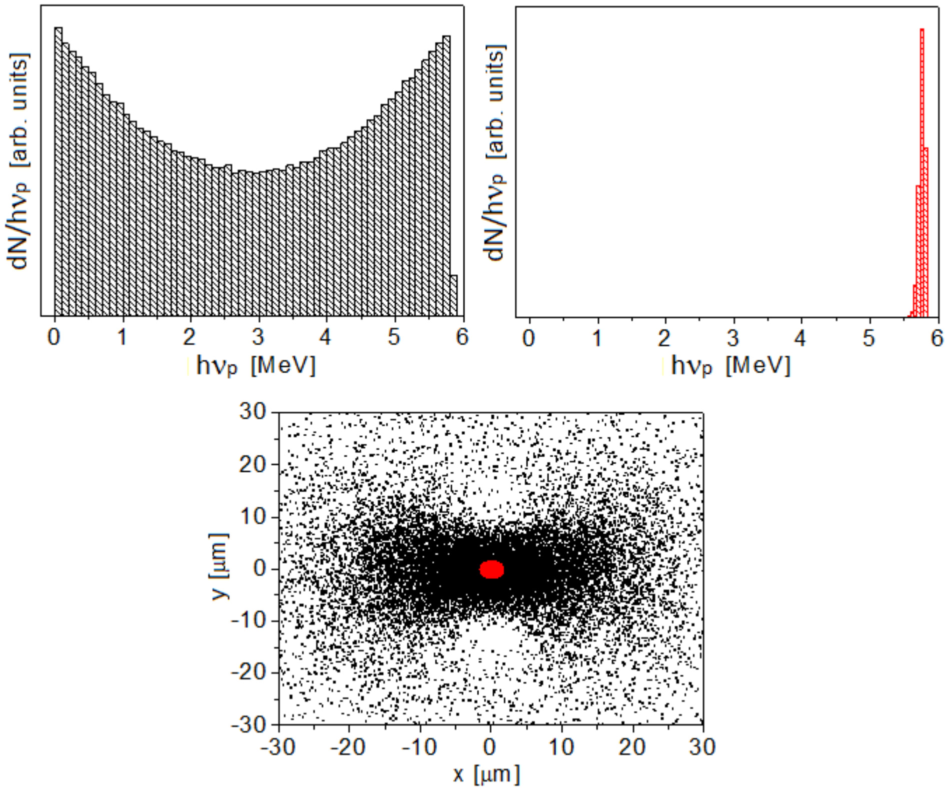

Figure C.3: Result of the beam E simulation: emitted photons spectrum dN/dhν_p [arb. units] as a function of energy hν_p [MeV] and transverse distribution on a screen at 10 m from the IP (x and y coordinates in [μm]). Total beam in black, collimated beam in red.

Pion photo-production differential cross section

The differential cross sections for the pion photo-production we used in our simulations have been found in [106]. The cross sections values reported in this article refer to fixed target experiments and therefore are related to the proton rest frame. We made the assumption that at those incoming particle energies the differential cross sections in the proton rest frame (PRF) and in the CM frame are very similar. To make sure this assumption is valid we compared the spectra obtained by the event generator code we described in Chapter 6 to another home-made code which samples the pion photo-production in PRF. The results obtained by the two codes (we will call them codeCM and codePRF) are, as we expected, in good agreement. For a deeper analysis of the emitted particle beams the codePRF is more appropriate: codeCM is faster but the differential cross section in CM has to be implemented in the code in order to have high precision results.

In the following, an example of comparison is reported: the proton beam energy is $E_p = 50$ TeV and $h\nu = 2.251$ keV. In PRF $h\nu' = 240$ MeV and therefore the differential cross section is the one reported in Fig. D.1 (from [106]).

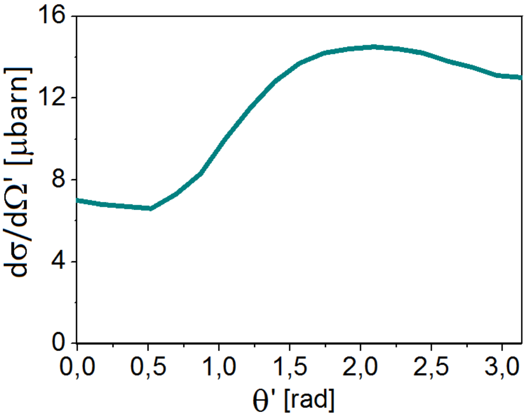

Figure D.1: Differential cross section [μbarn] as a function of θ' in PRF at $h\nu' = 240$ MeV.

The data relative to the muon beam obtained by the pion decay simulated by codeCM and codePRF are reported in Table D.1, while Fig. D.2 shows the spectra of pion and muon beams. Both the data and the spectra are similar for the two simulations.

Table D.1: Muon beam data obtained by the pion beam decay simulated by codeCM and codePRF.

Code	$\Delta p_{\mu_z}/p_{\mu_z}$ [%]	$\langle p_{\mu_z} \rangle$ [TeV/c]	$p_{\mu_z}^{rms}$ [TeV/c]	ϵ_n^{μ} [mm·mrad]
codeCM	41.43	7.43	3.08	1.64
codePRF	44.46	6.57	2.92	1.09

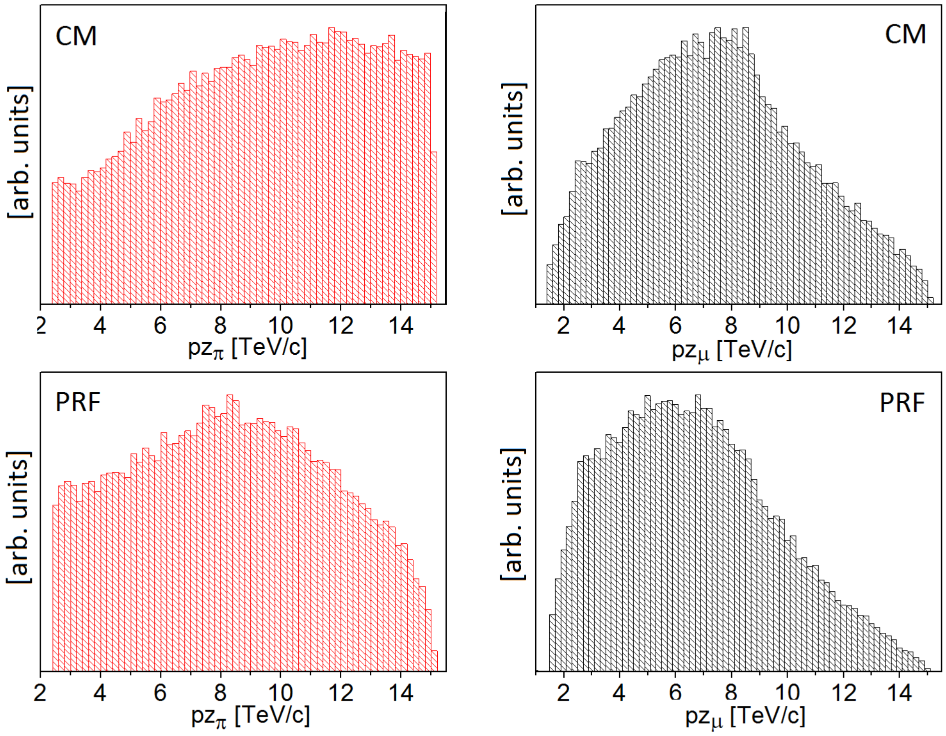

Figure D.2: Comparison of the pion dN/dp_{π_z} and muon dN/dp_{μ_z} beams spectra as a function of p_{π_z} and p_{μ_z} respectively [TeV/c] obtained by using codeCM (top line) and codePRF (bottom line).

Bibliography

[1] H. Motz, *Applications of the radiation from fast electron beams*, J. Appl. Phys. 22 (1951) 527-531

[2] K. Landecker, *Possibility of frequency multiplication and wave amplification by means of some relativistic effects*, Phys. Rev. 86 (1952) 852-855

[3] R. H. Milburn, *Electron scattering by an intense polarized photon field*, Phys. Rev. Lett. 10 (1963) 75-77

[4] F. R. Arutyunian and V. A. Tumanian, *The Compton effect on relativistic electrons and the possibility of obtaining high energy beams*, Phys. Lett. 4 (1963) 176-178

[5] L. Federici *et al.*, *Backward Compton Scattering of Laser Light against High-Energy Electrons: the LADON Photon Beam at Frascati*, Nuovo Cimento B 59 (1980) 247-256

[6] D. Babusci *et al.*, *Polarised and tagged gamma-ray Ladon beams*, `http://www.iaea.org/inis/collection/NCLCollectionStore/_Public/28/042/28042622.pdf` (1995)

[7] C. M. Guenther *et al.*, *Sequential femtosecond X-ray imaging*, Nat. Photonics 5 (2011) 99-102

[8] F. Tavella *et al.*, *Few-femtosecond timing at fourth-generation X-ray light sources*, Nat. Photonics 5 (2011) 162-165

[9] P. G. Thirolf and D. Habs, *Bright perspectives for nuclear photonics*, Eur. Phys. J. Special Topics 223, 1213–1219 (2014)

[10] I. V. Pogorelsky *et al.*, *Demonstration of* 8×10^{18} *photons/second peaked at* 1.8 *Å in a relativistic Thomson scattering experiment*, Phys. Rev. ST Accel. Beams 3, 090702 (2000)

[11] W. Brown *et al.*, *Experimental characterization of an ultrafast Thomson scattering x-ray source with three-dimensional time and frequency-domain analysis*, Phys. Rev. ST Accel. Beams 7, 060702 (2004)

[12] F. V. Hartemann *et al.*, *Characterization of a bright, tunable, ultrafast Compton scattering X-ray source*, Laser Part. Beams 22 (2004) 221-244

[13] M. Babzien *et al.*, *Observation of the Second Harmonic in Thomson Scattering from Relativistic Electrons*, Phys. Rev. Lett. 96, 054802 (2006)

[14] M. Bech *et al.*, *Hard X-ray phase-contrast imaging with the Compact Light Source based on inverse Compton X-rays*, J. Synchrotron Radiat. 16 (2009) 43-47

[15] R. Kuroda *et al.*, *Quasi-monochromatic hard X-ray source via laser Compton scattering and its application*, Nucl. Instr. Meth. Phys. Res. A 637 (2011) S183-S186

[16] Y. Du *et al.*, *Generation of first hard X-ray pulse at Tsinghua Thomson Scattering X-ray Source*, Rev. Sci. Instrum. 84, 053301 (2013)

[17] G. Priebe *et al.*, *Status of the inverse Compton backscattering source at Daresbury Laboratory*, Nucl. Instr. Meth. Phys. Res. A 608 (2009) S109-S112

[18] A. Jochmann *et al.*, *High Resolution Energy-Angle Correlation Measurement of Hard X Rays from Laser-Thomson Backscattering*, Phys. Rev. Lett. 111, 114803 (2013)

[19] H. Ikeura-Sekiguchi *et al.*, *In-line phase-contrast imaging of a biological specimen using a compact laser-Compton scattering-based x-ray source*, Appl. Phys. Lett. 92, 131107 (2008)

[20] Y. Sakai *et al.*, *Observation of redshifting and harmonic radiation in inverse Compton scattering*, Phys. Rev. ST Accel. Beams 18, 060702 (2015)

[21] K. Achterhold *et al.*, *Monochromatic computed tomography with a compact laser-driven X-ray source*, Sci. Rep. 3, 1313 (2013)

[22] B. Golosio *et al.*, *Measurement of an inverse Compton scattering source local spectrum using k-edge filters*, Appl. Phys. Lett. 100, 164104 (2012)

[23] F. G. Meinel *et al.*, *Diagnosing and mapping pulmonary emphysema on X-ray projection images: incremental value of grating-based X-ray dark-field imaging*, PLOS ONE 5, 59526 (2013)

[24] P. G. Thirolf *et al.*, *Perspectives for photofission studies with highly brilliant, monochromatic γ-ray beams*, EPJ Web Conf. 38, 08001 (2012)

[25] A. D'angelo *et al.*, *Generation of Compton backscattering γ-ray beams*, Nucl. Instr. Meth. Phys. Res. A 455 (2000) 1-6

[26] D. J. Gibson *et al.*, *Design and operation of a tunable MeV-level Compton-scattering-based γ-ray source*, Phys. Rev. ST Accel. Beams 13, 070703 (2010)

[27] S. Miyamoto *et al.*, *Laser Compton back-scattering gamma-ray beamline on NewSUBARU*, Rad. Meas. 41 (2007) S179–S185

[28] S. Amano *et al.*, *Several-MeV g-ray generation at NewSUBARU by laser Compton backscattering*, Nucl. Instr. Meth. Phys. Res. A 602 (2009) 337–341

[29] K. Aoki *et al.*, *High-energy photon beam production with laser-Compton backscattering*, Nucl. Instr. Meth. Phys. Res. A 516 (2004) 228–236

[30] *Advanced Light Source*, `http://accelconf.web.cern.ch/AccelConf/IPAC2015/papers/tupma001.pdf`

[31] T. Akagi *et al.*, *Production of gamma rays by pulsed laser beam Compton scattering off GeV-electrons using a non-planar four-mirror optical cavity*,`http://arxiv.org/pdf/1111.5834v2.pdf` (2012)

[32] H. Toyokawa *et al.*, *Recent progress in generation and application of AIST laser-Compton gamma-ray beam*, Nucl. Instr. Meth. Phys. Res. A 608(2009) S41–S43

[33] W. Guo *et al.*, *A high intensity beam line of g-rays up to 22MeV energy based on Compton backscattering*, Nucl. Instr. Meth. Phys. Res. A 578 (2007) 457–462

[34] T. Kaneyasu *et al.*, *Performance of the Laser Compton Scattering Gamma-Ray Source at SAGA-LS*, Journal of Physics: Conference Series 425, 042018 (2013)

[35] N. S. Mirian *et al.*, *Present status of source development station at UVSOR-III* , `http://arxiv.org/ftp/arxiv/papers/1509/1509.00700.pdf` (2015)

[36] S. H. Park, *Spatial distribution and polarization of γ-rays generated via Compton backscattering in the Duke/OK-4 storage ring FEL*, Nucl. Instr. Meth. Phys. Res. A 475 (2001) 425–431

[37] C. Sun, *PhD Thesis: Characterizations and Diagnostics of Compton Light Source*, `http://dukespace.lib.duke.edu/dspace/bitstream/handle/10161/1579/D_Sun_Changchun_a_200912.pdf?sequence=1` (2009)

[38] C. Sun and Y. K. Wu, *Theoretical and simulation studies of characteristics of a Compton light source*, Phys. Rev. ST Accel. Beams 14, 044701 (2011)

[39] Y. K. Wu, *Progress using an FEL oscillator for Compton Scattering*, `http://accelconf.web.cern.ch/AccelConf/FEL2014/talks/wea01_talk.pdf` (2014)

[40] A. P. Tonchev *et al.*, *The high intensity γ-ray source (HIγS) and recent results*, Nucl. Instr. Meth. Phys. Res. B 241 (2005) 170–175

[41] *The White Book of ELI Nuclear Physics*, `http://www.eli-np.ro/documents/ELI-NP-WhiteBook.pdf` (2011)

[42] EuroGammaS, *ELI-NP-GBS Technical Design Report*, `http://arxiv.org/ftp/arxiv/papers/1407/1407.3669.pdf` (2014)

[43] EuroGammas Association, `http://www.e-gammas.com/`

[44] C. Vaccarezza *et al.*, *A European proposal for the Compton gamma-ray source of ELI–NP*, International Particle Accelerator Conference – IPAC12 (2012) 1086–1088

[45] P. Cardarelli *et al.*, *Monte Carlo simulation of a collimation system for low-energy beamline of ELI–NP Gamma Beam System*, Nucl. Instr. Meth. Phys. Res. B, 355 (2015)

[46] K. Dupraz *et al.*, *Design and optimization of a highly efficient optical multipass system for γ-ray beam production from electron laser beam Compton scattering*, Phys. Rev. ST Accel. Beams 17 (2014)

[47] K. Dupraz, *These de Doctorat: Conception et optimisation d'un recirculateur optique pour la source haute brillance de rayons gamma d'ELI-NP* (2015)

[48] A. Bacci *et al.*, *Electron Linac design to drive bright Compton back-scattering gamma-ray sources*, J. Appl. Phys. 113 (2013)

[49] D. Alesini *et al.*, *High Power Test Results of the SPARC C-Band Accelerating Structures*, Proceedings of IPAC2014, MOOCA01 (2014) 39

[50] F. Schwabl, *Advanced Quantum Mechanics*, Springer, New York (2005)

[51] M. Alonso and E. J. Finn, *Quantum and Statistical Physics*, Addison Wesley Publishing Company, Cambridge (1972)

[52] O. Klein and Y. Nishina, *Über die Streuung von Strahlung durch freie Elektronen nach der neuen relativistischen Quantendynamik von Dirac*, Z. Phys. 52 (1929) 11-12

[53] A. Compton, *A quantum theory of the scattering of x-rays by light elements* Phys. Rev. 21 (1923) 483-502

[54] W. Heitler, *The Quantum Theory of Radiation*, The International Series of Monographs in Physics, Oxford at the Clarendon Press (1957)

[55] J. M. Jauch and F. Roerlich, *The theory of photons and electrons*, Addison Wesley Publishing Company, Cambridge (1955)

[56] G. Bhatt *et al.*, *Relativistic Spin-dependent Compton Scattering from Electrons*, Phys. Rev. A 28, 4 (1983) 2195-2200

[57] A. O. G. Källen, *Prinzipien der Quantentheorie I, Quantenelektrodynamik*, Springer-Verlag (1958)

[58] C. Curatolo, L. Lanz and V. Petrillo, *Inverse Compton cross section revisited*, Phys. Procedia 52 (2014) 46-51

[59] V. Petrillo *et al.*, *Photon flux and spectrum of γ-rays Compton sources*, Nucl. Instr. Meth. Phys. Res. A 693 (2012) 109

[60] V. Berestetskii, E. Lifshitz and L. Pitaevskii, *Quantum Electrodynamics. Landau and Lifshitz, Course of Theoretical Physics, Vol. 4*, Pergamon Press (1982)

[61] K. Yokoya, `http://www-acc-theory.kek.jp/members/cainS` (1985)

[62] K. Yokoya, *User manual of CAIN, version 2.40*, `http://lcdev.kek.jp/yokoya/CAIN/Cain242/CainMan242.pdf` (2009)

[63] J. D. Jackson, *Classical Electrodynamics*, John Wiley & Sons, Inc. (1998)

[64] V. Petrillo *et al.*, *Polarization of x-gamma radiation produced by a Thomson and Compton inverse scattering*, Phys. Rev. ST Accel. Beams 18 (2015)

[65] P. Tomassini *et al.*, *Linear and Nonlinear Thomson Scattering for Advanced X-ray Sources in PLASMONX*, IEEE T. Plasma Sci. 36 (2008)

[66] A. P. Potylitsyn and A. M. Kolchuzhkin, *Spectral characteristics of Compton backscattering sources. Linear and nonlinear modes*, Nucl. Instr. Meth. Phys. Res. B 355 (2015) 246–250

[67] L. D. Landau and E. M. Lifshitz, *The Classical Theory of Fields, Course of Theoretical Physics, Vol. 2*, Pergamon Press (1971)

[68] I. Chaikovska, *These de Doctorat: Polarized positron sources for the future linear colliders* (2012)

[69] L. Lanz, *Appunti del corso di Meccanica Quantistica 2*, Scientifica CUSL, Milano (2008)

[70] D. Babusci, *Photon polarization properties in laser backscattering*, Phys. Lett. B 355 (1995) 1–8

[71] C. Maroli *et al.*, *Nonlinear effects in Thomson backscattering*, Phys. Rev. ST Accel. Beams 16, 030706 (2013)

[72] K. Floettmann, *ASTRA*, `http://www.desy.de/~mpyflo/` (1997)

[73] TStep is an upgraded version of PARMELA, see: L. M. Young, PARMELA, Los Alamos National Laboratory Report LA-UR-96-1835

[74] L. M. Young, *PARMELA*, `http://pbpl.physics.ucla.edu/Literature/Special_Collections/docs/parmela.pdf` (1999)

[75] M. Borland, *elegant: A Flexible SDDS-Compliant Code for Accelerator Simulation*, `http://www.aps.anl.gov/Science/Publications/lsnotes/content/files/aps_1418218.pdf` (2000)

[76] V. Ivashchenko *et al.*, *NESTOR reference orbit correction*, Proceedings EPAC2014 (2014) 1431-1433

[77] A. Bacci, A. Giribono and C. Vaccarezza, EuroGammaS Internal Report (2015)

[78] A. Giribono *et al.*, *6D phase space electron beam analysis and machine sensitivity studies for ELI-NP-GBS*, Proceedings EAAC2015 (submitted to NIM A)

[79] K. Dupraz and F. Zomer, EuroGammaS Internal Report (2014)

[80] L. Serafini, C. Curatolo and V. Petrillo, *Low emittance pion beams generation from bright photons and relativistic protons*, `http://arxiv.org/pdf/1507.06626.pdf` (2015)

[81] D. Neuffer *et al.*, *A muon collider as a Higgs factory*, `http://arxiv.org/ftp/arxiv/papers/1502/1502.02042.pdf` (2015)

[82] D. M. Kaplan, *Muon Colliders and Neutrino Factories*, `http://arxiv.org/pdf/1412.3487v1.pdf` (2014)

[83] M. M. Alsharo'a *et al.*, *Recent Progress in Neutrino Factory and Muon Collider Research within the Muon Collaboration*, `http://arxiv.org/pdf/hep-ex/0207031v3.pdf` (2003)

[84] C. M. Ankenbrandt *et al.*, *Status of muon collider research and development and future plans*, Phys. Rev. ST Accel. Beams 2 (1999)

[85] K. T. McDonald, *Emittance Growth from Weak Relativistic Effects*, `http://www.physics.princeton.edu/~mcdonald` (2011)

[86] K. T. McDonald, *The Bethe-Heitler Process as a Source of Muons*, `http://www.physics.princeton.edu/~mcdonald` (2015)

[87] *Large Hadron Collider*, `http://lhc.web.cern.ch/lhc`

[88] E. Todesco and F. Zimmermann, *The Higher-Energy Large Hadron Collider*, Proc. EuCARD-AccNet HE-LHC workshop (2010)

[89] *Future Circular Collider*, `https://fcc.web.cern.ch/Pages/default.aspx`

[90] M. Benedikt and F. Zimmermann, *Future Circular Colliders*, `https://cds.cern.ch/record/2110739/files/CERN-ACC-2015-165.pdf`

[91] Ian Hinchliffe *et al.*, *Luminosity goals for a 100-TeV pp collider*, `http://arxiv.org/pdf/1504.06108.pdf`

[92] H. Yumoto *et al.*, *Micro-focusing of hard x-ray free electron laser radiation using Kirkpatrick-Baez mirror system*, Journal of Physics Conference Series 425 (2013)

[93] Y. Jiao *et al.*, *Modeling and multidimensional optimization of a tapered free electron laser*, Phys. Rev. ST Accel. Beams 15 (2012)

[94] C. Emma *et al.*, *Terawatt x-ray free-electron-laser optimization by transverse electron distribution shaping*, Phys. Rev. ST Accel. Beams 17 (2014)

[95] I. Agapov *et al.*, *Sase characteristics from baseline European XFEL undulators in the tapering regime*, Proceedings of FEL2014, Basel, Switzerland MOP056 (2014)

[96] *Super Proton Synchrotron*, `http://home.cern/about/accelerators/super-proton-synchrotron`

[97] A. Bacci *et al.*, *The SPARC-LAB Thomson source commissioning*, Proceedings IPAC2014, MOPRO078 (2014) 267

[98] M. Ferrario *et al.*, *SPARC-LAB present and future*, Nucl. Instr. Meth. Phys. Res. B 309 (2013) 183-188

[99] C. Vaccarezza *et al.*, *The SPARC-LAB Thomson source*, EAAA 2015 Conference (2015)

[100] R. Paramatti, *Cinematica Relativistica*, `http://www.roma1.infn.it/cms/ric/cinematica.pdf` (2013)

[101] S. Petrera, *La Relativitá in Fisica delle Particelle*, `http://www.aquila.infn.it/petrera/WebClasses/lezioni/relativitylectures.pdf` (2015)

[102] *Linac Coherent Light Source*, `http://lcls.slac.stanford.edu`

[103] *Linac Coherent Light Source II*, `https://portal.slac.stanford.edu/sites/lcls_public/lcls_ii/Pages/default.aspx`

[104] *European X-Ray Laser Project*, `http://www.xfel.eu/`

[105] A. Dadi and C. Muller, *Phenomenological model of multiphoto-production of charged pion pairs on the proton*, `http://arxiv.org/abs/1009.0621v1` (2010)

[106] D. Drechsel *et al.*, *A unitary isobar model for pion photo- and electroproduction on the proton up to 1 GeV*, Nucl. Phys. A 645 (1999) 145-174

[107] D. Drechsel and L. Tiator, *Threshold pion photoproduction on nucleons*, Nucl. Part. Phys. 18 (1992) 449-497

[108] Y. Tsai, *Pair production and bremsstrahlung of charged leptons*, Rev. Mod. Phys. 46, 4 (1974)

[109] Aachen-Berlin-Bonn-Hamburg-Heidelberg-München Collaboration, H. G. Hilpert *et al.*, *Photoproduction of negative pions on neutrons at photon energies between* 0.2-*GeV and* 2.0-*GeV*, Nucl. Phys. B 8 (1968) 535-544

[110] K. Kondo *et al.*, *Analysis of pion photoproduction on nucleons below 500 MeV*, J. Phys. Soc. Jpn 29, 1 (1970)

[111] E. M. Darwish and R. S. Alamry, *Quasifree pion photoproduction from the deuteron in the energy region from threshold up to the* $\Delta(1232)$*-resonance including polarization observables*, JTUSCI 4 (2010) 46-55

[112] H. Fujii, *Total pair production cross section of photons for hydrogen in the energy range* 330 *MeV to* 910 *MeV*, Nucl. Phys. B 114 (1976) 477-482

[113] H. Athar, *Muon pair production by electron-photon scatterings*, Phys. Rev. D 64, 071302(R) (2001)

[114] J. W. Motz, *Pair production by photons*, Rev. Mod. Phys. 41 (1969)

Acknowledgments

I wish to thank my supervisor, Vittoria Petrillo, for the constant help she gave me, for her patience, support and professionality, for the time and the energies she dedicated to me. My gratitude goes also to my co-supervisor, Lodovico Lanz, for everything he taught me and for all the advice he gave me. I greatly thank Luca Serafini, who offered me the opportunity to get involved in the study and development of his novel idea of a Hadron-Photon Collider. I thank a lot the whole Milan group: Alberto Bacci for all the help and the explanations he gave me through these years and for providing the electron beams for the interaction simulations; Illya Drebot for the time spent working together to the simulations for the ELI-NP-GBS; Cesare Maroli, Andrea Rossi, Marcello Rossetti Conti and Francesco Broggi for the fruitful and interesting discussions. I thank Calin Ur for the accurate review and correction of this document. I would also like to thank Najmeh Mirian, Anna Giribono, Paolo Cardarelli, Fabian Zomer, Kevin Dupraz, Paolo Tomassini, Cristina Vaccarezza, Massimo Ferrario, Gabriel Suliman, Dennis Palmer, Stefano Lazzari, Bryant Garcia, Alessandro Variola, Danilo Babusci and Frank Zimmermann for their collaboration and/or their advice and suggestions.